Summer 2015

# Improved theoretical prediction of nanoparticle stability and the synthesis, characterization, and application of gold nanoparticles of various morphology in surface-enhanced infrared spectroscopy

A. K. Lahiru Anuradha Wijenayaka
*University of Iowa*

## Recommended Citation

Wijenayaka, A. K. Lahiru Anuradha. "Improved theoretical prediction of nanoparticle stability and the synthesis, characterization, and application of gold nanoparticles of various morphology in surface-enhanced infrared spectroscopy." PhD (Doctor of Philosophy) thesis, University of Iowa, 2015.
http://ir.uiowa.edu/etd/1931.

# IMPROVED THEORETICAL PREDICTION OF NANOPARTICLE STABILITY AND THE SYNTHESIS, CHARACTERIZATION, AND APPLICATION OF GOLD NANOPARTICLES OF VARIOUS MORPHOLOGY IN SURFACE-ENHANCED INFRARED SPECTROSCOPY

by

A. K. Lahiru Anuradha Wijenayaka

A thesis submitted in partial fulfillment
of the requirements for the Doctor of
Philosophy degree in Chemistry
in the Graduate College of
The University of Iowa

August 2015

Thesis Supervisors: Associate Professor Christopher M. Cheatum
Associate Professor Amanda J. Haes

Graduate College
The University of Iowa
Iowa City, Iowa

CERTIFICATE OF APPROVAL

PH.D. THESIS

This is to certify that the Ph.D. thesis of

A. K. Lahiru Anuradha Wijenayaka

has been approved by the Examining Committee for the thesis requirement for the Doctor of Philosophy degree in Chemistry at the August 2015 graduation.

Thesis Committee:

Christopher M. Cheatum, Thesis Supervisor

Amanda J. Haes, Thesis Supervisor

Sarah C. Larsen

Claudio J. Margulis

Markus Wohlgenannt

To my beautiful family, with love…….

“Education is not the learning of facts, but the training of the mind to think”

Albert Einstein

# ACKNOWLEDGMENTS

First and foremost, I wish to thank my research advisors Professor Christopher Cheatum and Professor Amanda Haes for their valuable insights and guidance throughout my time in graduate school. A special thank goes to all Cheatum group members for creating a pleasant working environment and a friendly and supportive atmosphere within the group. I also wish to thank the Haes group members, especially Dr. Michael Ivanov, Binaya Shrestha, and Grace Lu for collaborating with me in numerous ways in the studies discussed herein. I express my sincere thanks to all technical and administrative staff at the Department of Chemistry of the University of Iowa for their very supportive role in this journey. Further, I wish to thank all the teachers from my childhood to date, especially the teachers and faculty at the Royal College, Colombo and the University of Colombo for always believing in me.

A special thank goes to my parents, my brother, and also all my friends who have been a momentous part of this journey. I appreciate all the wonderful things you have done to make this journey memorable. I am greatly thankful to my loving wife Thilini for being by my side throughout this wonderful journey. You have been there for me and given me the courage to strive to do what I believe. Your caring words kept the spirit alive whenever it was needed. So thank you for being a part of my life! Thank you for believing in me and for all the wonderful things that you have done and continue to do for me and our beautiful family. Finally, I would not forget my loving little son Nethuja, without whom writing this dissertation would have been much easier, but certainly less pleasurable. I am indeed thankful for your wonderful presence in our lives.

# ABSTRACT

The overarching objective of the investigations discussed herein is the development of a model experimental system for surface-enhanced infrared absorption (SEIRA) spectroscopy, with potential applicability in higher order infrared spectroscopic techniques, specifically, surface-enhanced two-dimensional infrared (SE-2D IR) spectroscopy.

Theoretical predictions that accurately predict the stability of functionalized nanoparticles enable guided design of their properties but are often limited by the accuracy of the parameters used as model inputs. Hence, first, such parameterization limitations for the extended DLVO (xDLVO) theory are overcome using a size-dependent Hamaker constant for gold, interfacial surface potentials, and tilt angles of self-assembled monolayers (SAMs), which collectively improves the predictive power of xDLVO theory for modeling nanoparticle stability. Measurements of electrical properties of functionalized gold nanoparticles validate the predictions of xDLVO theory using these new parameterizations illustrating the potential for this approach to improve the design and control of the properties of functionalized gold nanoparticles in various applications.

Next, a series of experiments were conducted to elucidate the behavior of various infrared active molecules in the presence of spherical gold nanoparticles of average diameter ~20 nm. Here, the spectroscopic anomalies, specifically the shifted vibrational frequency and the dispersive lineshape observed in the infrared spectra for $SCN^-$ in the presence of gold nanoparticles provide direct evidence of SIERA.

Nevertheless, it was evidenced that nanomaterial with plasmonic properties that extends into the infrared wavelengths and/or substrates that support image charges are imperative in observing efficient infrared enhancements. Hence, nanomaterials indicating

plasmonic properties extending into the infrared wavelengths were synthesized via a straightforward, seedless, one-pot synthesis. The gold nanostars prepared here indicated plasmonic behavior clearly extending into the near infrared, with simple plasmonic tunability via changing the buffer concentration used during synthesis.

The systematic understanding achieved here in terms of theoretical prediction of nanoparticle stability, origin of infrared spectral anomalies in the presence of nanomaterials, and the preparation of infrared plasmonic material, collectively provides a resilient framework for the further investigation of surface-enhanced infrared spectroscopic techniques including SEIRA and SE-2D IR spectroscopies.

# PUBLIC ABSTRACT

Nanoparticles are materials that are on the order of one billionth of a meter in size and particles of such small size behave in very unique ways allowing them to exhibit many properties important to industrial and scientific applications. These properties rely on the fact that the nanoparticles exist as individual structures, not combined with its neighboring particles. Hence, here we conduct modifications on an existing model such that the stability of a specific type of nanoparticle can be theoretically predicted.

Spectroscopy or the study of the interactions between light and matter is important in many chemical analyses. Metal nanoparticles are widely used to increase the efficiency of the above light - matter interactions thereby allowing to efficiently identify chemical species, determine their structure, and understand how they behave under given conditions. Here, we use gold nanoparticles to demonstrate that this interesting characteristic of metal nanoparticles can be extended into novel scientific techniques, allowing increased efficiency in identifying or even understanding chemical substances.

Preparation of competent nanoparticles for such applications is important, but at the same time challenging. Here we demonstrate a new method of preparing gold nanoparticle that are shaped in the form of stars, hence being named ‘nanostars’. The prepared nanostars demonstrate many unique, interesting, and tunable properties, suggesting their efficient applicability in many scientific applications. The overall understanding attained in the series of investigations conducted here, will be imperative in the design, preparation, and application of new and exciting forms of nanoparticles in many novel scientific applications.

# TABLE OF CONTENTS

# LIST OF TABLES

## LIST OF FIGURES

# CHAPTER 1

# INTRODUCTION

## 1.1 Enhancement of Infrared Spectroscopic Signals: Significance and the Ensuing Implications

Two-dimensional Infrared (2D IR) spectroscopy can reveal kinetic as well as dynamic information on various molecular systems.[2] It is a powerful tool for characterizing molecular structure that exhibits advantages over conventional vibrational spectroscopies such as Raman scattering and IR absorption by providing chemically selective signals. Despite its utility, the application of 2D IR spectroscopy has been greatly limited owing to complex and expensive apparatus as well as the expertise required and difficulties associated with building them.[3] Although novel techniques such as pulse shaping and upconversion detection may enable to overcome the complexities associated in making 2D IR measurements, these techniques are believed to adversely impact the limit of detection and signal-to-noise ratio (S/N) enough to make certain experiments inaccessible, typically those of weak chromophores in dilute solutions such as proteins.[3]

Typically, 2D IR spectroscopy requires high sample concentrations ($\geq$ 1 mM) because the signal depends on multiple laser pulses interacting with the sample. Thus, improvements that enhance the 2D IR signal so that low analyte concentrations ($<<$ 1 mM) become accessible, while not being at the expense of S/N, would open up a wide range of applications of this powerful and selective spectroscopic method.

Optical properties of molecules undergo significant changes once adsorbed to metallic structures with nanoscale properties, giving rise to surface enhanced spectroscopic techniques, which allows the problems associated with S/N to be overcome efficiently. A well-known example is Surface Enhanced Raman Scattering (SERS), where significant enhancements (typically $10^6$ - $10^8$, or even larger) are possible when an analyte is near a nanoparticle or a surface with nanoscale roughness,[4-6] which can lead to single molecular detection, via the otherwise faint Raman scattering properties of molecules.

Although less understood mechanistically, the infrared (IR) analogue, Surface Enhanced Infrared Absorption (SEIRA) spectroscopy is presently emerging as a powerful tool in chemical analysis owing to its many desirable characteristics. Of note, molecules adsorbed on metal island films or metal colloids show 10 - 1000 times more intense infrared (IR) absorption as compared to conventional measurements made in the absence of nanoparticles, which today, is commonly referred to as SEIRA.[7] However, to date, SEIRA has only received limited attention, especially compared to SERS, as the enhancements observed in SEIRA are typically much less than those observed in SERS.

However, multi-dimensional spectroscopies such as 2D IR provides an advantage to the surface enhancements via the involvement of multiple laser pulses. For example, surface enhanced two dimensional infrared (SE-2D IR) spectroscopy, would allow higher order enhancements to be achieved compared to SEIRA,[8] owing to the multiple laser pulse interactions employed herein. Specifically, according to a previous account by Donaldson and Hamm, 2D IR spectra are measured via signals originating from a third order nonlinear polarization $P$ induced in an isotropic sample by an electric field $E(t)$ comprised of several laser pulses such that:

$$\vec{P}^{(3)}(t)=\int_0^\infty dt_3\int_0^\infty dt_2\int_0^\infty dt_1 R^{(3)}(t_3,t_2,t_1)\vec{E}(t-t_3)\vec{E}(t-t_3-t_2)\vec{E}(t-t_3-t_2-t_1) \quad (1.1)$$

Here, $R^{(3)}$ is a third order response function which is a four time-point correlation function of the dipole operator $\mu(t)$.[8] The radiated third order field is projected onto a forth local oscillator field to obtain the heterodyned signal such that:

$$S \propto \vec{E}_{LO}(t).\vec{P}^{(3)}(t) \propto \vec{E}_{LO}(t).\vec{E}^{(3)}(t) \quad (1.2)$$

The projection of the incident field onto the ensemble distribution of transition dipoles and the third order induced dipole field projection onto the local oscillator field are orientationally averaged.[8] The averaged result at the semi-impulsive limit can be written as;

$$S \propto \left\langle \left(\mu(t_3).\vec{E}(t_3)\right)\left(\mu(t_2).\vec{E}(t_2)\right)\left(\mu(t_1).\vec{E}(t_1)\right)\left(\mu(t_0).\vec{E}(t_0)\right)\right\rangle \quad (1.3)$$

Consider the enhancement contributions to the electric fields to be of the form;

$$\vec{E}(t)=L\vec{E}_0(t) \quad (1.4)$$

where $L = L(R,\theta,\phi)$ is the local field enhancement factor. Hence, now the signal can be rewritten as:

$$S \propto \left\langle \left(\mu(t_3).L\vec{E}_0(t_3)\right)\left(\mu(t_2).L\vec{E}_0(t_2)\right)\left(\mu(t_1).L\vec{E}_0(t_1)\right)\left(\mu(t_0).L\vec{E}_0(t_0)\right)\right\rangle \quad (1.5)$$

Which can be further simplified to give;

$$S \propto L^4\left\langle \left(\mu(t_3).\vec{E}_0(t_3)\right)\left(\mu(t_2).\vec{E}_0(t_2)\right)\left(\mu(t_1).\vec{E}_0(t_1)\right)\left(\mu(t_0).\vec{E}_0(t_0)\right)\right\rangle \quad (1.6)$$

which clearly indicates that the total field enhancement scales as $L^4$. Note that analogous to the framework discussed above, linear spectroscopy has only two laser pulse interactions and hence the signal there would only be proportional to $L^2$. Therefore, we can conclude:

$$Enhancement_{SE-2D\ IR} = \left(Enhancement_{SEIRA}\right)^2 \qquad (1.7)$$

Indicating that even modest enhancements in SEIRA can be manifested by significant enhancements in SE-2D IR, thereby allowing the challenges associated with S/N to be easily overcome. Interestingly, coupling SEIRA and SE-2D IR measurements will allow efficient quantification of the signal enhancements while at the same time contributing towards increasing the understanding of the surface enhancement mechanism (*vide infra*).

The overall objective of the investigations discussed here is the development of a model system for solution-phase SE-2D IR spectroscopy. Three specific objectives are believed to assist in achieving this ultimate objective as have been summarized in Figure 1.1. Namely; (1) understanding and controlling nanoparticle stability in solution, (2) identifying spectroscopic features of infrared surface enhancements, and (3) developing material with infrared plasmonic properties. These specific objectives will be dealt with separately in detail in the subsequent chapters.

## 1.2 Nanoparticle Stability: Improved Parametrization of Theoretical Modelling

Structural stability, or in other words, preserving the architectural integrity of nanoparticles for prolonged durations, potentially under ambient and/or application conditions, is an overarching challenge to all contemporary nanotechnology research.[9,10] Thus, enormous importance is placed on increasing the comprehension of what we know about how nanoparticles, specifically those of technological relevance, would behave under various environments. All nanomaterials, nevertheless, are high in surface energy compared to their bulk counterparts, and hence, in attempt to minimize their energy,

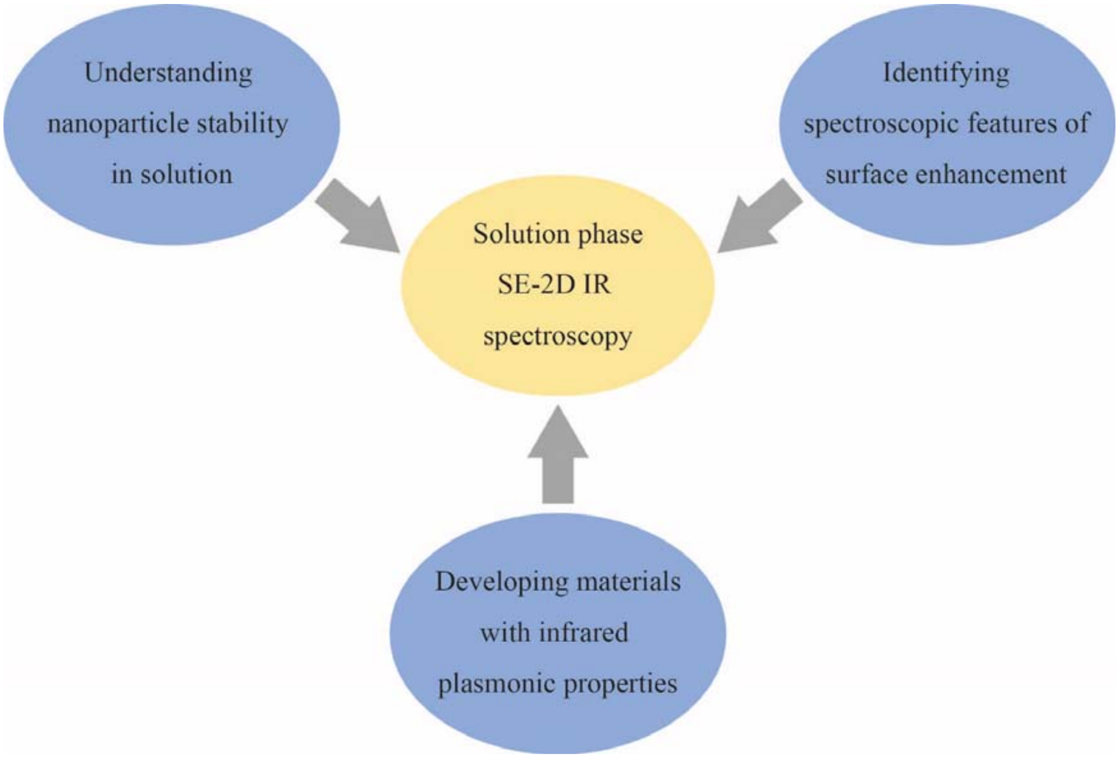

Figure 1.1 The schematic representation of the objectives of this study. The overall objective of this study is the development of a model system for solution-phase SE-2D IR spectroscopy. Three specific objectives, namely; (1) understanding and controlling nanoparticle stability in solution, (2) identifying spectroscopic features of infrared surface enhancements, and (3) developing material with infrared plasmonic properties, are believed to assist in achieving this ultimate objective.

nanomaterials form large clusters of nanoparticles upon collision, commonly referred to as aggregates, thereby often losing their nanoscale properties.

This aggregation process, however, may be limited by the presence of an energetic barrier that must be overcome in forming aggregates and/or by the existence of a local minimum where nanoparticles are stabilized via weak interactions, thus forming reversible agglomerates as depicted in Figure 1.2. Importantly, aggregation can be kinetically controlled by the energetic barrier, allowing the nanoparticles to preserve their nanoscale properties for short or even prolonged durations. Despite its significance, nanoparticle stability is often loosely defined in literature. Herein, we define such transitory stability, or 'metastability' of nanoparticles as the maintenance of chemical and physical properties while preserving the innate structure of the nanomaterial. Importantly, knowledge of the metastability of a material is key to the successful design, development, and integration of all nanomaterials into functional nanotechnology devices and applications.[10]

Gold (Au) nanoparticles are often used in functional nanotechnology and are ubiquitous in many chemical,[11,12] medical,[13,14] biological,[15] as well as electronic applications.[16] Often, the Au surface is functionalized by chemi- or physisorbed organic ligands at the nanoparticle surface as to tailor the nanoparticle properties to enhance applicability and/or colloidal stability.[17] Self-assembly of alkanethiols on Au that incorporate the sulfhydryl (-SH) linkage at the surface is a common and successful strategy of surface functionalization,[18] which has enabled the widespread use of gold nanoparticles in many scientific applications as well as in basic studies on interfacial chemistry.[19] Previous studies have shown that the chemical and physical properties of gold nanoparticles as well as their thermodynamic stability are dictated by the surface chemistry

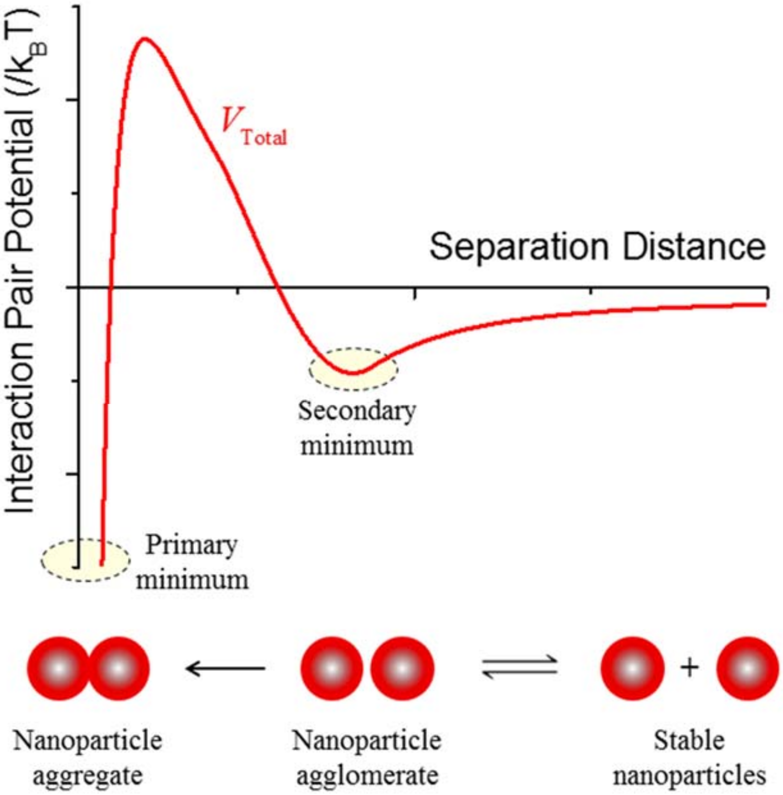

Figure 1.2 A typical total interaction potentials curve between a pair of nanoparticles that is used for predicting stability according to the xDLVO theory. As can be seen, the pair experiences no net attractive or repulsive interactions at large separation distances. At moderate separations, the particles are trapped in a secondary (local) minimum, producing reversible agglomerates. Eventually, particles will accumulate sufficient energy to overcome the energy barrier, thereby falling into the primary minimum where thermodynamic stability is achieved via the formation of large nanoparticle aggregates.

of the functionalized nanoparticles. For example, surfactant coated gold nanoparticles are known to exhibit electrically conducting,[20] insulating,[21] or even rectifying,[22] depending on the surface chemistry of the nanoparticles.

Although the properties of nanoparticles that gives rise to their wide ranging applicability has been well studied, it is often challenging to prepare nanoparticle with predictable and reproducible properties under ambient or application conditions. Interestingly, surface functionalization may induce or resist the inherent stability of nanoparticles via the replacement of the surface charges with uncharged or charged ligand moieties. Generally, the physico-chemical properties of the ligands used for surface functionalization have a greater influence on the aggregation behavior of functionalized gold nanoparticles than either their core composition or particle size.[23] Predicting the surface chemistry driven interactions among and the ensuing stability of nanoparticles suspended in a medium is, therefore, of primary importance for all nanoparticle applications. Commonly, this is achieved via the classical DLVO (Derjaguin, Landau, Verwey, and Overbeek) theory, or the extended DLVO (xDLVO) theory (when non-classical interactions are present), where the stability is predicted by modelling the interactions that exist between pairs of nanoparticles.

According to the xDLVO framework, the relevant interaction contributions for surface functionalized nanoparticles are van der Waals, electrostatic and steric (osmotic and elastic) interactions (*vide infra*) as shown in Figure 1.3.[24-26] As shown here, the presence of surface functional groups results in additional steric interactions via the mutual interactions of the ligands on each nanoparticles and also the ligands with the nanoparticle cores. Quantification of each interaction above is specific to the type of nanoparticles,

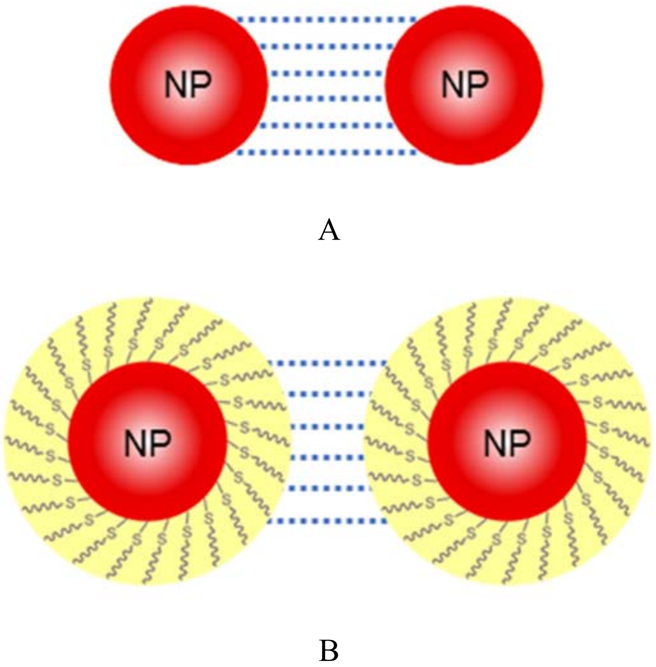

Figure 1.3 The interactions between a pair of (A) bare and (B) functionalized spherical nanoparticles. Bare nanoparticles predominantly interact through van der Waals and electrostatic interactions, whereas additional steric interactions exist between functionalized nanoparticles resulting from the mutual interactions of the ligands on each nanoparticles and also the ligands with the nanoparticle cores.

surface functionality, as well as the environment in which the nanoparticles are suspended, while the total interaction potential obtained by summing the individual contributions is used for eventual prediction of nanoparticle stability. Thus, the challenge in theoretical prediction of functionalized nanoparticle stability lies on determining the individual interactions between nanoparticles with sufficient accuracy. Approximations or assumptions in determining individual interaction potentials, however, are common in nanoparticle stability modelling, while often leading to inaccurate predictions.

Herein, synergistic contributions from a size-dependent Hamaker constant, surface potentials and ligand tilt angles produce an empirically consistent application of the xDLVO theory accounting for van der Waals, electrostatic, and steric interaction potentials, which is experimentally verified using carboxylic acid functionalized gold nanoparticles in solution. Gold nanospheres with ~13 nm diameters are used here owing to their well-known monodispersity in particle size while their properties are modified via the self-assembly of alkanethiols on the gold surface, which promote/hinder inter-particle interactions as governed by the packing density and effective film thickness determined from the ligand length and tilt angle. Therefore, thioctic acid (TA), 6-mercaptohexanoic acid (MHA), and 11-mercaptoundecanoic acid (MUA) are used to systematically modify the surface chemistry of the gold nanoparticles.

In order to provide an accurate description of the interactions between these materials modifications to the xDLVO theory are adopted in terms of the Hamaker constant, surface potentials, and ligand tilt angles. First, a size-dependent Hamaker constant of 3.7 x $10^{-19}$ J for ~13 nm diamater gold nanoparticles is incorporated into van der Waals contributions by assuming size-dependence of the imaginary part of dielectric permittivity of the metal. Second, surface potentials contributing to the electrostatic interactions are estimated assuming a Poisson-Boltzmann charge distribution and a uniform local dielectric constant. Finally, the effective SAM thickness which governs the steric interactions for the three selected ligands is quantified using localized surface plasmon resonance (LSPR) sensitivity towards the changes in the local dielectric environment. Interaction pair potentials between functionalized nanoparticles modelled via the inclusion of these three modifications to xDLVO theory provides an accurate description of functionalized gold nanoparticle interactions which is experimentally verified using the electrical properties of the carboxylic acid functionalized gold nanoparticles. Interestingly, these improvements in xDLVO theory could be expanded to model the interactions between and predicting the properties of other functionalized solution phase nanoparticles, thereby facilitating the rational design of functionalized nanomaterials for novel nanotechnology applications.

## 1.3 Mechanistic Understanding of Signal Enhancement in SE-2D IR Spectroscopy

To date, one example of using surface enhancement via gold nanoparticles for small molecule detection was published.[27] Gold nanoparticles with diameters ranging from 6.5 - 10 nm provided 4x to 100x signal enhancements for the Amide I bands of amide-functionalized thiols. While these results are encouraging, no systematic studies of the effects of the plasmonic properties of the particles or the role of inter-particle spacing in agglomerates and aggregates were evaluated. Such a study is essential to assess the potential for 2D IR spectroscopy as an effective analytical tool in chemical investigations.

The working hypothesis of this study is that SE-2D IR enhancements will depend on (1) the optical properties of the primary nanoparticles, (2) the inter-particle spacing, and (3) the wavelength range for excitation. We predict that the excitation and enhancement properties for 2-color SE-2D IR experiments could differ from those for 1-color SE-2D IR. By controlling the plasmonic properties of the primary nanoparticles and the inter-particle spacing, we can evaluate the relationship between the nanomaterial properties and 2D IR signal enhancements. Second, interrogation of functional groups with vibrational transitions at various wavelengths will allow us to understand how the wavelength-dependent properties of the nanoarchitectures affect observed enhancements. Finally, we can employ 2-color SE-2D IR to facilitate selective sensing by measuring couplings and energy transfer between functional groups on target molecules.

Direct and accurate determination of the enhancement factor is important for SE-2D IR. To quantify and compare enhancement factors, we can prepare analyte samples with and without nanostructures and measure both infrared absorption and 2D IR spectra. While traditional SEIRA signals scale linearly with analyte concentration, pathlength, molar absorptivity, and enhancement factor; SE-2D IR signals scale linearly with analyte concentration and pathlength but quadratically with both molar absorptivity and enhancement factor. Thus, the enhancement factor is quantified by taking a ratio of the ratios of the 2D IR to IR absorption signals with and without the nanostructures as follows:

$$\text{Enhancement factor} = \frac{\left(\dfrac{\text{SE-2D IR signal}}{\text{SEIRA signal}}\right)}{\left(\dfrac{\text{2D IR signal}}{\text{IR signal}}\right)} = \frac{\left(\dfrac{fcl\varepsilon^2\alpha^2}{cl\varepsilon\alpha}\right)}{\left(\dfrac{fcl\varepsilon^2}{cl\varepsilon}\right)} = \alpha \qquad (1.8)$$

where $f$ is an instrumental factor that accounts for laser power and focusing conditions in the 2D IR measurements, $c$ is the analyte concentration, $l$ is the pathlength of the cell, $\varepsilon$ is the molar absorptivity of the transition, and $\alpha$ is the enhancement factor.

The model for electromagnetic enhancements of SERS is that the localized surface plasmon resonance of the nanoparticles leads to electric field enhancements located at the surface of and junctions between the nanostructures that result in the observed increase in Raman scattering.[28] In SEIRA, the same mechanistic model may apply if the plasmon resonance is shifted into the IR region of the electromagnetic spectrum where IR electric field enhancements can be induced.[29] While still not fully understood, this model explains many phenomena in SEIRA, but these modeled enhancement predictions are typically one to two orders of magnitude smaller than experimentally observed enhancements.[30]

A competing model for SEIRA enhancement suggests that molecules near the surface induce an image dipole of the dipole-active vibrational modes in the metal thereby perturbing the optical properties of the metal nanostructure.[30] Consequently, the vibrational absorbance of observed analytes should increase because of the impact of the molecular vibrational mode on the optical properties of the metal. In other words, the metal functions as an antenna that senses the dipolar oscillations of the molecule. This alternative mechanism successfully explains observed SEIRA signal enhancements for coinage metals such as Ag and Au as well as for transition metals such as Pt, Pd, Rh, Ru, Ir, Sn, Fe, In, and Pb. We expect that the two contributions proposed for SEIRA will also be important in understanding the mechanism of enhancement in SE-2D IR.

## 1.4 Solution Phase Surface Enhanced Infrared Absorption via Nanoparticles Anchored Molecular Moieties

Generally, the phenomena of infrared surface enhancement has been studied much less than its Raman counterpart and currently there is heavy debate about its exact mechanism as discussed above. There are reports that claim, the nanoparticle plasmonics play the same role as that in SERS,[31] whereas some argue that the enhancement principally stems from the generation of image charges in the nanoparticle substrates, making the plasmonic contributions less significant.[32] Clearly, further investigation on infrared surface enhancements are imperative in order for an exact consensus to be achieved on the above topic. Interestingly, enhancement in the infrared absorption are manifested by changes in spectral features, such as derivative-like of Fano type lineshapes as have been previously reported.[7,33] These spectral anomalies can hence be utilized in order to identify infrared signal enhancements and more importantly to determine the exact mechanism by which such phenomena occurs.

Although the literature on SE-2D IR is scarce to date,[8] SEIRA has already been widely applied in the analysis of trace chemicals,[34] biosensing and immunoassays,[35,36] characterization of thin organic films and solid surfaces,[37,38] and in the in situ studies of electrochemical dynamics.[39] Hence, the applications of SEIRA had been generally limited to the use of solid state nanostructures as the substrate. However, various novel morphological forms of nanostructures have been successfully synthesized such that they are stably suspended in solution for prolonged periods of time. These nanostructures may potentially provide surfaces for analyte molecules in solution to be bound, while being stably suspended in solution, thereby allowing surface-enhancements to be observed in the solution phase. Extrapolation of surface enhancements using IR in the solution phase would be imperative in increasing the efficiency, sensitivity, as well as selectivity of the many chemical analyses where a solution phase is essential, hence allowing widespread applicability of SEIRA and SE-2D IR spectroscopies.

Herein, first steps towards observing a SEIRA signal from an analyte bound to a suitable nanoparticle surface using nanoparticle suspensions are discussed. Typically, the effects of the substrate and the chromophore, need to be evaluated for SEIRA studies. The choice of substrate was non-trivial as stable dispersion in solution was desired. Hence, various morphological forms of gold nanoparticles with previous known solution phase stability; namely, nanospheres, nanostars, as well as nanorods (not discussed here) are investigated as potential SEIRA substrates. Further, the efficacy of various molecules containing $N^{3-}$, $SCN^{-}$, or CH moieties as potential IR chromophores are investigated. Complementary analysis (via UV/Visible spectroscopy and SERS) are utilized as needed.

It was observed that $SCN^{-}$ in the presence of gold nanospheres (diameter ~ 20 nm) caused anomalous spectral lineshapes to be observed. Such spectral features are typically regarded as hallmark features of SEIRA spectroscopy,[7] and hence the experiments conducted herein provided direct evidence of SEIRA via the combination of shifted frequency and dispersive lineshapes in the infrared absorption spectra obtained. A detailed analysis and theoretical modelling of the spectroscopic origin of the anomalous lineshapes observed here allowed the above inference to be made effectively.

## 1.5 Engineering Nanostructures with Tunable Plasmonic Properties

Fabrication and synthesis of nanomaterial substrates for reproducible surface-enhanced vibrational spectroscopic signals are essential for any quantitative assay. Large enhancing substrates are currently being developed, manufactured, and sold. For instance, Renishaw used to sell (presently discontinued) a SERS substrate that is bound to a solid support that consistently generates signal enhancements up to $10^6$. When nanostructures are bound to a solid support, limitations of mass transport for trace molecules can increase detection time and limit detection capabilities. As a result, nanomaterials placed at liquid | liquid or liquid | air interfaces that rely on preferential radial diffusion could reduce the time required for detection. As with SERS and SEIRA spectroscopies, the signal enhancements in SE-2D IR experiments are expected to depend on the optical properties of the primary metal nanostructures. While much progress has been made in engineering enhancing substrates for SERS and SEIRA using lithographic methods, less development of ordered, non-lithographic substrates for SERS, SEIRA, and SE-2D IR has been realized.

We expect that either spikey nanoparticles or nanoparticles with aspect ratios greater than one will exhibit larger enhancements than nanospheres.[28,31,40] For instance, gold nanorods with varying aspect ratios have been previously synthesized,[41-45] while synthetic modifications can be employed so that the nanoparticles are closely spaced.[31] Then, the localized surface plasmon resonance maximum wavelength is red-shifted for SERS studies, and there are broad optical features in the infrared for 2D IR studies. The gold nanorod aspect ratios can be controlled by varying the concentrations of stabilizing ligands and growth catalysts.

Solution-phase stability of primary and assembled nanoparticles at interfaces must be considered to successfully develop SE-2D IR. For instance, primary nanomaterials functionalized with amine or carboxylic acid terminated groups[46] will facilitate physical stability.[43-45] These molecules are available with tunable chain lengths (i.e., spacer layer thicknesses) and will provide nanoparticle stability in both low and high temperature environments, dried and hydrated states (for spectroscopic measurements at long wavelengths of low frequency phosphate modes and agents that react with water), as well as in a variety of solvent systems. While these covalently attached ligands will exhibit superior performance in terms of stability, these ligands may reduce the interaction of analyte molecules for detection. As a result, weakly binding ligands such as surfactants and zwitterions could be used to maintain control over inter-particle spacing upon assembly and nanoparticles stability but would allow target molecule interaction with the nanoparticles surfaces.

Here, we demonstrate the synthesis of gold nanostars via a simple, seedless, one-pot synthetic procedure, where 2-[4-(2-hydroxyethyl)-1-piperazenyl]propanesulfonic acid (EPPS) is used as the reducing agent as well as the template that drives anisotropic growth. The synthesized gold nanostars indicated plasmonic behavior extending into the infrared wavelengths. Furthermore, the plasmonic properties of these structures could be easily tuned by simply changing the buffer concentration used during synthesis. Here, the plasmon tuning was manifested via manipulating the nanoarchitectures with varying buffer concentrations, as was revealed by the detailed morphological analysis. Interestingly, the gold nanostars synthesized here indicate promising plasmonic behavior for use in SEIRA, SE-2D IR as well as other surface-enhanced spectroscopic techniques.

## 1.6 Significance of Developing SE-2D IR Spectroscopy

While vibrational modes in SERS spectra are relatively narrow versus IR spectral features, SERS spectra can become very complicated when multiple molecules are present in a sample. Chemometric methods, such as partial least squares,[47,48] can be used when a SERS spectrum containing no more than ~10 analytes is embedded within a complex background, but this requires additional processing time before positive identification and quantification of analytes can be made. In contrast, SE-2D IR can be used to measure couplings and energy relaxation pathways within molecules with multiple functional groups by exciting high frequency vibrations and probing lower frequency fingerprint modes. The couplings and energy-transfer pathways probed by SE-2D IR spectroscopy will provide a molecularly specific fingerprint that is characteristic of the connectivity of the probed functional groups. Furthermore, because the pattern of cross peaks is spread across two frequency dimensions, the 2D IR spectrum separates overlapping contributions allowing identification of target analytes even in complex mixtures. Hence, all efforts in increasing the efficiency and applicability of SE-2D IR is important in the design, development and application of novel tools for chemical analysis.

# CHAPTER 2

# IMPROVED PARAMETRIZATION FOR XDLVO PREDICTIONS OF FUNCTIONALIZED GOLD NANOSPHERE STABILITY

## 2.1 Theoretical Modelling of Nanoparticle Stability and the xDLVO Theory

Assessing and controlling the stability of solution-phase nanoparticles is important for exploiting the chemical and physical properties of nanomaterials as well as determining their fate in complex environments.[49-51] Typically, achieving this control requires considerable experimentation. Ideal conditions are attained after a series of studies varying the nanoparticle composition, size, surface chemistry, and surface potential as well as solvent composition, synthetic approaches, and washing conditions.[52-55] Recently, predictions that utilized these nanoparticle properties were exploited to develop stability maps for quantum dots and ZnO nanoparticles.[55] These optimizations are often time consuming and can lead to anomalous results as environmental factors such as temperature, pH, and the presence of small molecules impact nanoparticle stability,[56] but are not always independently controlled or varied.

Both experimental and computational studies can be used to assess nanoparticle stability. Traditional experimental approaches include atomic force microscopy,[57] measurements of optical or electrical properties,[49,50,58] sedimentation,[59] and structural characterization.[51] Calculations use a variety of models including depletion forces,[60]

---

Adapted from *Improved Parametrization for xDLVO Predictions of Functionalized Gold Nanosphere Stability*, Wijenayaka, L. A.; Ivanov, M. R.; Cheatum, C. M.; Haes, A. J. *The Journal of Physical Chemistry C* **2015**, *119*, 10064.

Lifschitz theory,[56,61] DLVO, and extended DLVO (xDLVO) theories.[24-26,62] According to Lifschitz theory, van der Waals interactions between two nanoparticles arise from the bulk electrodynamic response of one object interacting with a second object, resulting in electromagnetic fluctuations in both objects.[63] These van der Waals attractions are opposed by several repulsive forces including electrostatic repulsions as well as contributions from surface chemistry and the medium.[64] The competition between these contributions determines nanoparticle stability and fate in a way that depends on inter-particle separation distances.[65,66]

Predicting the interactions among, and the ensuing stability of nanoparticles suspended in a medium is, therefore, of primary importance for all nanoparticle applications. Commonly, this is achieved via the classical DLVO (Derjaguin, Landau, Verwey, and Overbeek) theory, which simplifies nanoparticle interactions as being van der Waals or electrostatic in origin, or the extended DLVO (xDLVO) theory when non-classical interactions are present, where the stability is predicted by modelling the interactions that exist between pairs of nanoparticles.[26] The classical DLVO theory often fails in accounting for all the different non-classical interactions in a given nanoparticle system. For example, aligning of electron spins gives rise to magnetic attractions in magnetic nanoparticles,[67] while the entropic penalty of separating hydrogen bonds in water may lead to hydrophobic (Lewis acid-base) interactions in others,[68,69] both of which are not accounted by the classical DLVO theory. In essence, therefore, many factors such as nanoparticle shape, structure, composition, as well as the presence of nanoparticle surface modifications challenge the DLVO stability predictions.[26]

For functionalized nanoparticles, additional non-classical interactions exist as a result of the surface functional groups sterically interacting with ligands on other nanoparticles as well as other nanoparticle cores themselves.[24,25] According to the xDLVO framework, therefore, the relevant interaction contributions for surface functionalized nanoparticles are van der Waals, electrostatic and steric (osmotic and elastic) interactions.[24-26] Reasonable, qualitative agreement was resulted in previous studies where the stability of functionalized nanoparticles have been predicted using the above interaction contributions.[24,25] Quantification of each interaction above, however, is specific to the type of nanoparticles, surface functionality, as well as the environment in which the nanoparticles are suspended. Thus, the challenge in theoretical prediction of functionalized nanoparticle stability lies on determining the individual interactions between nanoparticles with sufficient accuracy. Approximations or assumptions in determining individual interaction potentials, however, are common in nanoparticle stability modelling. Although such approximations allow the potentials to be easily estimated and sometimes even the stability to be reasonably predicted, more often it may easily lead to both qualitatively and quantitatively inaccurate predictions.

## 2.2 Common Misconceptions in Modelling Nanoparticle Stability

van der Waals attractions dominate inter-particle interactions between nanoparticles at relatively short separation distances, while the calculation of van der Waals interactions ($V_{vdw}$) between particles requires knowledge of their Hamaker constant (*vide infra*). Typically, the Hamaker constant had been considered to be a size and morphology independent constant that depends on the electron densities of the interacting materials and the dielectric properties of the intervening media,[70-72] allowing the Hamaker constant of the bulk material to be utilized as that of nanoparticles. According to more recent findings, however, the Hamaker constant of noble metals exhibit significant size dependence, where the Hamaker constant exponentially increase as the particle size falls below the mean free path of electrons in the bulk metal. Such size dependence of the Hamaker constants of nanoparticles, nevertheless, has not been incorporated into nanoparticle interaction modelling to date, often leading to the underestimation of van der Waals interactions between nanoparticles, especially at relatively short inter-particle separations where van der Waals interactions are predominant.

Further, electrostatic interactions ($V_{ele}$) between particles are strongly dependent on the nanoparticle surface potential, $\psi_0$ (*vide infra*), thus the proper estimation of $\psi_0$ is central for the determination of $V_{ele}$ between nanoparticles. In some cases, however, $\psi_0$ is approximated to the Stern potential ($\psi_\delta$), which is the potential at the Stern plane (plane of closest approach of the ions to the surface) to account for the finite size of ions around nanoparticles, allowing $\psi_0$ to be estimated using surface charge density.[73] Nevertheless, it is more practical to use an experimentally determined value for $\psi_0$, rather than a theoretical approximation in order to accurately determine the electrostatic interactions. Although $\psi_0$ cannot be directly measured, zeta potential ($\zeta$), which is the potential measured at a distance that is equal to the Debye length away from the charged surface (slipping plane) provides an indirect estimation of $\psi_0$. For simplicity, it is a common practice in DLVO calculations to consider $\psi_0$ to be equal to $\zeta$,[74-77] assuming the Stern plane and the slipping plane are nearly identical.[73] Although this assumption is valid at high ionic strength where the ions are forced to be closer to the surface, it often fails at reasonable values of ionic strength where nanoparticle stability may retain, thus leading to known errors via the under-estimation of $\psi_0$.

Nanoparticles are often functionalized with chemi- or physisorbed organic ligands, forming self-assembled monolayers (SAM) on their surfaces in order to tailor nanoparticle properties for targeted applications,[17-19,78] or to further promote colloidal stability.[79-81] Self-assembly of alkanethiols on gold is a common and successful strategy for surface functionalization which enables the widespread use of gold nanoparticles in many applications[82-84] and fundamental interfacial studies.[85] The presence of surface functionalized groups allows additional steric interactions to exist between nanoparticles, which are mainly elastic and osmotic in nature. The existence as well as the extent of these additional interactions relies on the inter-particle separation distances relative to the SAM thickness (*vide infra*). Thus, precise knowledge of the SAM thickness is crucial in order to accurately quantify the steric interactions between functionalized nanoparticles.

Commonly, one may consider the thickness of a SAM to be the same as the length of the molecule forming the monolayer via ordered assembly on the surface, thus allowing simple estimation of the SAM thickness. When an alkanethiol chain binds to a gold surface, however, the molecule is oriented with a tilt angle ($\theta$) that is measured from the surface normal,[86,87] causing the monolayer thickness to deviate from molecular length. Steric interactions provide a predominant contribution towards the total interactions between functionalized nanoparticles, especially when the nanoparticles are functionalized with long chain hydrocarbons. Approximation of SAM thickness to molecular length, therefore, often leads to misinterpretation of the steric interactions existing between functionalized nanoparticles.

Approaches to improve the prediction of solution-phase nanoparticle stability date back to the 1950s and continue today.[66,88-90] Based on these models, nanomaterials are synthesized and can be stored as stable suspensions for months.[91] Despite this success, predictions of nanoparticle stability often deviate significantly from experimental results.[56,91-93] Predictions of gold nanosphere stability are often qualitatively consistent with experiment,[88] but the underlying reasons for this stability are not well described. As gold nanosphere diameter increases, the stability of these materials has been described as increasing because of a variety of effects including kinetic retardation,[22] surface chemistry,[56,94,95] and solvation differences.[56] Although any or all of these may be involved, the relative importance of these contributions remains unresolved by current models at least in part because of uncertainties related to the parameters used as inputs.

In this study, methods to refine the values of several input parameters for xDLVO theory are considered for improving the predictability of functionalized gold nanosphere stability. Specifically, predictions using xDLVO theory are developed by employing surface potential estimations, size dependent Hamaker constants for gold nanoparticles, and experimental determination of monolayer thickness. In addition, the predictive capabilities of this approach to parameterizing xDLVO theory are validated through simple experimental measurements of the electrical properties of three functionalized gold nanosphere samples. These improvements in xDLVO input parameters yield consistency between the xDLVO predictions and experimental observations. Importantly, this exciting new approach can readily be extended and adapted for future studies of nanomaterials of various functionalities, shapes, and sizes.

## 2.3 Mathematical Framework for Modelling the Interaction Potentials of Functionalized Nanoparticles

xDLVO theory models the pairwise interaction potential between particles and can predict the stability of solution-phase nanomaterials.[24-26] Nanoparticles in solution undergo collisions via Brownian motion, but nanoparticle solutions will remain kinetically stable if the interaction pair potential barrier ($V_{max}$) is greater than ~16/$k_BT$.[96,97] Within the xDLVO framework, functionalized nanoparticles interact through van der Waals, electrostatic, and steric (osmotic and elastic) contributions to the potential energy.[24-26] Quantification of each of these potentials depends on nanoparticle composition, surface functionality, as well as the environment in which the nanoparticles are suspended. As a result, the challenge in theoretical prediction of functionalized nanoparticle stability relies on determining the individual interactions between nanoparticles with sufficient accuracy. Approximations for determining individual interaction potentials are, however, common in modeling nanoparticle stability,[70-77,98,99] and these approximations often lead to inaccurate estimation of the total interaction potentials, thus leading to inconsistent predictions of nanoparticle stability.[86,87] The following sections consider individual contributions to the total interaction potential from xDLVO theory and identify novel approaches for determining key parameters that are inputs to the theory. Thus, the quality of nanoparticle stability predictions based on xDLVO theory is improved.

## 2.4 Synthesis and Characterization of Carboxylic Acid Functionalized Gold Nanoparticles

Citrate stabilized gold nanoparticles were synthesized according to an established procedure using gold (III) chloride trihydrate ($HAuCl_4$) and trisodium citrate dihydrate (citrate) (Sigma Aldrich).[46] Once cooled and prior to functionalization, the nanoparticle solutions were filtered through 13 mm diameter, 0.45 μm nylon filters (Whatman). These nanoparticles were then functionalized with thioctic acid (TA) ($pK_a$ (COOH) = 4.75-5.30[1]), 6-mercaptohexanoic acid (MHA) ($pK_a$ (COOH) = 4.8[1]), or 11-mercaptoundecanoic acid (MUA) ($pK_a$ (COOH) = 4.6-5.0[1]) (Sigma Aldrich). For each self-assembled monolayer, 1 mL of 10 mM ligand (TA, MHA, or MUA) in ethanol was added to 10 mL of a 10 nM nanoparticle solution and stirred at 500 RPM for at least 60 hours at room temperature. The nanoparticles were then centrifuged at 11,500 RPM (8,797 x g) for 40 minutes, and the supernatant was replaced with water (obtained from a Barnstead Nanopure System and adjusted to pH 11 with 1 M NaOH). The rinsing procedure was repeated three times to ensure sufficient removal of unbound ligand. All nanoparticles were suspended in 5.5 mS/cm phosphate buffer with a pH of 7.3 and stored in brown vials until use. Except as noted, all chemicals were purchased from Fischer and used as received.

Nanoparticle homogeneity was characterized by transmission electron microscopy (TEM) using a JEOL JEM-1230 electron microscope. In all cases, 2 μL of a diluted nanoparticle solution (50 % mixture in ethanol) was applied to a carbon-formvar coated copper grid (400 mesh, Ted Pella or Electron Microscopy Sciences) and allowed to air dry.

The resulting images were analyzed using Image Pro Analyzer, and at least 100 nanoparticles were evaluated per sample.

Nanoparticle solutions were characterized using UV-Vis spectroscopy (USB 4000, Ocean Optics). Extinction maximum wavelength ($\lambda_{max}$) values were determined from the zero point crossing value of the first derivative of each spectrum using MathCAD. Nanoparticle solutions were diluted to 1 nM concentrations for zeta potential measurements (Delsa Nano, Beckman-Coulter), which were performed in triplicate using $H_2O$ diluent parameters (refractive index (n) = 1.3328, viscosity ($\eta$) = 0.8919 cP, and dielectric constant ($\varepsilon$) = 78.4) at 25° C. A flow cell configuration was used for all measurements, and data were fit using the Smoluchowski theory.

Electrical measurements were performed using a Beckman Coulter P/ACE MDQ capillary electrophoresis instrument and fused silica capillary (internal diameter = 75 μm, outer diameter = 360 μm) with an external polyimide coating (Polymicro). Current differences were monitored for a constant applied electric field maintained at 332 V/cm (20 kV, normal polarity) at a constant temperature of 25°C. Prior to electrical measurements, the capillary was conditioned using the following procedure: 0.1 M $HNO_3$ (20 psi for 5 minutes), $H_2O$ (20 psi for 2.25 minutes), 1 M NaOH (20 psi for 2.25 minutes), $H_2O$ (20 psi for 2.25 minutes), 250 mM phosphate buffer (20 psi for 3 minutes), and 30 mM phosphate buffer either with or without nanoparticles (20 psi for 3 minutes). Nanoparticle electrical effects were monitored using a conditioned, fused silica capillary that was filled with 1 or 5 nM functionalized nanoparticle solutions before applying a potential. Changes in current were determined by averaging differences from at least five stable current measurements that were collected one minute after the potential was applied (i.e., when the current stabilized).

## 2.5 Electrostatic Pair Potential and Surface Potential Estimations

The electrostatic interaction potential ($V_{ele}$) between a pair of nanoparticles arises from long-range, electrostatic repulsions between the particles in a polar solvent. For spherical nanoparticles with identical radii, a, if the Debye length ($\kappa^{-1}$) is small (i.e., $\kappa a > 5$),[100] then $V_{ele}$ as a function of the edge-to-edge separation distance between the particles, s, is given by[100,101]

$$\frac{V_{ele}(s)}{k_B T} = \frac{2\pi \varepsilon_0 \varepsilon_r \psi_0^2 a}{k_B T} \ln\left(1 + e^{-\kappa s}\right) \qquad (2.1)$$

where $\varepsilon_0$ is the permittivity of vacuum, $\varepsilon_r$ is the relative permittivity of the solution, $\psi_0$ is the surface potential, $k_B$ is the Boltzmann constant, and T is absolute temperature (see Appendix A).

In practice, these variables are all known with the exception of the surface potential. Typically, surface potentials are not measured but approximated using either the Stern potential ($\psi_S$) or zeta potential ($\zeta$).[73-77] These approximations are only reasonable if the ionic strength of the solution is sufficiently high so that $\kappa^{-1}$ is small compared to the relevant separation distances for which the potential is to be evaluated.[73-77] Typically, nanoparticle solutions both for storage and application, however, use low or moderate ionic strength buffers (~mM concentrations).[1,102] Under these conditions, use of $\zeta$ values leads to a significant underestimation of $V_{ele}$.

To avoid the underestimation of electrostatic interactions between nanostructures, we calculate the surface potential by solving the Poisson-Boltzmann equation for a distribution of point charges that decay as a function of radial distance from the charged nanoparticle surface. The surface potential is then expressed as

$$\psi_0 = \zeta\left(1+\frac{1}{\kappa a}\right)\mathrm{e}^1 \tag{2.2}$$

which assumes that the local dielectric constant around a nanoparticle is independent of the radial distance from the surface, and the energy required to transport charges in solution depends only on Coulomb interactions.[63] This relationship holds when surface charge density is proportional to ion concentration,[103,104] and builds on well-established literature precedents.[63 101]

To illustrate the effects of this approach, Figure 2.1 shows the electrostatic interaction potential associated with the surface potential on a nanosphere surface for three typical ζ values including -15, -25, and -35 mV. These zeta potential values result in slowly decaying electrostatic pair potentials. When the two nanospheres are separated by 1 nm, the electrostatic interaction pair potentials remain significantly different from one another, i.e. 5.8, 16.4, and 32.3/$k_BT$ for nanoparticles with ζ of -15, -25, and -35 mV, respectively. In all cases, the potential decays asymptotically to zero at a ~6 nm separation distance. While this relatively long-range repulsive interaction potential provides some short-term stabilization of solution-phase nanoparticles, it is ultimately not enough to prevent nanoparticle flocculation.[105,106]

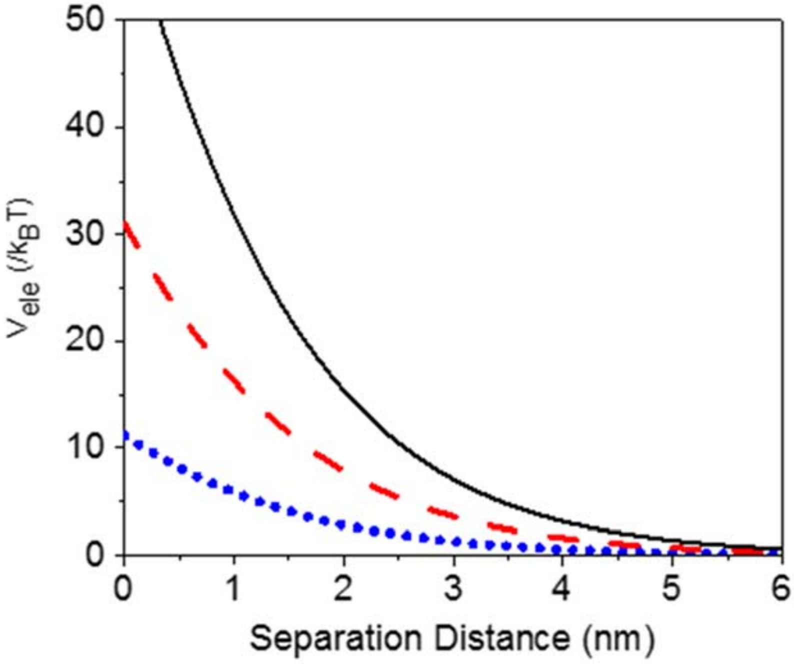

Figure 2.1 The electrostatic interaction potential as a function of separation distance for gold nanoparticles with an average radius of 6.5 nm immersed in a 63 mM ionic strength solution with zeta potentials of -35 (black solid line), -25 (red dashed line), and -15 mV (blue dotted line).

## 2.6 Size Dependence of the van der Waals Interactions between Gold Nanoparticles

Although electrostatic repulsions can provide short-term stabilization of gold nanospheres in solution, flocculation still occurs as a result of attractive interactions between nanostructures.[100,107] Specifically, the van der Waals attraction ($V_{vdw}(s)$) between two spherical nanoparticles with identical radii suspended in a medium can be calculated as follows[100,108]

$$\frac{V_{vdw}(s)}{k_BT} = -\left(\frac{A}{6k_BT}\right)\left(\frac{2a^2}{s(4a+s)} + \frac{2a^2}{(2a+s)^2} + \ln\left(\frac{s(4a+s)}{(2a+s)^2}\right)\right) \tag{2.3}$$

where A is the Hamaker or Lifshitz constant. The Hamaker constant depends on the complex dielectric permittivity of a material in a medium.[70-72] Hamaker constants are generally positive and used to model short-range attractive interactions between particles as a function of composition, geometry, and medium. Previously reported Hamaker constants for gold range from (0.9 - 3.0) x $10^{-19}$ J[72,109,110] in water and up to 4 x $10^{-19}$ J in a mixed water and/or hydrocarbon medium.[111] As a result of these large variations, choosing a Hamaker constant value for xDLVO theory can be difficult and are often selected to match experimental observations.

One aspect of the Hamaker constant that has largely been neglected in modeling the van der Waals interactions between nanoparticles is the size dependence of the dielectric properties of the material.[112] Recently, the Hamaker constant of silver was predicted to increase as nanoparticle diameter decreased.[70] This result was attributed to an increase in the imaginary part of the metal dielectric permittivity with decreasing nanoparticle size.

We develop a similar model for gold nanoparticles using an approach developed by Pinchuk[70] (see Appendix B for details). Size dependent Hamaker constants for a pair of gold nanoparticles interacting through a medium (M) are calculated from the equation

$$A_{NP-Medium-NP} = \frac{3\hbar}{4\pi}\int_0^{\infty}\left(1-\frac{2\varepsilon_M\left(i\omega\right)}{\varepsilon_{NP}\left(i\omega\right)+\varepsilon_M\left(i\omega\right)}\right)^2 d\omega \tag{2.4}$$

where ħ is reduced Planck's constant and $\varepsilon_{NP}(i\omega)$ and $\varepsilon_M(i\omega)$ are the dielectric permittivity of the nanoparticles and of the medium as a function of the imaginary frequency, respectively. Using the Drude model, the size and wavelength dependence of the imaginary part of dielectric permittivity of the metal is[70,112]

$$\Delta\left(\operatorname{Im}\varepsilon_{NP}\left(\omega,a\right)\right)=\frac{\omega_p^2}{\omega^3}\left(\frac{v_F}{a}\right) \tag{2.5}$$

where $\omega_p$ is the plasma frequency and $v_F$ is the Fermi velocity of the metal. Finally, the resulting size-dependent Hamaker constants are scaled so that they asymptotically approach the commonly reported Hamaker constant of bulk gold[113,114] ($2.5 \times 10^{-19}$ J).

Figure 2.2 (A) shows the Hamaker constant for gold nanospheres as a function of diameter calculated from this model. As expected, the Hamaker constant increases with decreasing radius. As specific examples, gold nanoparticles with radii of 2.5, 6.5, and 50 nm have calculated Hamaker constants of 4.0, 3.7, and $2.8 \times 10^{-19}$ J, respectively. When the nanoparticle radius increases, the size-dependence diminishes, and the Hamaker constant asymptotically approaches the bulk value. In contrast, typical gold nanoparticles prepared using standard citrate reduction methods exhibit ~13 nm diameters (6.5 nm

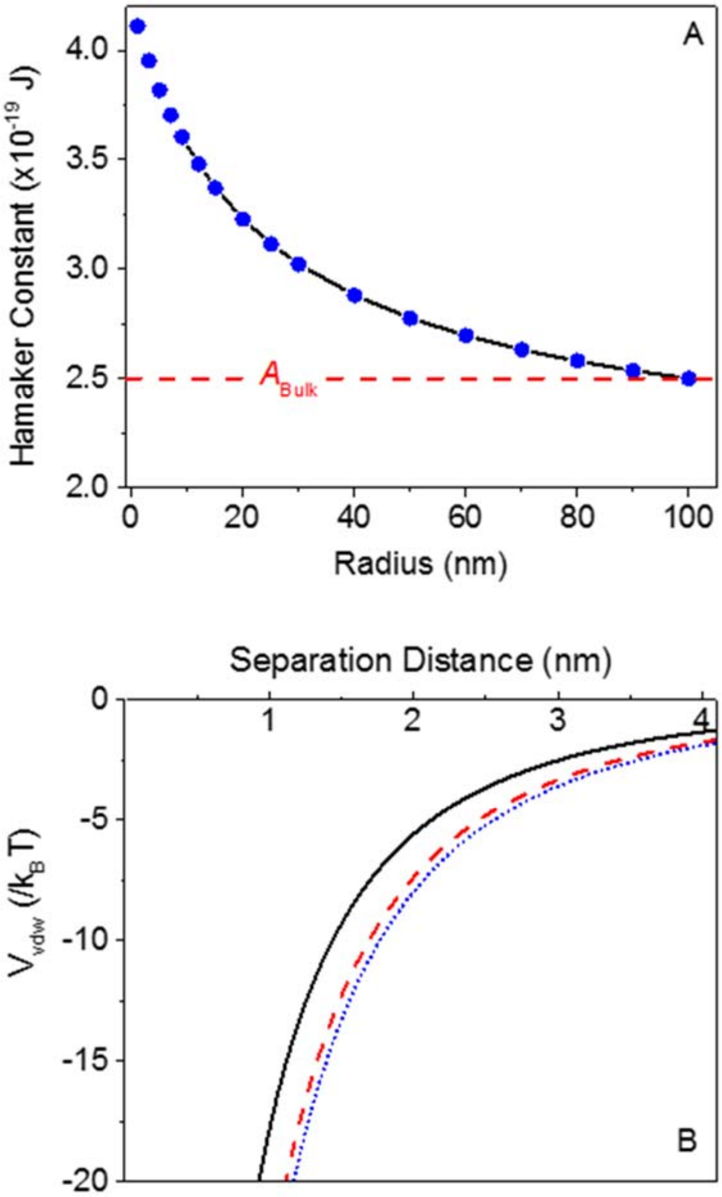

Figure 2.2 (A) Variation of the Hamaker constant as a function of nanoparticle radius. Each data point represents a calculated Hamaker constant, and the line is meant to guide the eye. (B) Variations in the van der Waals interaction potential ($V_{vdw}$) as a function of separation distance for gold nanoparticles with radii of 2.5 ($A = 4.0 \times 10^{-19}$ J) (blue dotted line), 6.5 ($A = 3.7 \times 10^{-19}$ J ) (red dashed line), and 50 nm ($A = 2.8 \times 10^{-19}$ J) (black solid line).

radius). The implications of this result suggest that these materials exhibit Hamaker constants ~50% larger than bulk gold thereby causing these materials to exhibit larger van der Waals attractive interactions and aggregate more readily than larger particles.

To demonstrate the influence of size dependent Hamaker constants on the van der Waals potentials between gold nanospheres, Figure 2.2 (B) shows the van der Waals interaction potential ($V_{vdw}$) as a function of separation distance for 2.5, 6.5, and 50 nm radius nanoparticles. As expected, the van der Waals attractive potential is negative and rapidly increases in magnitude as separation distance decreases. The effect of a size-dependent Hamaker constant, however, is that larger attractive interactions between smaller nanoparticles persist at longer separation distances vs. nanoparticles with radii greater than 50 nm. Although the variations in the attractive potential as a result of the size-dependent Hamaker constant may appear to be modest, it is important to realize that the attractive potential decays slowly to zero at large separation distances where the other contributions to the total interaction potential have already decayed to zero. Thus, even a modest change in $V_{vdw}$ can significantly affect nanoparticle stability because of the interplay between the different contributions at relatively long separation distances.

## 2.7 Steric Interactions between Functionalized Nanoparticles and Determination of Monolayer Thickness

In addition to the electrostatic and van der Waals interactions between nanoparticles, functionalized nanoparticles also exhibit osmotic and elastic interactions ($V_{osm}$ and $V_{ela}$), that are relatively short-range repulsive contributions to the total interaction potential, which can be used to kinetically stabilize nanoparticle solutions.[24,25,115] Models for both $V_{osm}$ and $V_{ela}$ assume that the ligands are uniformly distributed throughout the total ligand shell volume and depend critically on accurately determining the thickness of the monolayer.[24]

The osmotic potential arises from the competition of solvent molecules to solvate the ligands on the two nanoparticles at short inter-particle spacing (i.e., $s < 2t$ where t is the monolayer thickness)[24,115] and is zero at separation distances larger than twice the effective monolayer thickness. According to Vincent et al.,[115] for $t \leq s \leq 2t$ and nanoparticles with identical radii (a), $V_{osm}(s)$ is

$$\frac{V_{osm}(s)}{k_B T} = \frac{4\pi a N_a}{\upsilon_l}\phi_p^2\left(\frac{1}{2}-\chi\right)\left(t-\frac{s}{2}\right)^2 \tag{2.6}$$

where $N_a$ is Avogadro's number, $\nu_l$ is molar volume of the solvent, $\chi$ is the Flory-Huggins interaction parameter (0.45 for an ordered alkanethiol monolayer),[25] and $\phi_p$ is volume fraction of the ligand (see Appendix A). As the separation distance between nanoparticles decreases further ($s < t$), ligands on one nanoparticle can interact with the other nanoparticle. Thus, $V_{osm}(s)$ must also account for elastic deformations of the ligands[25,115]

$$\frac{V_{osm}(s)}{k_B T} = \frac{4\pi a N_a}{\upsilon_l}\phi_p^2\left(\frac{1}{2}-\chi\right)\left[t^2\left(\frac{s}{2t}-\frac{1}{4}-\ln\left(\frac{s}{t}\right)\right)\right] \tag{2.7}$$

where each of the parameters is again defined as in equation 2.6. When separation distances are shorter than the monolayer thickness ($s < t$), entropic effects arise from ligand tail compression[24] resulting in an elastic contribution to the potential ($V_{ela}$) given by[115]

$$\frac{V_{ela}(s)}{k_B T} = \left(\frac{2\pi a N_a}{M_W}\phi_p t^2 \rho_d\right)\left(\left(\frac{s}{t}\right)\ln\left(\frac{s}{t}\left(\frac{3-{}^{s}\!/_{t}}{2}\right)^2\right)-6\ln\left(\frac{3-{}^{s}\!/_{t}}{2}\right)+3\left(1-\frac{s}{t}\right)\right) \tag{2.8}$$

where $M_W$ and $\rho_d$ are the molecular weight and density of the (pure) ligand, respectively.

To demonstrate the effect of monolayer thickness on both $V_{osm}$ and $V_{ela}$, Figure 2.3 shows (A) osmotic and (B) elastic potentials between two gold nanospheres with monolayer thicknesses of 0.4, 0.8, and 2.0 nm. Both $V_{osm}$ and $V_{ela}$ are large, repulsive, and short-range potentials consistent with monolayer thicknesses. The osmotic potentials are all very large, $>100/k_BT$, at separation distances less than 1 nm and decay over a length scale equal to twice the monolayer thickness. The elastic potential, in contrast, is also repulsive but smaller in magnitude and proportional to monolayer thickness. These observations suggest that solvent-ligand interactions rather than the monolayer thickness itself dominate the repulsive forces between nanoparticles as separation distance decreases. In addition, because of the magnitude of these short-range interactions and their sensitivity to layer thickness, an accurate determination of effective monolayer thickness is necessary for accurately modeling the pair potential.

For well-ordered self-assembled monolayers (SAMs), monolayer thickness depends both on the molecular length and the tilt angle ($\theta$) of the surface-bound molecules relative to the surface normal.[86,87] Most SAMs form with a significant tilt relative to the surface normal, meaning that the ligand length is, by itself, a poor approximation for monolayer thickness. For example, ~30° tilt angles are commonly reported for alkanethiol monolayers.[116,117] The tilt angle, however, is often neglected in xDLVO calculations.[98,99]

As demonstrated previously, the shift in the localized surface plasmon resonance (LSPR) wavelength ($\lambda_{max}$) of gold nanoparticles provides an accurate measure of monolayer thickness.[118-120] Specifically, $\lambda_{max}$ is related to surface functionalization by the equation

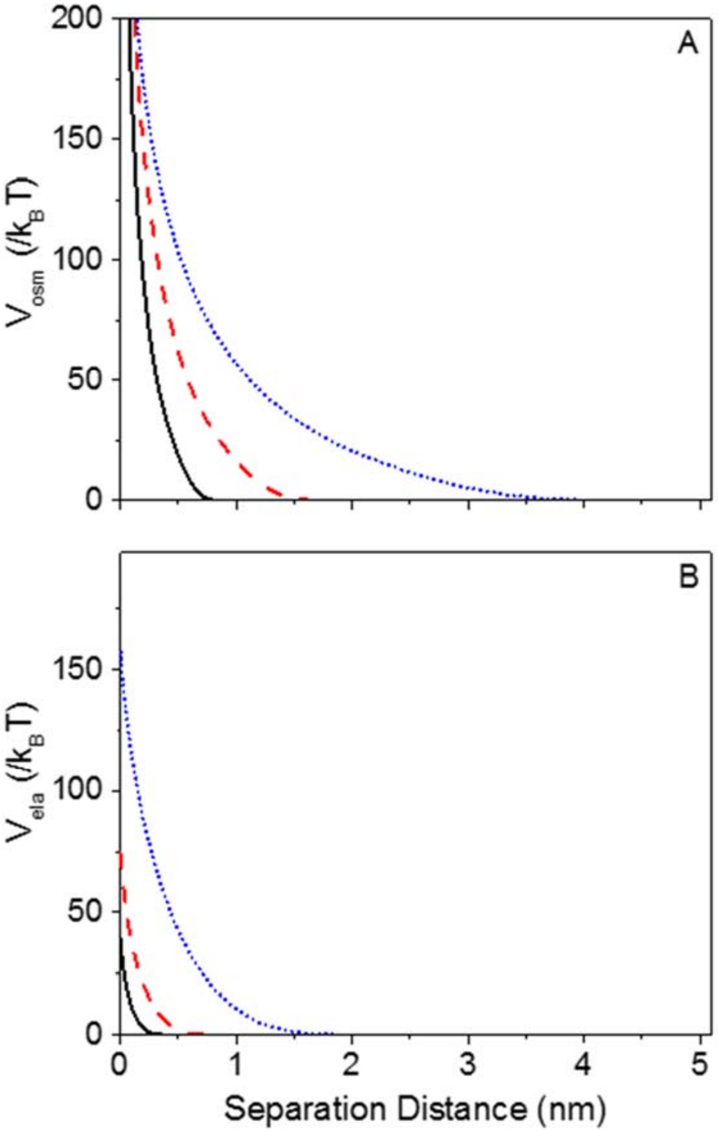

Figure 2.3 Effect of theoretical monolayer thickness (t) = 0.4 (black solid line), 0.8 (red dashed line), and 2.0 (blue dotted line) nm on the (A) osmotic ($V_{osm}$) and (B) elastic ($V_{ela}$) interaction potentials as a function of edge to edge separation distance (s) between two gold nanoparticles (radius = 6.5 nm, Ionic strength = 63 nm, zeta potential = -20.9 mV).

$$\lambda_{\max} = \lambda_{\max,original} + m\Delta n - m\Delta n^2 \tag{2.9}$$

where $\lambda_{\max,\text{original}}$ is the extinction maximum wavelength before surface functionalization, m is the refractive index sensitivity of the nanoparticles, and Δn is the change in refractive index resulting from surface functionalization. Assuming that the ligand refractive index is independent of surface coverage, Δn is related to effective monolayer thickness (t), local electromagnetic field decay length ($l_d$), refractive index of the bulk medium ($n_{\text{bulk}}$), and refractive index of the ligand ($n_l$) by the expression[119]

$$\Delta n = \left(n_l - n_{bulk}\right)\left(1 - \mathrm{e}^{\frac{-2t}{l_d}}\right) \tag{2.10}$$

These results provide a reliable relationship between the LSPR shift and the monolayer thickness. Further, this thickness is also expressed in terms of the ligand length (l) and the tilt angle (θ) as t = l cosθ. By uniquely combining these expressions, the tilt angle can be directly related to the extinction maximum wavelength ($\lambda_{\max}$) as

$$\theta\left(\lambda_{\max}\right) = \cos^{-1}\left(\left(\frac{-l_d}{2l}\right)\ln\left(1 - \frac{m - \sqrt{m^2 - 4m\left(\lambda_{\max} - \lambda_{\max,original}\right)}}{2m\left(n_l - n_{bulk}\right)}\right)\right) \tag{2.11}$$

Thus, the average tilt angle of a monolayer on a gold nanoparticle can be directly estimated using the $\lambda_{\max}$.

## 2.8 Implications of Parameterization on the Total Interaction Potential

The total interaction potential is the sum of the contributions described above, i.e. $V_{\text{total}}(s) = V_{\text{vdw}}(s) + V_{\text{ele}}(s) + V_{\text{osm}}(s) + V_{\text{ela}}(s)$. Ultimately, predictions of nanoparticle stability depend on the interplay between the individual contributions to this total interaction potential. It is clear that the short-range height of the repulsive barrier as well as the separation distance at which this repulsive contribution decays to zero are important for predicting nanoparticle stability. For a suspension of gold nanoparticles in Brownian motion (radius of 6.5 nm, a concentration 5 nM, and at a temperature of 25 °C), the rate of nanoparticle collisions is 14.6 collisions/s. The number of collisions per week, therefore, would be 8.83 x $10^6$, indicating that to ensure kinetic stability over a period of one week, the probability of two colliding nanoparticles overcoming the energy barrier and forming an aggregate (i.e., $e^{-V_{max}/k_BT}$) should be less than 1/(8.83 x $10^6$). Using this threshold value, the barrier ($V_{max}$) required to result in kinetic stability over a period of one week, thus is calculated to be ~16/$k_B$T. This threshold value will be used in all subsequent assessments of nanoparticle stability.

Now that a threshold value has been determined, the significance of each of the previously discussed parameter modifications to the xDLVO model is assessed. These results are summarized in Figures 2.4 and 2.5. Of note, Figures 2.4 A/B/C-1 represent traditional methods for employing xDLVO for nanoparticle stability whereas Figures 2.4 A/B/C-2 all show the same result from identical nanoparticles and xDLVO parameterization. First, implications of using surface potential modifications are assessed. Figure 2.4 A shows the modified $V_{total}$ between two gold nanoparticles with a radius of 6.5 nm functionalized with a 1.2 nm thick monolayer that are suspended in a 63 mM ionic strength solution at 25°C. Figures 2.4 A-1 and 2.4 A-2 represent the total interaction

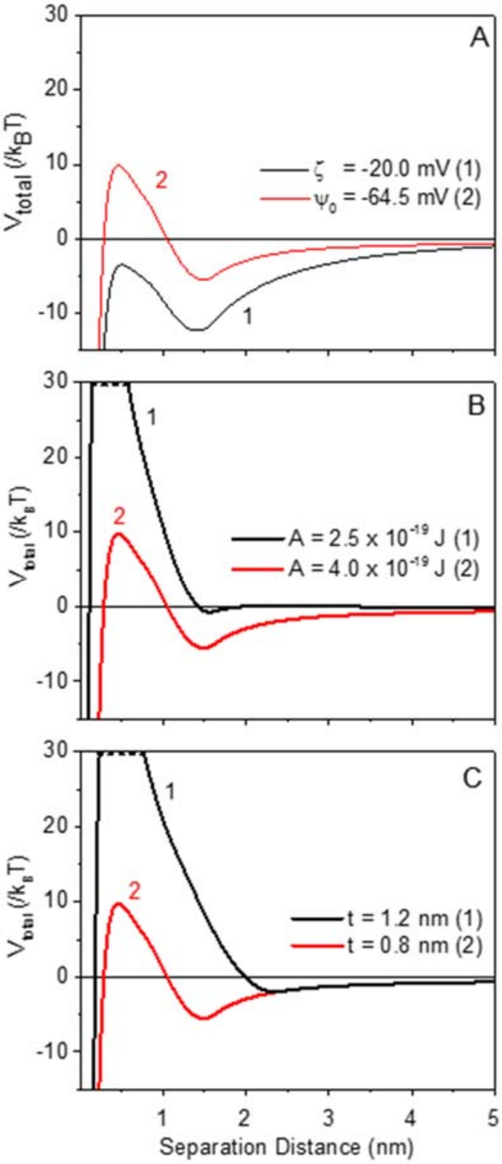

Figure 2.4 Optimized total interaction potential ($V_{total}$) as a function of separation distance (s) between two gold nanoparticles (radius = 6.5 nm, ionic strength = 63 mM, ζ = -20 mV, A = 4 x $10^{-19}$ J, ligand length = 1.2 nm, and monolayer thickness = 0.8 nm) obtained according to the outlined optimized procedure (A1, B1 and C1) (red), and $V_{total}$ obtained using the conventional approximations (A2) $\Psi_0$ = ζ, (B2) A = $A_{Au,Bulk}$ = 2.5 x $10^{-19}$ J, and (C2) t = ligand length, for determining $V_{ele}$, $V_{vdw}$ and $V_{steric}$ (i.e. $V_{osm}$ and $V_{ela}$) respectively (black).

potential when a $\zeta$ = -20 mV and the corresponding $\psi_0$ = -64.5 mV (eq. 2) are used, respectively. Using $\zeta$ as the surface potential significantly undervalues the electrostatic repulsions and leads to a total potential with no repulsive barrier at all. In contrast, the modified parameterization where the surface potential is determined using equation 2 results in a modest potential barrier (~10 mV), which suggests that electrostatic stabilization should provide some thermodynamic stability but not sufficiently to stabilize nanoparticles for one week.

While consideration of surface potentials into the parameterization into the xDLVO model causes the total interaction potential to increase relative to tradition methods, incorporation of a size dependent Hamaker constant for gold nanoparticles results in nanoparticles that are less stable than traditionally predicted. This is demonstrated in Figure 2.4 B. Using the bulk Hamaker constant value reduces the van der Waals attractions to the point that the barrier far exceeds $30/k_BT$, and there is only an insignificant secondary minimum and a repulsive total interaction potential once interparticle separation distances decrease to ~0.4 nm (Figure 2.4 B-1). In contrast, use of the appropriate size dependent Hamaker constant leads to the same overall trend yet a clear secondary minimum and barrier are calculated. This change is an implication of the larger than traditional attractive van der Waals component between the nanostructures which arises from the size dependent dielectric permittivity of the metal nanoparticles as previously discussed.

Similar to the size-dependent Hamaker constant result, the new parameterization for the steric inputs also reduces the overall interaction potential between two gold nanospheres (Figure 2.4 C). In general, as monolayer thickness increases, steric interactions are overestimated as well. As a result, the barrier height in the total interaction potential is again too large (i.e., not physically or experimentally relevant), and there is no secondary minimum. Based on our efforts to parameterize these contributions, it is clear that the short-range height of the repulsive barrier in the total potential will be most sensitive to the SAM thickness. In addition, the tilt angle of a monolayer will determine not only the barrier height but also the separation distance at which this repulsive contribution decays to zero thereby allowing for the possibility of a shallow attractive basin where steric repulsions decay to zero. To demonstrate the effect of accounting for tilt angle on the total interaction potential, Figure 2.5 shows $V_{total}$ for nanoparticles functionalized with the same ligand, with varying tilt angles of 0, 20, 40, and 60°. For tilt angles less than ~40°, no secondary minimum is observed, while the nanoparticles would need to overcome large (>30/$k_BT$) energy barriers for aggregation to occur. In contrast, however, nanoparticles with a tilt angle of 60° show a secondary minimum where the nanoparticles can be transiently trapped before overcoming the barrier that is ~19/$k_BT$. Aggregation, therefore, can be kinetically hindered if the repulsive barrier is of sufficiently large amplitude. Clearly, the predicted behavior of nanoparticles using xDLVO theory, therefore, depends critically on all of these parameterization modifications described here.

## 2.9 Experimentally Testing xDLVO Predictions using Functionalized Gold Nanoparticles

To evaluate the xDLVO theory predictions using the new parameterization methods, we characterize, predict stability, and experimentally assess the stability of engineered gold nanospheres functionalized with SAMs composed of three different ligands including thioctic acid (TA), 6-mercaptohexanoic acid (MHA), and 11-

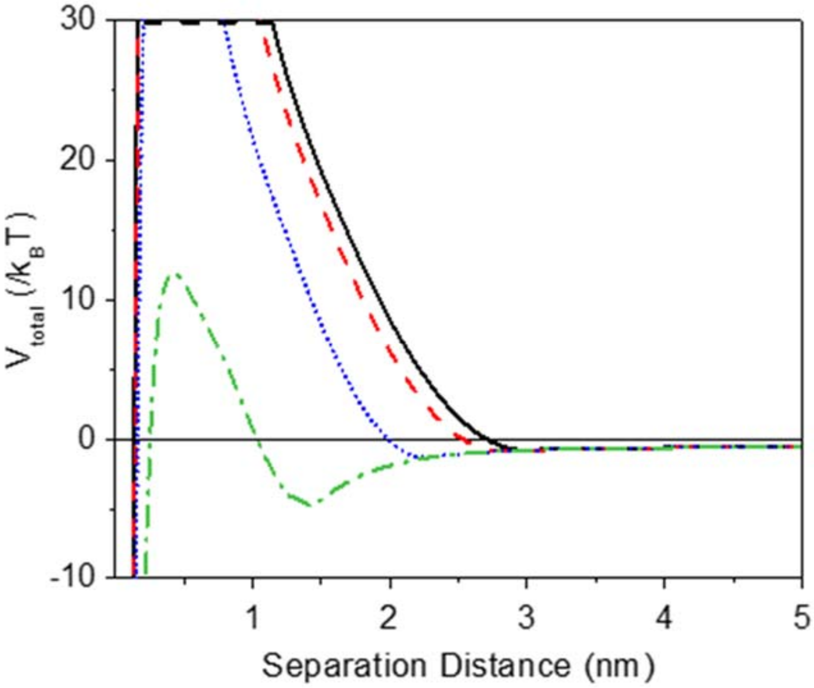

Figure 2.5 Total interaction potentials ($V_{total}$) between a pair of gold nanoparticles (radius = 6.5 nm, Ionic strength = 63 mM, zeta potential = -20.9 mV) functionalized with a ligand of length 1.5 nm, oriented on the surface at a tilt angle of 0° (black solid line), 20° (red dashed line), 40° (blue dotted line), or 60° (green dot-dash line).

mercaptoundecanoic acid (MUA). Nanoparticles are often functionalized with chemi- or physisorbed organic ligands both for targeted applications[17-19,78] and to promote kinetic stability.[79-81] The presence of surface functionalized groups provides steric repulsions, as described above, which can kinetically stabilize the nanoparticles in solution. The series of ligands we chose varies the molecular length of the ligand and the tilt angle in ways that systematically influence monolayer thicknesses.

The total interaction pair potential for gold nanoparticles modified with thioctic acid, 6-mercaptohexanoic acid, and 11-mercaptoundecanoic acid are modeled by summing each interaction pair potential contribution calculated as a function of edge-to-edge separation distance between nanoparticles at 298.15 K ($\varepsilon_r = 78.4$). All calculations were performed using MATLAB (see supplemental information). An ionic strength of 63 mM, corresponding to a Debye length of 1.211 nm, and a Flory Huggins solvency parameter of 0.45 were used for all calculations and calculated in 0.01 nm intervals between separation distances of 0.001 and 10 nm. Equilibrium geometries of the deprotonated ligands in water were obtained by density functional theory (DFT) calculations performed using Spartan '10 V1.1.0. Method B3LYP with a 6-31G* basis set was used for all DFT calculations.

Figure 2.6 shows and Table 2.1 summarizes the experimental characterization of these materials. To monitor and quantify nanoparticle functionalization, extinction spectra for Au nanoparticles incubated in a ligand containing solution are collected. Representative spectra after 5 minutes, 24 hours, and 60 hours are reported in Figure 2.6 (A) - (C) for gold nanospheres functionalized with TA, MHA, and MUA, respectively. For instance, the LSPR wavelength maximum ($\lambda_{max}$) shifts from 518.2 nm before functionalization with TA to 518.7, 519.8, and 520.7 nm, respectively, indicative of the initial increase and eventual

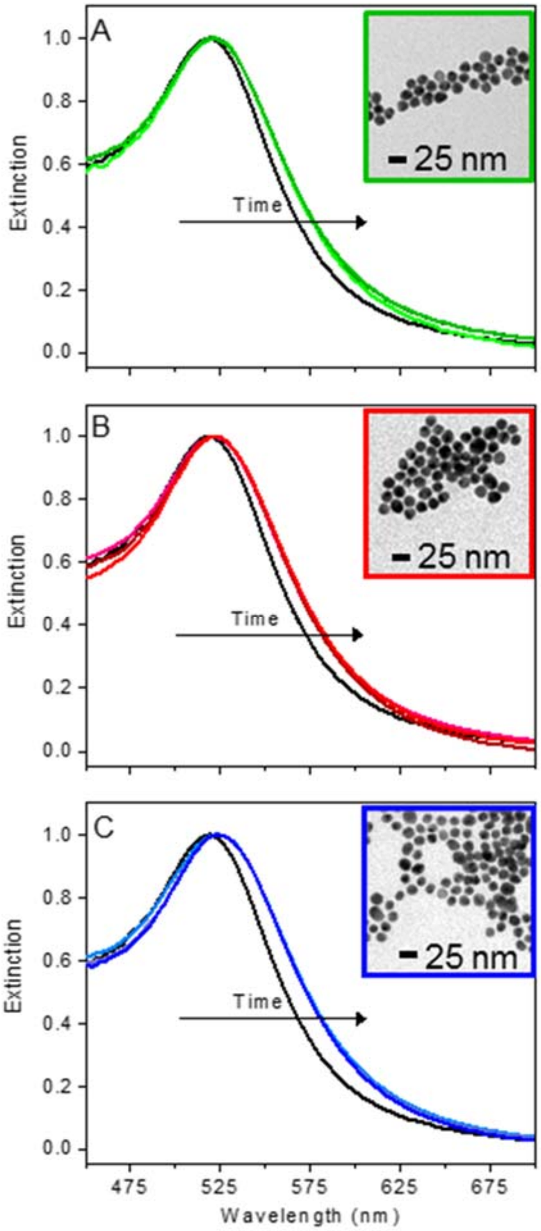

Figure 2.6 Normalized extinction spectra of gold nanoparticles functionalized with (A) TA, (B) MHA, and (C) MUA. Spectra are plotted prior to ligand addition (0 hours), and after incubation for 5 minutes, 24 hours, and 60 hours. All spectra were collected in pH adjusted water (pH adjusted to 11 with 1 M NaOH) (The insets show the TEM images of the functionalized nanoparticles).

Table 2.1 Experimental functionalized nanoparticle parameters at 298.15 K used in the xDLVO calculations

| **Parameter** | **Nanoparticle functionality** | | |
|---|---|---|---|
| | **Au@TA** | **Au@MHA** | **Au@MUA** |
| Nanoparticle diameter (nm) | 12.3 ± 1.2 | 13.0 ± 1.3 | 12.6 ± 1.2 |
| Zeta potential (mV) | -18.4 ± 1.3 | -20.9 ± 1.5 | -37.6 ± 3.5 |
| Molecular weight of ligand (g/mol) | 206.3 | 148.2 | 218.4 |
| Bulk density of ligand (g/cm$^3$) | 1.218 | 1.087 | 0.998 |
| Monolayer thickness (nm) | 0.58 | 0.88 | 1.56 |
| Ligand length* (nm) | 1.06 | 1.13 | 1.77 |
| Tilt angle** (degrees) | 57 | 39 | 28 |
| SAM packing density***<br>($10^{14}$ molecules/cm$^2$) | $2.20_0 \pm 0.03_9$ | $4.58_1 \pm 0.01_9$ | $4.97_5 \pm 0.01_8$ |

Values are estimated using DFT*, LSPR**, and XPS*** results, respectively.[1]

saturation of ligand packing and assembly on the metal surface. Qualitatively similar trends are observed for all three ligands (Figure 2.6 A-C), but the saturated $\lambda_{max}$ values for each ligand differ reflecting the differences in the monolayer thicknesses. Determination of the monolayer thickness and tilt angles requires several parameters in addition to the LSPR $\lambda_{max}$, such as the refractive index sensitivity of the nanoparticles, m, the electromagnetic field decay length, and the refractive index of the ligands (see equations 2.9 and 2.10). Previous studies showed that the refractive index sensitivity of citrate stabilized Au nanoparticles (d ~13 nm) is ~45 nm per refractive index unit,[121] the characteristic electromagnetic field decay length is 5.7 nm,[122-125] and the refractive index of alkanethiols in a SAM is 1.65.[116] Using these values and equations 2.9 and 2.10, the monolayer thicknesses are 0.58, 0.88, and 1.56 nm for TA, MHA, and MUA functionalized nanoparticles, respectively.

To validate these results, we calculate the ligand tilt angles corresponding for these SAMs to compare with previous studies using SAMs using the ligand length, including the length of the Au-S bond, and equation 2.11. Previous experimental and theoretical evidence showed that the Au-S bond distance for alkanethiol SAMs on gold nanoparticles is ~0.24 nm.[82,126-128] To determine the ligand length (l), i.e., not including tilt angle, this Au-S bond length is added to the distance from the S to the furthest O atom in each alkanethiol calculated using energy minimized molecular geometries from DFT calculations. The insets in Figure 2.7 (A) show the energy minimized molecular structures. For MHA and MUA, the calculated molecular lengths are easily determined ($l_{MUA}$ = 1.77 nm and $l_{MHA}$ = 1.13 nm). TA, however, binds to gold via two S atoms,[129-131] thus the distance from the S atom nearest to the alkyl chain to the furthest O atom, is added to the S-Au bond length to

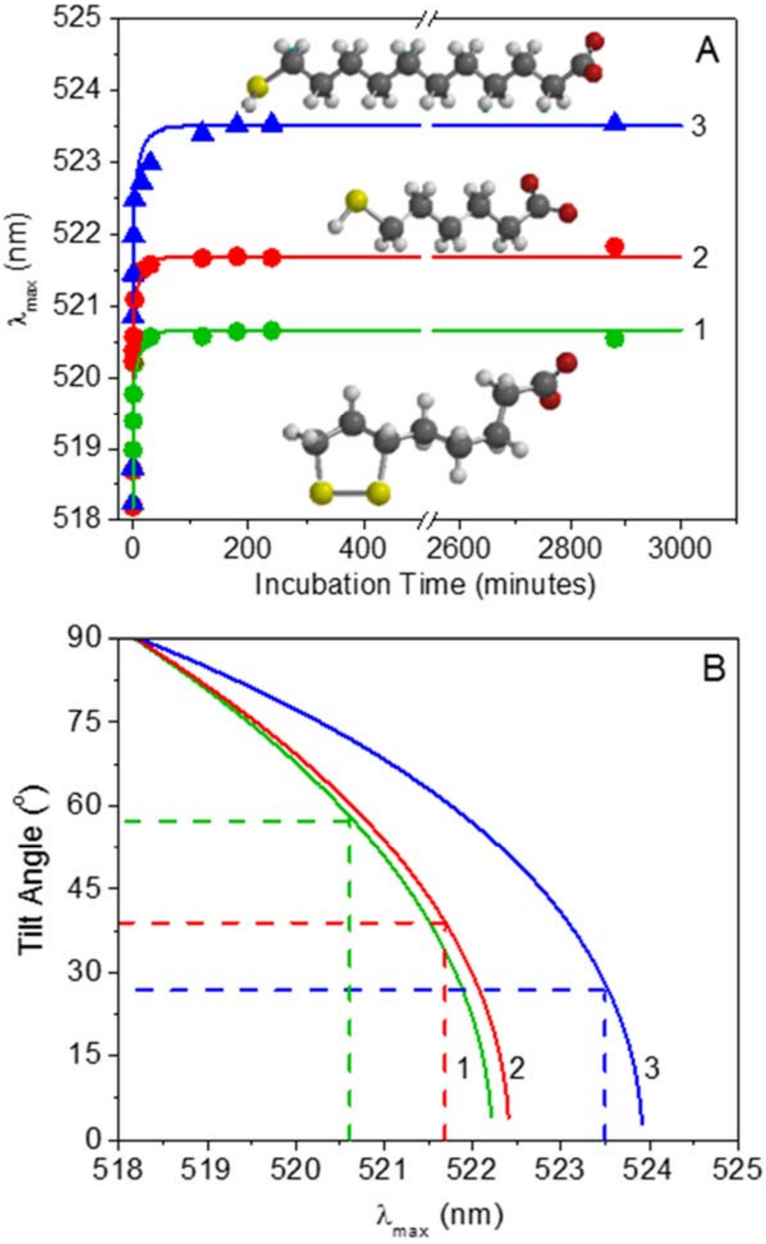

Figure 2.7 (A) LSPR $\lambda_{max}$ response for Au nanoparticles as a function of incubation time, and (B) variation of SAM tilt angle ($\theta$) as a function of $\lambda_{max}$ for (1) TA, (2) MHA, and (3) MUA functionalization. DFT optimized molecular geometries of deprotonated ligands are shown as insets in panel A (C - grey, H - white, O - red and S - yellow). The $\lambda_{max}$ at saturation surface coverage was used to determine the corresponding $\theta$ (dotted lines).

determine the ligand length ($l_{TA}$ = 1.06 nm). Figure 2.7 (B) illustrates the determination of the tilt angles for each ligand based on the saturated $\lambda_{max}$ values are using plots of equation 2.11. The tilt angles for the three ligands are 57º, 39º, and 28º for TA, MHA, and MUA, respectively, and are consistent with previously reported tilt angles for alkanethiol SAMs on gold nanoparticles.[132-134]

Now that these materials are thoroughly characterized, their stability can be predicted using the previously discussed xDLVO parameterization inputs. These results are summarized in Figure 2.8, which shows the total interaction pair potentials for all three functionalized nanoparticles. The implications of our new parameterization for xDLVO theory are most apparent in the total interaction potential for MHA functionalized (Au@MHA) nanoparticles, where the potential barrier exhibits a height of ~25/$k_BT$ and there is a shallow secondary minimum at an edge-to-edge separation of about 1.7 nm. In contrast, for TA (Au@TA) and MUA (Au@MUA) functionalized particles the modeling predicts either no repulsive potential (TA) or a barrier of >50/$k_BT$ (MUA). The prediction of a secondary minimum for MHA functionalized particles indicates a tendency to form reversible, metastable agglomerates with an interparticle spacing corresponding to the location of the secondary minimum in the pair potential. For MUA functionalized nanoparticles, however, the potential indicates a propensity to behave as stable primary nanoparticles, while the model predicts that TA functionalized nanoparticles should aggregate.

Because gold exhibits well-established, size-dependent optoelectric properties,[135] these predictions can easily be tested. Specifically, when the nanosphere diameter decreases below the mean free path of the metal (~25 nm for gold[136,137]), the scattering

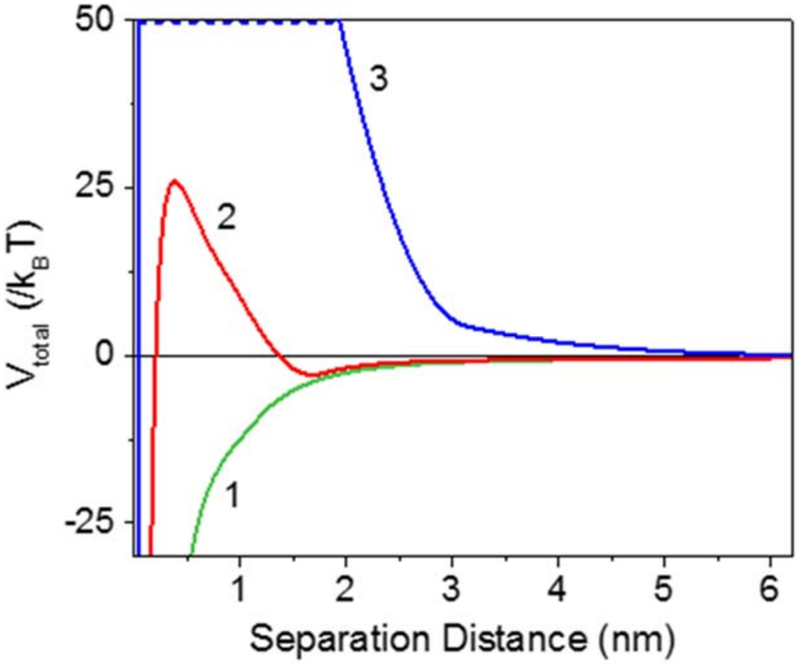

Figure 2.8 The total interaction pair potentials between two (1) Au@TA, (2) Au@MHA, and (3) Au@MUA nanoparticles as predicted using xDLVO theory.

frequency of the excited electrons increases thereby decreasing the electrical conductivity. The nanoparticle cores used here (*d* ~13 nm) are, therefore, not expected to conduct if the inter-particle separation distance is sufficiently large such that primary particle-like behavior dominates. If aggregation occurs, however, the size of the gold aggregates that form will exceed the mean free path of the electrons, and the aggregates will conduct electricity. In the intermediate case, where the nanoparticles form metastable, reversible agglomerates, the nanoparticles will be separated from one another but at a length scale where electrons can still hop from one particle to the next. Thus, agglomerates should conduct but with a conductivity that is less than that of aggregated particles.

To experimentally evaluate the electrical behavior of covalently functionalized gold nanoparticles at steady state and test the xDLVO predictions, solution-phase nanoparticles are suspended in buffer and placed in a 332 V/cm electric field to increase the collision frequency between nanoparticles. The measurements are performed by filling a capillary with buffer containing gold nanoparticles at 0, 1, or 5 nM concentrations, applying the electric field, and recording current changes (stabilized within 1 minute).

Figure 2.9 (A) and (B) shows the changes in the currents measured in the presence of the three functionalized nanoparticles at 1 nM and 5 nM concentrations, respectively. These results are consistent with the xDLVO predictions. For example, increasing the concentration of TA functionalized nanoparticles should lead to more and/or larger aggregates that would increase the conductivity, which is precisely what we observe. MHA functionalized nanoparticles, which are predicted to form metastable agglomerates with edge-to-edge separation distances of ~1.7 nm, also show an increase in conductivity but to a lesser extent than observed for TA functionalized nanoparticles. Again, although the gold

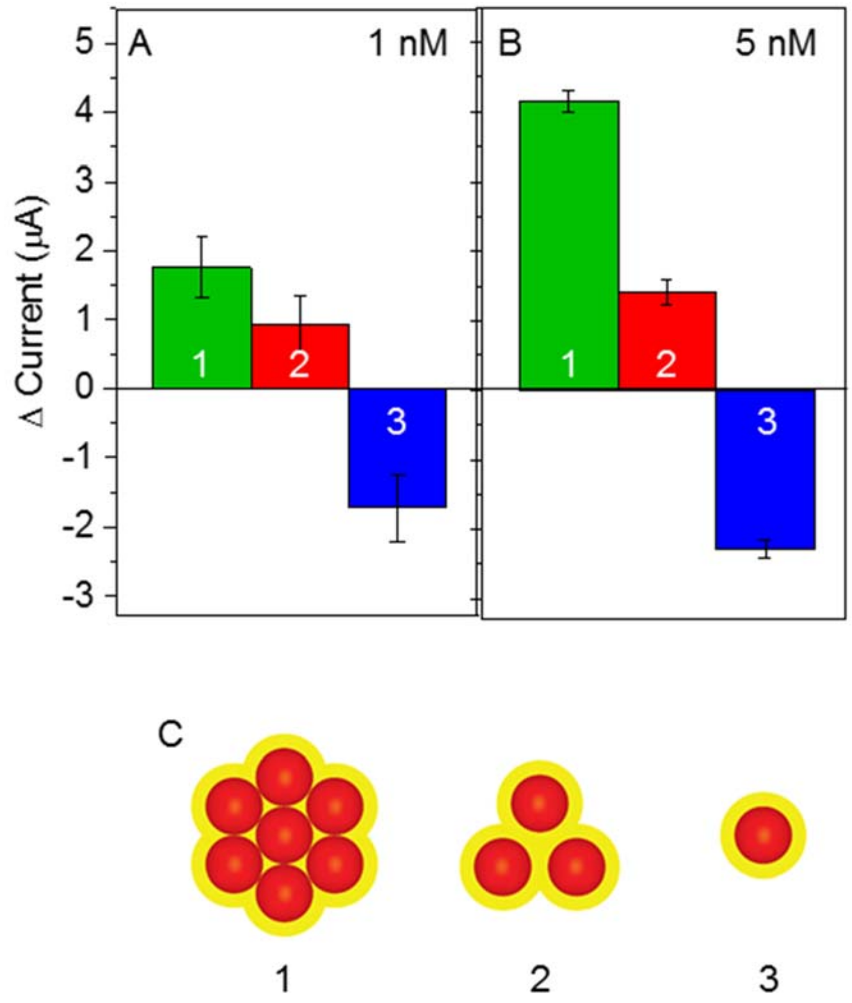

Figure 2.9 Current differences measured in the presence of (A) 1 nM and (B) 5 nM concentrations of (1) Au@TA, (2) Au@MHA, and (3) Au@MUA nanoparticles placed in a 332 V/cm electric field (Current measured in the absence of nanoparticles was used as reference measurements. Error bars represent the standard deviation of at least 5 measurements). (D) Cartoon representations of the stability predicted for (1) Au@TA, (2) Au@MHA, and (3) Au@MUA nanoparticles, where the nanoparticles aggregate, agglomerate, or are stably suspended respectively. Note that here the thickness of the nanoparticle monolayers are indicated (in yellow) around the spherical nanoparticles.

cores are not in physical contact at this separation distance, electron hopping between the nanoparticles will occur leading to conductive agglomerates but with a much lower conductivity than for aggregates. This experimental result is consistent with the predictions in Figure 2.8. Finally, xDLVO predictions suggest that MUA functionalized nanoparticles will remain well-dispersed in solution given the large potential barrier between nanoparticles. Consequently, these particles should not be effective conductors consistent with the experimental observations. Thus, the experimental conductivity measurements on these three functionalized nanoparticle systems are entirely consistent with the predictions of the xDLVO model using the proposed parameterizations. This result is significant because the detailed shape of the total interaction potential is extremely sensitive to the interplay between the individual interaction potentials, which are, in turn, sensitive to the parameter. If this parameterization were not sufficiently accurate with respect to any of these contributions, then the predictions using xDLVO theory to capture the experimental behavior would be extremely difficult. This experimental measurement, therefore, provides validation and strong support for the approach adopted herein.

## 2.10 Summary, Conclusions and Future Direction

In summary, the stability of functionalized ~13 nm diameter gold nanospheres was predicted using a reparameterization of xDLVO theory and confirmed using conductivity experiments. Three contributions to the xDLVO model were considered. First, electrostatic interactions between two spherical gold nanoparticles were modeled using surface potentials rather than directly using experimentally measured zeta potentials so that this contribution was not underestimated. Second, the size dependence of the Hamaker constant for gold was incorporated into the van der Waals potential so that the attractive interactions between nanospheres were not underestimated. Third, the monolayer thickness was determined empirically, which accounts for both the ligand length and the SAM tilt angle to calculate both osmotic and steric interaction potentials. These modifications are summarized in Figure 2.10 and were eventually used in predicting the stability and the ensuing electrical properties of three types of carboxylic acid (TA, MHA, and MUA) functionalized spherical gold nanoparticles. The experimental results of conductivity measurements on gold nanoparticles functionalized by TA, MHA, and MUA provided strong support for the predictions of xDLVO theory using these new approaches for determining the parameters that are used in this model.

In conclusion, implications of surface chemistry variations on metal nanoparticles (i.e., packing density, tilt angle, and composition etc.) influence not only the plasmonic and electrical properties of these materials but also their behavior in subsequent applications. The combination of theoretical predictions with straightforward experimental measurements supports and justifies the observed electrical behavior of the functionalized gold nanoparticles used herein. Such molecular level insight into surface chemistry directed nanostructure-property relationships are envisioned to improve the systematic use of solution-phase nanomaterials by providing a method for predicting the thermodynamic stability of nanomaterials. Hence, future direction of these improved xDLVO theory parametrizations include predictions of the solution-phase nanoparticle behavior and stability of various other morphological forms, and/or functionality thereby facilitating the rational design of and solvent selection for functionalized nanomaterials in various novel nanotechnology applications.

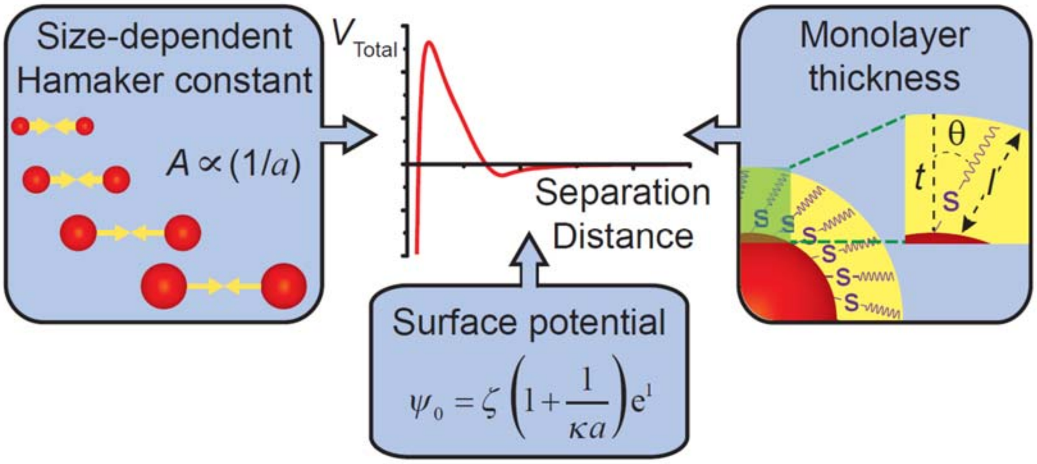

Figure 2.10 Summary of modifications conducted on the xDLVO theory. First, electrostatic Interactions between two spherical gold nanoparticles were modelled using surface potentials rather than directly using experimentally measured zeta potentials. Second, the size dependence of the Hamaker constant for gold was incorporated into the van der Waals potential. Third, the monolayer thickness was determined empirically, which accounts for both the ligand length and the SAM tilt angle to calculate both osmotic and steric interaction potentials.

# CHAPTER 3

# SOLUTION PHASE SURFACE ENHANCED INFRARED ABSORPTION VIA VIBRATIONAL CHROMOPHORES ANCHORED ON SPHERICAL GOLD NANOPARTICLES

## 3.1 Surface Enhanced Two-dimensional Infrared (SE-2D IR) Spectroscopy

Surface enhanced vibrational spectroscopies including surface enhanced Raman scattering (SERS), surface enhanced infrared absorption (SEIRA), and surface enhanced two-dimensional infrared (SE-2D IR) spectroscopy can provide rapid, sensitive, and selective detection of target molecules in air and liquid samples. Table 3.1 summarizes the characteristics of these methods. Notably, little is known about the enhancement mechanisms or the optimum conditions for SE-2D IR. Although initial experiments are promising,[27] systematic studies have yet to be performed. In contrast, SERS and SEIRA are more widely characterized. Hence, the objective of this study is to develop a model system for solution phase SEIRA, with the potential of being used in observing a SE-2D IR signal.

All of these techniques depend on the optical properties of nanostructured substrates (i.e., composition, shape, size, surface chemistry, stability, and dielectric environment).[28,138-140] These factors will affect the sensitivity of the detection methods. Even for SERS, improved sensitivity will offer additional benefits when samples from polluted environments are processed or for analytes with weak vibrational cross-sections. For 2D IR, signal enhancements are vital to make this technique analytically viable. A

Table 3.1 Characteristic features of SERS, SEIRA, and SE-2D IR spectroscopy

| Parameter | Spectroscopic Technique | | |
|---|---|---|---|
| | **SERS** | **SEIRA** | **SE-2D IR** |
| Excitation | Tunable, Narrow | Broad | Tunable, Broad and narrow |
| Electric field intensity dependence | $E^4$ | $E^2$ | $E^4$ |
| Enhancement mechanism | Chemical, Electromagnetic | Debated (Chemical, Electromagnetic, Image charge…) | Unknown (Complementary to SEIRA?) |
| Enhancement factor | Up to $10^9$ | Up to $10^4$ | Up to $10^9$ |
| Sensitivity | Excellent | Modest | Unknown |
| Selectivity | Poor | Poor | Excellent |
| Ideal NP-NP spacing | < 2 nm | $\frac{(\text{size} + \text{spacing})}{\text{spacing}}$ | Unknown |
| Water tolerance | Excellent | Poor | Poor |

common way to increase the enhancement factor is to design plasmonic nanostructures that generate “hot-spots” in crevices, voids, or gaps.[141]

For example, nanoparticle arrays provide such hot-spots[142] and offer control over inter-particle spacing. If the spacing between nanoparticles decrease, signals will increase due to heightened electromagnetic fields between nanoparticles.[143,144] Thus, methods to assemble two-dimensional arrays with controlled spacing could revolutionize how substrates are formed and employed. Recently, nanoplasmonic SERS substrates were developed using on the self-assembly of nanoparticles at liquid | liquid and liquid | air interfaces.[145,146] These structures have been found to promote large electromagnetic fields between nanoparticles and provide a tool to increase the sensitivity of surface-enhanced spectroscopies.

## 3.2 Synthesis and Characterization of Spherical Gold Nanoparticles

Gold(III) chloride trihydrate ($HAuCl_4 \cdot 3H_2O$), trisodium citrate ($C_6H_5Na_3O_7 \cdot 2H_2O$), and hydroxylamine hydrochloride ($NH_2OH \cdot HCl$) were purchased from Sigma (St. Louis, MO). Water (18.2 MΩ $cm^{-1}$) was obtained using a Nanopure System from Barnstead (Dubuque, IA), and used in the preparation of all solutions. All glassware was cleaned with aqua regia (3:1 $HCl:HNO_3$), rinsed thoroughly with water, and oven-dried overnight before use. Seed gold nanoparticles were synthesized via a well-established citrate reduction process.[147,148] Briefly, a 1 mM $HAuCl_4 \cdot 3H_2O$ solution (100 mL) was refluxed and vigorously stirred for 15 minutes. Once a rolling boil was achieved, 10 mL of a 39 mM citrate ($C_6H_5Na_3O_7 \cdot 2H_2O$) solution was added quickly. The resulting solution was refluxed for an additional 10 minutes and was allowed to equilibrate to room temperature while stirring. The resulting average seed gold nanoparticle diameter is typically about 13 nm as determined from transmission electron microscopy.[148]

Synthesis of 1st generation gold nanoparticles were conducted using freshly prepared seed gold nanoparticles as the precursors as described previously elsewhere.[149,150] Briefly, 37.50 mL of seed gold nanoparticles were diluted with 337.50 mL of Nanopure water. Then, 3.13 mL of freshly prepared 0.2 M hydroxylamine hydrochloride ($NH_2OH{\cdot}HCl$) and 25.9 μL of 2 M citrate was added into the flask, while stirring was continued for 5 minutes. Finally, 3.75 mL of 1% w/v $HAuCl_4{\cdot}3H_2O$ (i.e. 0.04 g in 4 mL Nanopure water) was added and the contents were allowed to stir for 4 hours. The flask was covered with Aluminum foil during synthesis as gold nanoparticles as well as the gold salt is light sensitive.

The stability of the as-synthesized seed and first generation particles were examined using their localized surface plasmon resonance (LSPR) behavior as indicated in Figure 3.1. All extinction measurements were conducted using a UV-visible spectrophotometer (Ocean Optics HR4000, Dunedin, FL) configured in transmission geometry. To estimate the size as well as to observe the morphology of these nanoparticles, the seed and 1st generation gold nanoparticles were imaged using a JEOL JEM-1230 electron microscope as shown in the insets in Figure 3.1. In all cases, 2 μL of a diluted nanoparticle solution was applied to a carbon-formvar coated copper grid (400 mesh, Ted Pella or Electron Microscopy Sciences) and allowed to air dry. The resulting images were analyzed using Image Pro Analyzer, and at least 100 nanoparticles were evaluated per sample. According to the TEM analysis, the diameter of the seed and 1st generation particles were estimated to be 12.4 ± 1.2 and 20.4 ± 2.0 nm respectively. The previously observed LSPR was then

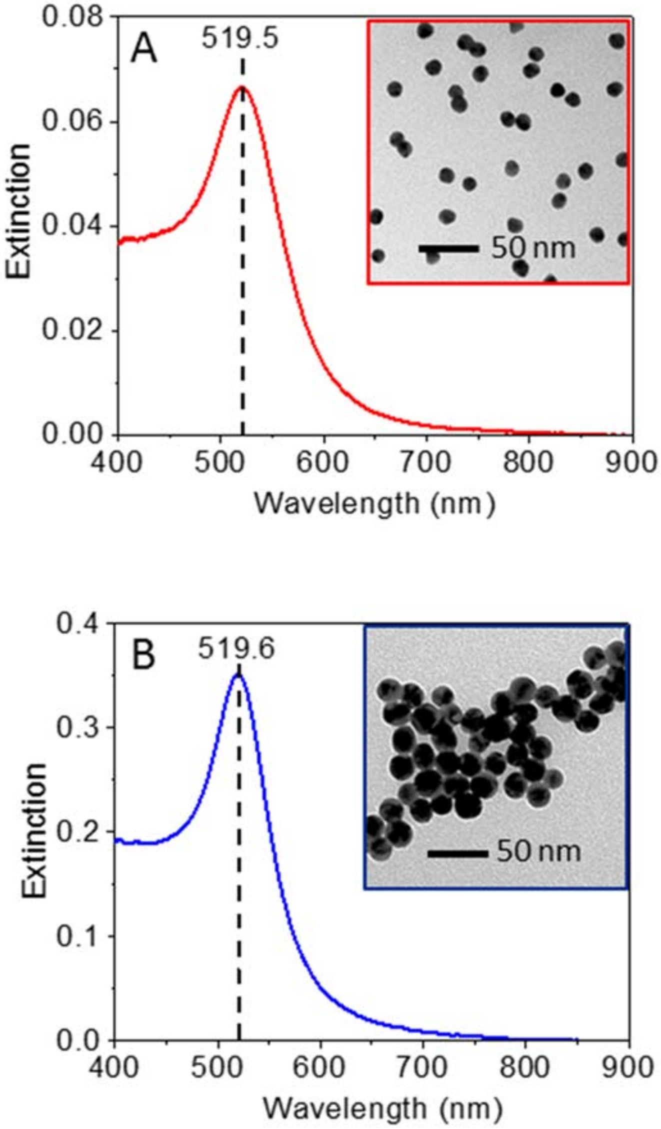

Figure 3.1 LSPR of the synthesized (A) seed and (B) 1st generation gold nanoparticles. The insets in each panel show the TEM image of the gold nanoparticles, from which the diameter of the seed and 1st generation particles were estimated to be 12.4 ± 1.2 and 20.4 ± 2.0 nm, respectively.

used to estimate the diameter, concentration, and the extinction coefficient of the as-synthesized gold nanoparticles as described elsewhere.[151] The estimated extinction coefficients ($\varepsilon$) at the extinction maximum wavelength ($\lambda_{max}$) according to these diameters were 2.0 x $10^8$ and 5.8 x $10^8$ respectively for seed and 1st generation gold nanoparticles.

## 3.3 Synthesis and Characterization of the Potential Chromophore, *p*-Azidothiophenol

In order to observe a SEIRA signal, a chromophore that has a large IR cross section would have to associate with a gold substrate. Thiols (-SH) are well known to form ordered monolayers on gold nanoparticles,[130,152,153] while the azide group ($N_3^-$) is used as a probe in many IR analyses.[154,155] Further, conjugation between the thiol group and terminal azide in the selected chromophore molecule would allow optimum electromagnetic coupling between the nanoparticle and the terminal chromophore thus increasing the chance of observing an enhanced IR signal. Thus, *p*-azidothiophenol was synthesized as a potential chromophore for initial SEIRA investigations. Previously, evidence suggested that this compound was SERS active,[156] indicating the possibility of electromagnetic coupling between the compound and plasmonic substrate.

*p*-azidothiophenol was synthesized using guidance from literature. According to Kwok et.al. azidobenzene can be synthesized from aniline in the presence of catalytic tetraalkylammonium hydroxide.[157] Further, according to Butini et. al. aniline can undergo diazotization, followed by nucleophilic substitution in the presence of thiol (-SH) groups on the phenyl ring.[158] Here, *p*-aminothiophenol (12.5 g, 0.1 mol) and distilled water (50 mL) were mixed in a 250 mL round bottom flask. Then, concentrated HCl (17.4 mL) was added, and the contents were vigorously stirred in an ice bath (Caution - All steps discussed here were conducted in a well ventilated hood and behind a blast shield). After cooling to 0 °C and stirring for 20 - 30 minutes, a freshly prepared, ice cold solution of $NaNO_2$ (7.16g, 0.1 mol) in water (20 - 30 mL) was added dropwise, while maintaining the reaction temperature between 0 - 5 °C.

The reaction mixture was stirred for an additional 10 minutes and a freshly prepared solution of sodium azide (6.75 g, 0.1 mol) in water (30 - 40 mL) was added dropwise via an addition funnel, while maintaining the reaction temperature below 5 °C. The mixture was then stirred for an additional 20 - 30 minutes at 0 °C, followed by stirring at room temperature for 3 hours. Finally, the product was extracted with ethyl acetate (2 x 100 mL) and the solvent was evaporated by rotary evaporation. The resulting product (a thick, yellow colored oil) was refrigerated at 4 °C until further analysis was conducted.

The product was first characterized using $^1$H-NMR spectroscopy, where the desired para substitution was clear from the characteristic peak pattern (doublet of doublets) (Appendix C). However, the absence of a thiol proton peak indicated the possibility for the synthesis product to be oxidized as a consequence of the conditions used during synthesis. This was further evidenced by the peak at 300 m/z observed on the mass spectrum of the product, indicating the presence of bis(*p*-azidothiophenol) disulfide as the synthesis product, instead of the desired product *p*-azidothiophenol (Appendix C). However, sulfur has an extremely high affinity to gold (47 kcal/mol), and the disulfide bonds can be broken in the presence of a gold surface or gold nanoparticles thus allowing the strong S-Au linkage to be established. This has been previously observed with many studies concerned with the formation of self-assembled monolayers (SAMs) on gold surfaces.[159,160]

Finally, the presence of the azide substitution was confirmed via IR absorption where a doublet of peaks (at 2094 $cm^{-1}$ and 2130 $cm^{-1}$), split by Fermi resonance was observed due to the asymmetric stretching of the azide group as seen in Figure 3.2 (A). These frequencies as well as the observance of a Fermi resonance are consistent with previous studies conducted with various azides.[161,162] Typically, azides are known to have high IR absorptivity. However, in order to use the synthesized product in SEIRA investigations, accurate values of the molar absorption coefficients are needed. Thus, a calibration was conducted by preparing a series of concentrations ranging from 50 - 400 mM of *p*-azidothiophenol (i.e., concentrations ranging from 25 - 200 mM of the disulfide compound). Because the synthesized product is only sparingly soluble in water, dimethyl formamide (DMF) was used as the solvent in preparing the calibration standards. The calibration curves obtained using spectra collected at a 25 μm pathlength (fixed pathlength cell) are shown in Figure 3.2 (B) and (C) for 2130 and 2094 $cm^{-1}$ respectively, from which the molar absorption coefficients were determined to be 708 and 484 $M^{-1}$ $cm^{-1}$ at 2130 and 2094 $cm^{-1}$ respectively.

## 3.4 Enhancement Experiments with *p*-Azidothiophenol

Now that the desired nanoparticles and the chromophore molecules are synthesized, the chromophore molecules are bound to the nanoparticle surface via the cleavage of the disulfide bond as observed in previous studies.[159,160] Figure 3.3 (A) shows the LSPR spectra of the 1st generation gold nanoparticles with and without 2.5 μM *p*-azidothiophenol in an aqueous solution containing 16 mM DMF. Here, DMF was required to solubilize the analyte as well as to control molecular orientation (*vide infra*), while the stability of the

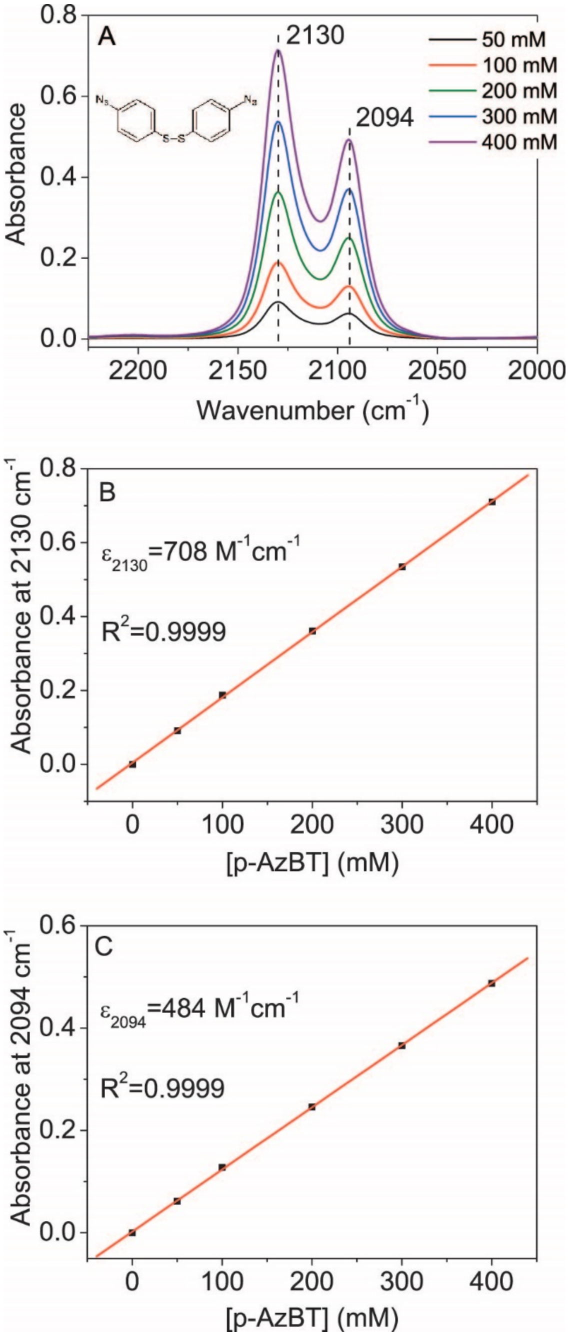

Figure 3.2 (A) IR spectra, and the calibrations conducted to determine the molar absorption coefficients of *p*-azidothiophenol at (B) 2130, and (C) 2094 cm$^{-1}$. The structure of the synthesis product bis(*p*-thiophenol) disulfide is shown alongside the spectra in panel (A).

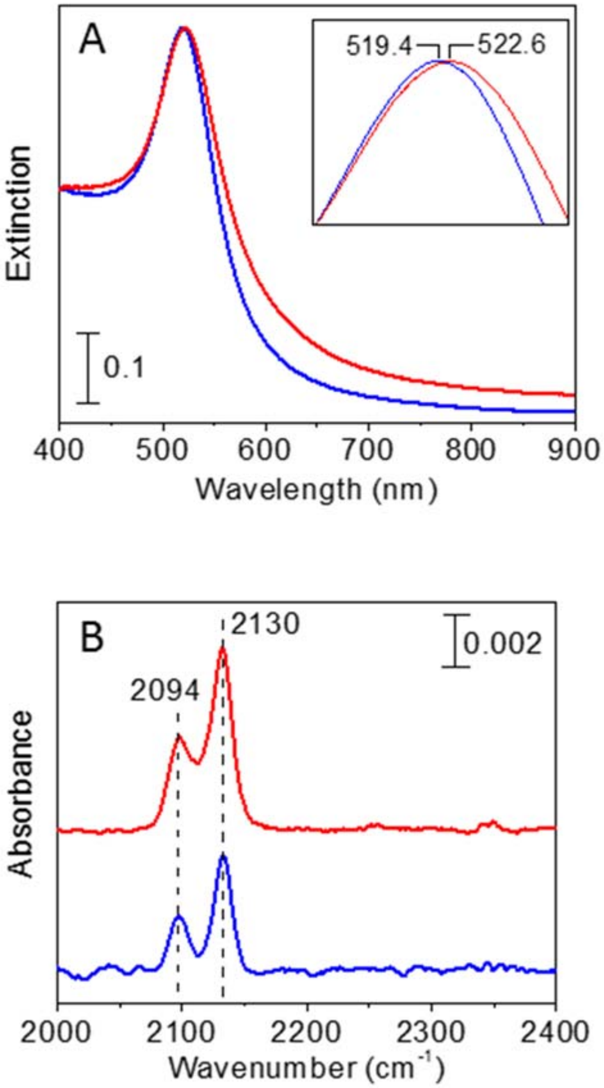

Figure 3.3 Characterization of synthesized *p*-azidothiophenol, with (A) LSPR, (B) IR spectroscopy. The LSPR spectra of 1st generation gold nanoparticles is shown in (A), in the absence (blue) and presence (red) of the synthesized product. As can be seen clearly from the inset, binding of the molecule is evidenced by the shift in $\lambda_{max}$ from 519.4 to 522.6 nm. The IR spectra in (B) were obtained for solutions containing 2 mM *p*-azidothiophenol in 1:1 DMF:$H_2O$, in the presence (red) and absence (blue) of nanoparticles.

nanoparticles in DMF containing media were previously studied in a series of separate solvent exchange experiments (Note that the water solubility of *p*-azidothiophenol was previously determined to be only ~20 μM from a saturated aqueous solution, with the help of ultraviolet absorbance values (data not shown)). As can be seen here, the LSPR indicates a shift of +3.2 nm in the presence of the analyte. Such variations in the $\lambda_{max}$ have been previously observed during surface functionalization while it being attributed to the changes in local refractive index of the nanoparticles caused by the presence of the surface functional groups.[119,163] Thus, we confirm that the synthesized analyte bis(*p*-azidothiophenol) disulfide successfully binds to the gold nanoparticles via the cleavage of the disulfide bond.

The other important feature of the analyte is the ability of the analyte to couple with the electromagnetic field at the nanoparticle surface, thus giving rise to enhanced absorption and/or scattering properties. To confirm this, the SERS spectrum of the above nanoparticle solution was obtained as shown in Figure 3.4 (B). The SERS measurements were conducted using an Advantage 200A Raman spectrophotometer (DeltaNu) using a 633 nm excitation wavelength. Here, the symmetric stretch of the azide group was observed at 1299 cm$^{-1}$ (7 cm$^{-1}$ shift compared to the Raman spectrum) in the sample containing nanoparticle bound *p*-azidothiophenol, whereas no Raman features were observed in the absence of nanoparticles. The other scattering features observed here at 1579, 1180, 1076, and 369 cm$^{-1}$ can be attributed to C-C stretching/C-H bending, C-H bending, C-C stretching/C-S stretching, and C-S bending motions respectively, while the remaining features could be attributed to C-C and C-H bending and stretching motions.[156] Importantly, this confirmed that the synthesized chromophore was SERS active and is

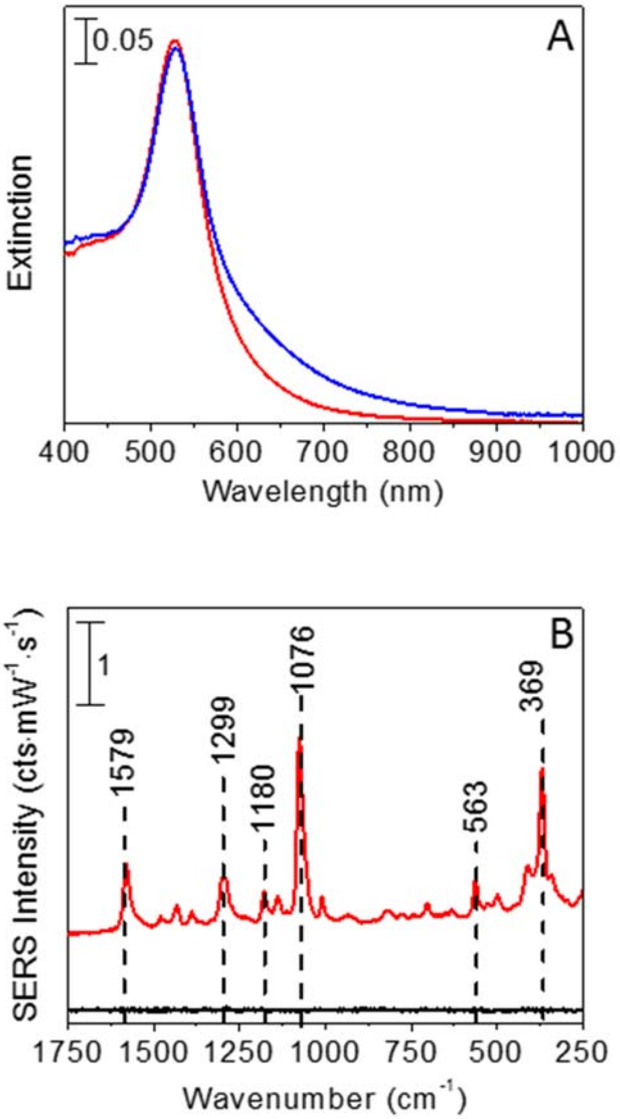

Figure 3.4 Stability of nanoparticles in the presence of DMF was investigated using LSPR spectra as indicated in (A). A slight broadening was clearly visible for the sample suspended in a 1:1 DMF:$H_2O$ mixture (blue), compared to those suspended in $H_2O$ only. Interestingly, the presence of DMF was favorable for SERS activity, where as seen in (B) significant SERS activity was observed for 2.5 µM *p*-azidothiophenol in 16 mM DMF (red), while no SERS activity was visible with the same analyte concentration, in the absence of nanoparticles (black).

therefore capable of coupling with the electromagnetic field at the nanoparticle surface once bound onto the nanoparticle.

Collectively, the above evidence suggests that the gold nanosphere bound *p*-azidothiophenol is a suitable system to be used in preliminary investigations of a possible SEIRA signal; therefore, IR spectra were collected with a 25 μm pathlength using a Bruker Tensor 27 IR spectrophotometer for solutions containing a 2 mM *p*-azidothiophenol in 1:1 DMF:$H_2O$ as indicated in Figure 3.3 (B). However, the azide absorption could be observed both in the presence as well as absence of the nanoparticles, with no significant change in absorption intensity being indicated for nanoparticle bound *p*-azidothiophenol.

We hypothesize that the non-observation of an enhanced IR signal was mainly due to the low nanoparticle concentration used here. Under these low concentrations only a very small portion of the analyte molecules are bound to the nanoparticles, limited by the surface site capacity. Thus, an observable enhancement is not resulted. However, *p*-azidothiophenol suffers from low solubility in aqueous media, hence requiring the presence of a non-polar substance in the medium (e.g. DMF) to promote solubility. The stability of gold nanoparticles in mixed solvent systems, nevertheless, is less-known. Therefore, the solubility of *p*-azidothiophenol in aqueous media limits its applicability in SEIRA based experiments.

To be more precise, the concentration of *p*-azidothiophenol used here was 2 mM, and the absorbance that is expected with a 25 μm pathlength is therefore ~0.0035 OD at 2130 $cm^{-1}$, according to the molar absorption coefficient determined previously. This in turn is a significantly low absorption, especially in the presence of water which strongly absorbs in the most part of the mid IR spectrum. Assuming that only 20% of the analyte molecules here are bound onto the nanoparticles, even if 100x enhancement was achieved, the enhanced signal would still only be ~0.07 OD, which is insignificant, especially compared to the large water background. Although we do observe a very small signal increase (in the order of 0.002 OD) in the presence of nanoparticles, variations of this magnitude can easily be caused by fluctuations in pathlength or background subtraction differences. Thus, the observed result is attributed to the low nanoparticle concentration used versus the analyte concentration in the experiment above.

Further, it should be noted that the solvent was exchanged into 1:1 DMF:$H_2O$ in order to achieve a 2 mM analyte concentration. Typically, nanoparticles are suspended in water ($\varepsilon = 78.4$ at 25° C), and stabilized by part because of the solvent dielectric properties. To date, little is understood about the stability of nanoparticles in alternative or mixed solvents, although many combinations have been demonstrated to yield stable nanoparticles. In order to understand any stability changes that may occur for these 1st generation spherical gold nanoparticles, 0.4 nM samples of these nanoparticles were suspended into a 1:1 DMF:$H_2O$ medium while the ionic strength of the medium was maintained constant. The LSPR spectra of these nanoparticles are indicated in Figure 3.4 (A), while the nanoparticles suspended in a purely aqueous medium at the same concentration is indicated for comparison.

As can be seen, the presence of DMF broadens the LSPR peak of the nanoparticles (This effect was more pronounced for higher nanoparticle concentrations). Such broadening is typically characteristic of plasmon dampening.[164] Hence, it is clear that the presence of DMF, especially at high concentration as used above causes the optical properties of the nanoparticles to be altered. Therefore, the observed IR absorbance results are a consequence of the high DMF content in the sample. However, a pure $H_2O$ medium could not be used because of the previously discussed solubility limitations of *p*-azidothiophenol. Thus, the solubility of *p*-azidothiophenol and the stability of nanoparticles in non-aqueous media have to be further investigated in order to use *p*-azidothiophenol in SEIRA investigations.

Interestingly, the presence of DMF was favorable in the SERS experiments. Recall that the samples used in the SERS experiments contained 16 mM DMF. It was observed that the nanoparticle sample containing 2.5 µM *p*-azidothiophenol and 16 mM DMF indicated significant SERS activity, whereas no such activity was observed in the absence of DMF as shown in Figure 3.4 (B). The presence of DMF modifies the native dielectric properties at the vicinity of the nanoparticle surface. This may cause the molecule to adopt alternate orientations at the surface in order to maximize stability in solution. As widely accepted, orientation plays a key role in SERS and SEIRA, and only those vibrations having surface-normal polarizability components will be Raman active.[165,166] Thus, we attribute the variations observed in SERS activity to possible, more vertical molecular orientation with relative to the surface in the presence of DMF as illustrated in Figure 3.5. Collectively, low nanoparticle concentration, nanoparticle stability, and the unknown orientations of the analyte at the nanoparticle surface in 1:1 DMF:$H_2O$ hinders the use of *p*-azidothiophenol in SEIRA investigations.

## 3.5 Initial Considerations for a Potential Alternative Chromophore: $SCN^-$

Thiocyanate ($SCN^-$) containing molecules are another class of compounds widely studied via SERS[167,168] and SEIRA.[38] The C-N stretching mode is known to have

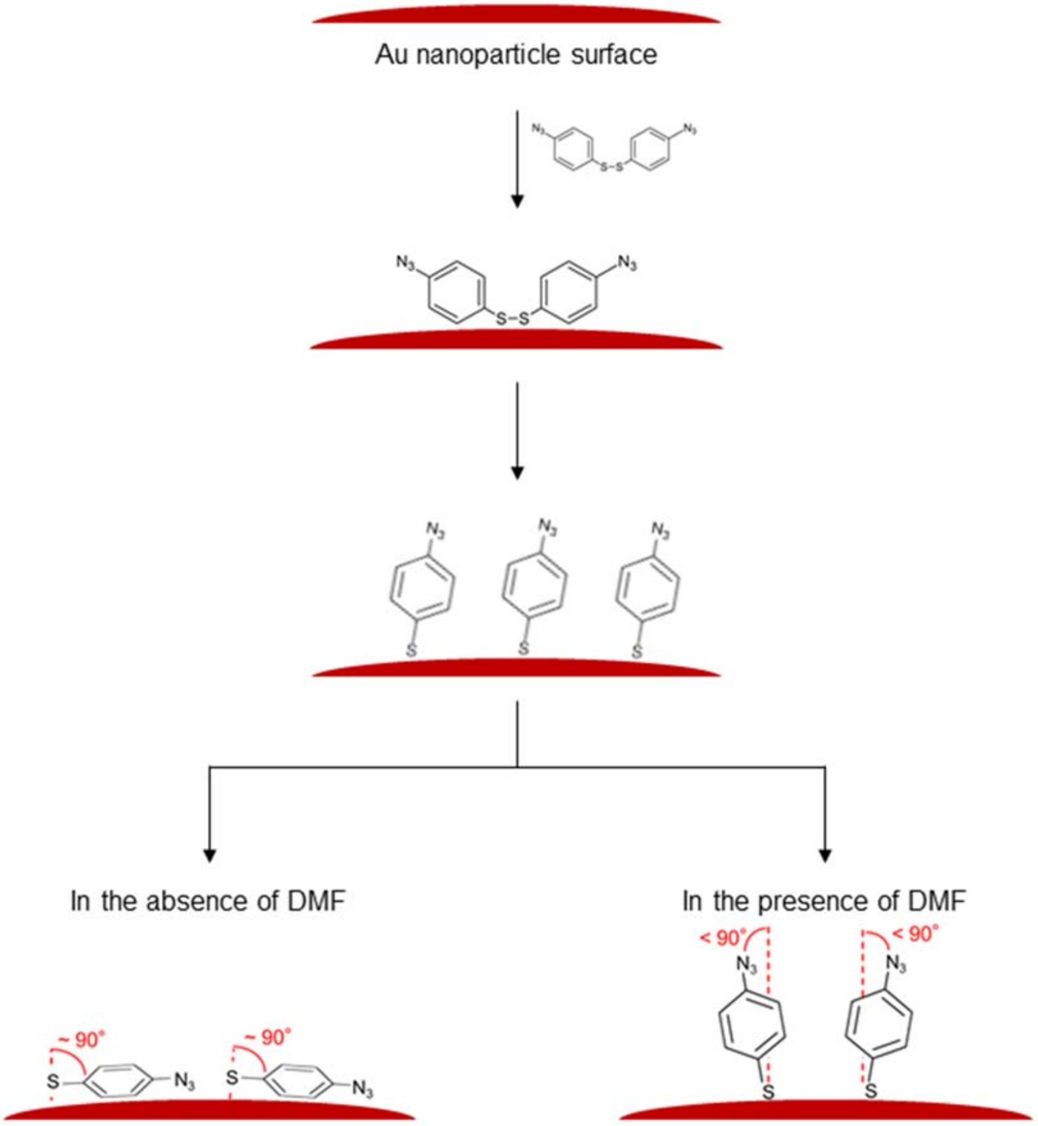

Figure 3.5 Nanoparticle surface functionalization using bis(*p*-azidothiophenol) disulfide where the disulfide bond is broken at the gold nanoparticle surface, and the expected variations in molecular orientation in the absence and presence of 16 mM DMF in the functionalization solvent.

appreciable IR absorptivity,[169,170] thus, sodium thiocyante (NaSCN) was selected as the chromophore for further SEIRA investigations with 1st generation gold nanoparticles. The hydrophilicity of NaSCN allows the potential to overcome the solubility limitations experienced with *p*-azidothiophenol, allowing for larger IR signals, which could be efficiently background subtracted permitting easier observation of signal enhancement spectral changes.

To perform these experiments, a calibration curve was prepared using a series of aqueous solutions ranging from 100 - 500 mM NaSCN. The IR absorption due to the C-N stretching mode of the molecule was observed at 2065 $cm^{-1}$ as indicated in Figure 3.6 (A). The calibration curve obtained using spectra collected at a 25 μm pathlength (fixed pathlength cell) is shown in Figure 3.6 (B), from which the molar absorption coefficient of $SCN^-$ was determined to be 492 $M^{-1}$ $cm^{-1}$ at 2065 $cm^{-1}$. The objective here is to observe evidence of SEIRA; therefore, the IR absorbance at 2065 $cm^{-1}$ of a $SCN^-$ containing 1st generation gold nanoparticle solution is monitored, while the nanoparticle concentration of the sample is increased systematically from 5 to 3000 nM.

## 3.6 Enhancement Experiments with $SCN^-$

Sample containing gold nanoparticles (5 nM), $d$ = 20.4 ± 2.0 nm, suspended in an aqueous solution of 72 mM NaSCN and 1 mM sodium tricitrate (total volume of ~200 mL) was used for the SEIRA experiment. These concentrations were achieved by washing the as-synthesized (~0.5 nM) gold nanoparticles with 1 mM citrate followed by pre-concentration via successive centrifugation steps at 3500 g for 1 hour, followed by the 4 μL/min addition of stock concentrations of $SCN^-$ and citrate to the nanoparticle solution

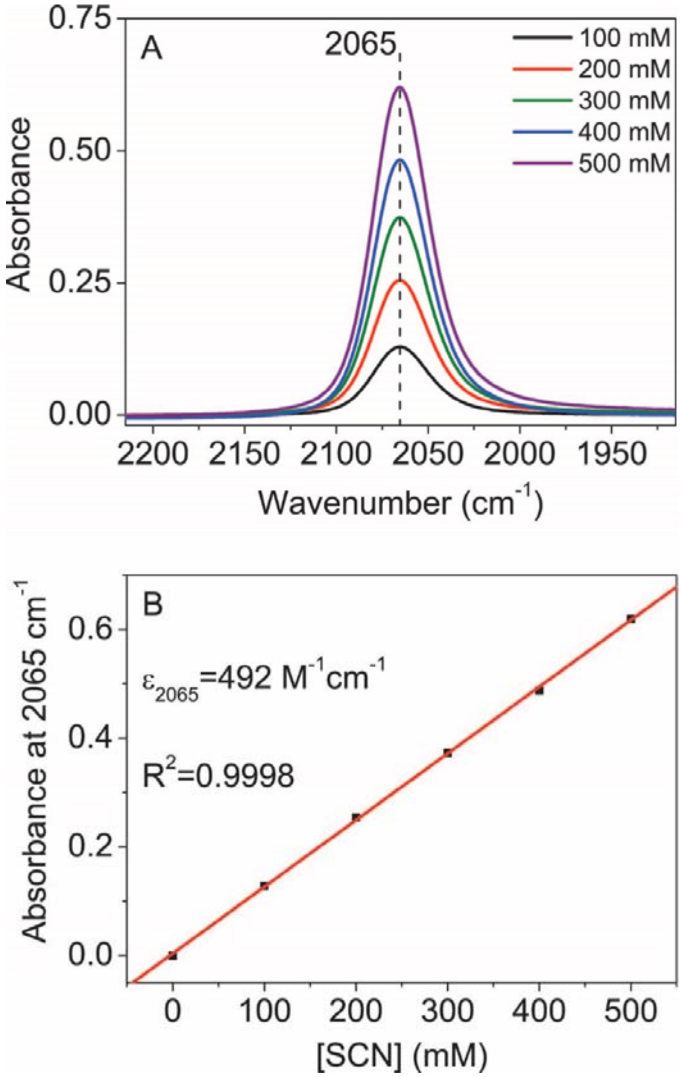

Figure 3.6 (A) The IR absorption of to the C-N stretching mode of $SCN^-$ at varying analyte concentrations and (B) the calibration curve constructed to determine the molar absorption coefficient of the C-N stretching mode at 2065 $cm^{-1}$.

using a syringe pump to achieve the final concentrations given above. After a 1 hour incubation of the experimental sample, an aliquot (~80 μL) was removed, sonicated for 5 minutes, and the LSPR, SERS, and IR spectra were collected using a USB 4000 Ocean Optics UV-Vis spectrophotometer, DeltaNu Advantage 200A Raman spectrophotometer, and a Bruker Tensor 27 FTIR spectrophotometer, respectively. The remaining volume of the experimental sample was then centrifuged at 3000 g for 10 minutes, followed by the removal of a pre-determined volume of the supernatant to achieve a solution with higher nanoparticle concentration, while maintaining the concentrations of $SCN^-$ and citrate constant. Once again, an aliquot (~80 μL) was removed following the redispersion and incubation of the processed experimental sample (nanoparticle concentration > 5 nM) for a period of 1 hour, sonicated for 10 minutes and the LSPR, SERS, and IR spectra were collected. This process was repeated with the remaining volume of the processed sample, centrifuging at 1000 g for 10 minutes in each successive step, until the nanoparticle concentration was increased stepwise up to 3000 nM.

Representative LSPR spectra of 5, 2000, and 3000 nM nanoparticle solutions are shown in Figure 3.7 (A) and (B) after incubation in 78 mM $SCN^-$. The spectral analysis region in panel (B) is extended into the NIR in order to observe more of the broad plasmonic band due to the aggregates. The LSPR spectrum of stable 1st generation nanoparticles at 0.6 nM concentration is indicated in panel (A) for comparison. This result validates the notion that the nanoparticles aggregate under the experimental conditions, while the extent of aggregation increase with increasing nanoparticle concentration. Further, as visible in Figure 3.7 (B), aggregation shifts the plasmonic resonance of the gold nanoparticles into the NIR wavelengths. This, in fact is a favorable plasmonic behavior in

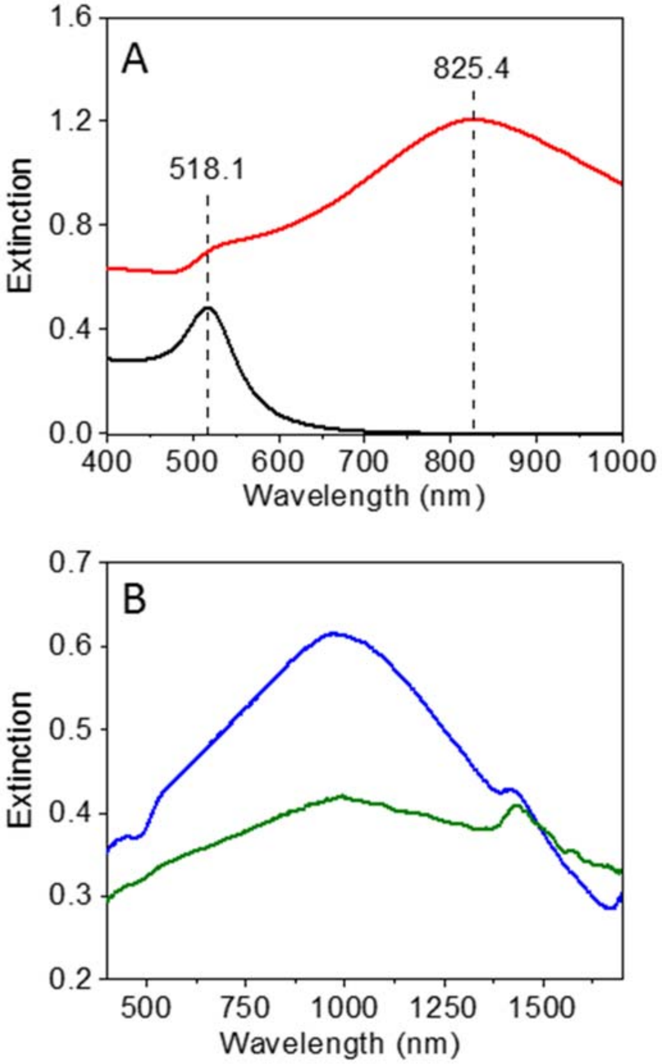

Figure 3.7 LSPR spectra of (A) 5 nM (red), and (B) 2000 (blue) and 3000 (green) nM 1st generation gold nanoparticle samples, containing 72 mM $SCN^-$ and 1 mM sodium citrate. Spectral region in (B) had been extrapolated into the NIR in order to observe the complete broad absorption band due to the formed aggregates. The typical LSPR spectrum of a stable 0.6 nM 1st generation gold nanoparticle sample (black) is indicated in panel (A) for comparison.

terms of observing a SEIRA signal. Unfortunately, however, the nanoparticles were rapidly destabilized as the nanoparticle concentration increased, where sedimentation of the formed aggregates was apparent.

A possible reason for the aggregation of nanoparticles was the high ionic strength (78 mM) used during the experimental flow. To investigate this further, LSPR and SERS spectra were collected for 1st generation gold nanoparticles (13 nM) at a lower SCN$^-$ concentration (12 mM) (An excitation wavelength of 385 nm was used in the SERS measurements), thereby lowering the ionic strength, as indicated in Figure 3.8. The samples were incubated for 24 and 72 hours before recording the SERS spectra whereas the LSPR of the sample was recorded at 24 hours. The comparison of LSPR spectra before and after SCN$^-$ addition as indicated in Figure 3.8 (A) reveal a ~4.5 nm red-shift, a reduction in extinction magnitude by a factor of ~5, and a long plasmonic tail extending into the NIR. This result suggests that aggregation is occurring at a SCN$^-$ concentration of 12 mM and therefore, indicates that the larger (78 mM) ionic strength used in the SEIRA experiment discussed above is clearly a reason for the observed nanoparticle instability. Further, kinetic control of nanoparticle stability becomes increasingly difficult at high nanoparticle concentrations, owing to the increased rate of inter-particle collisions, leading to rapid destabilization especially at significantly large (μM) nanoparticle concentrations as used here (Figure 3.7).

The SERS spectra shown in Figure 3.8 (B) and (C), however, confirm the binding of SCN$^-$ on the nanoparticles via the observation of a SERS signal. Here, the CN stretch was observed at 2151 cm$^{-1}$ for the surface bound SCN$^-$, indicating a shift of 81 cm$^{-1}$ from the Raman signal observed for SCN$^-$ in solution. It is interesting to note that this shift is

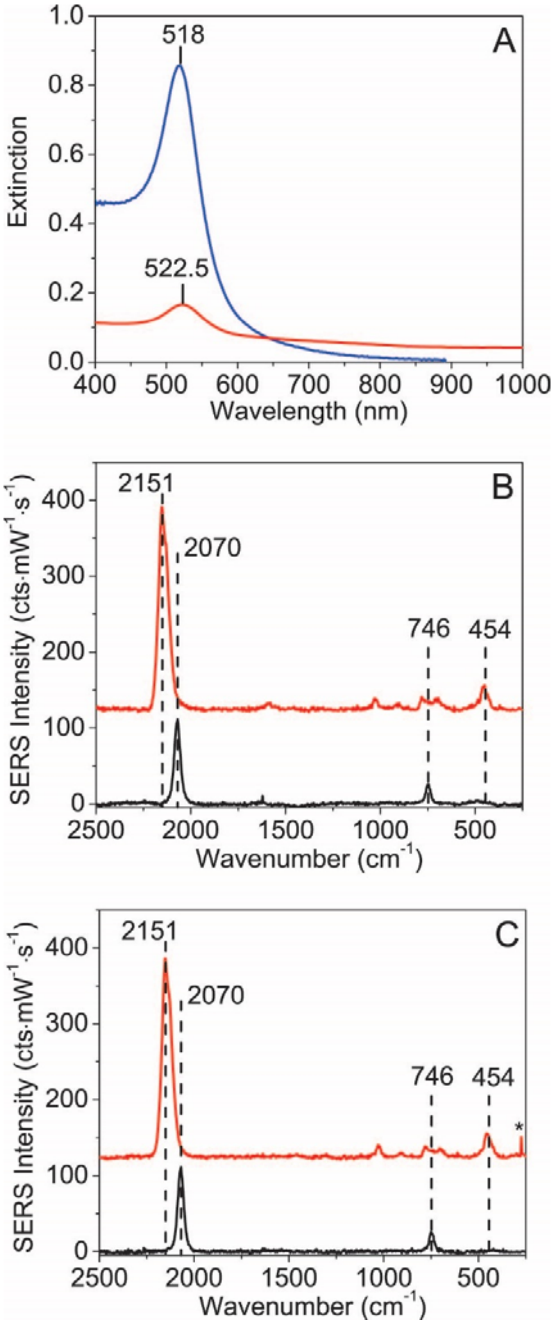

Figure 3.8 (A) LSPR spectra of 0.6 nM 1st generation gold nanoparticles in the absence (blue) and presence (red) of 12 mM $SCN^-$ after incubating for 24 hours, and the SERS spectra collected for 13 nM 1st generation gold nanoparticles containing 12 mM $SCN^-$ (red) after incubating for (B) 24, and (C) 72 hours. The Raman spectrum of a 1 M $SCN^-$ sample (black) is also indicated here for comparison.

consistent with our intuition about bound and unbound $SCN^-$ ions in a system. Specifically, binding of a molecule to a surface changes the electronic structure reflecting a small shift in the bond character, hence shifting the vibrational frequencies of the molecule accordingly. $SCN^-$ ions free in solution are known to exist as a resonance hybridized structure in which there is only partial triple bond character between the C and N. Once bound to a surface via the S, however, the C-N bond achieves triple bond character, whereby the C-N bond strength and hence the stretching frequency would increase. The observed increase in Raman shift, therefore, is consistent with our understanding of the electronic structure of the $SCN^-$ anion. In summary, although the nanoparticles aggregate under the experimental conditions as shown in Figure 3.7, clear evidence of SERS activity is visible in Figure 3.8. Hence, the IR spectra is collected to observe the effect on the presence of nanoparticles on the observed infrared signal.

Representative IR spectra of 500 nM and 3000 nM nanoparticle concentrations are indicated in Figure 3.9, while the spectrum of a sample in the absence of nanoparticles has been indicated for comparison (as 0 nM nanoparticle concentration). Recall that these samples contained 72 and 1 mM, $SCN^-$ and citrate concentrations respectively. A couple of distinctive features are clearly visible in the IR spectra. First, a broad spectral background arises in the presence of nanoparticles, and, second, a new but distorted feature appears in the IR absorption spectrum in the region of the C-N stretching mode. Both features become increasingly prominent as the nanoparticle concentration increases.

As noted, a MIR plasmon resulting from the interactions of the particles appears in the spectrum and increases with increasing nanoparticle concentration. This is consistent with the aggregation predicted in Figure 3.7 and 3.8, and hence we attribute the observed

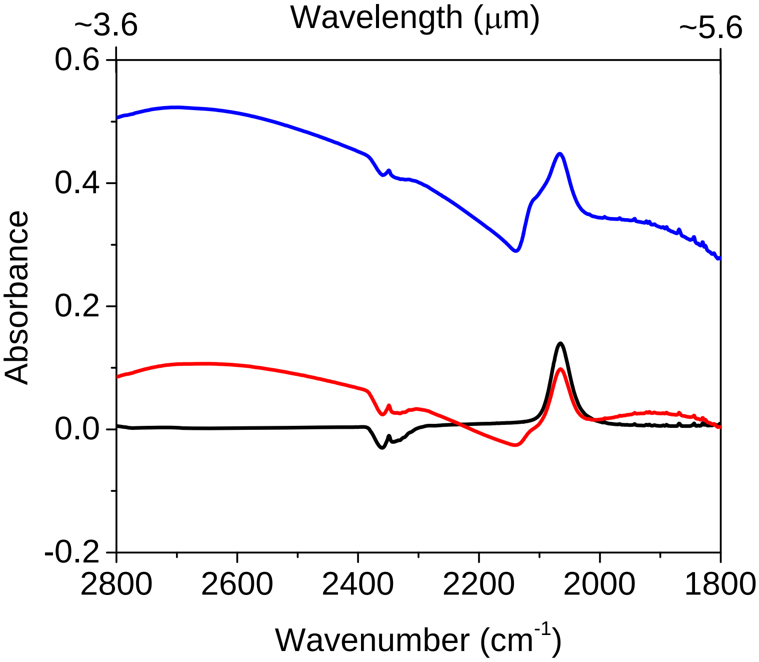

Figure 3.9 IR spectra of samples containing 72 mM $SCN^-$ and 1 mM sodium citrate, at 0 (black), 500 (red), and 3000 nM (blue) concentrations of 1st generation gold nanoparticles. As seen, both the absorption lineshape as well as the spectral background change in the presence of nanoparticles.

background variations to the plasmonic features resulting from the aggregated gold nanoparticles. Further, a closer look at the IR spectra on Figure 3.9 indicates that the absorbance peak due to C-N stretching mode indicates a distorted nature in the presence of nanoparticles, while these distortions become more apparent at the higher nanoparticle concentration. Interestingly however, asymmetric, dispersive lineshapes as seen here, have been previously reported in SEIRA based investigations at the solid-liquid interface.[7]

According to a critical review on vibrational spectroscopy by Osawa, SEIRA bands often have very asymmetric or dispersive shapes, while in some cases, transitions could even be observed as negative peaks (i.e. negative absorption).[7] Lu et. al. had reported the observation of two main features; namely (1) the inversion of IR bands and (2) the enhancement of IR absorbance of the adsorbate in his work on $SCN^-$ adsorbed on electrodes of nanometer thin films of Pt, Pd, and Rh.[38] They attribute this inversion to the differences in absorption frequency for surface-bound $SCN^-$ versus those in the bulk solution, and have also observed similar features with various other surface bound analyte molecules.[38] Akin band inversion behavior has also been reported by Lu, Sun, and Cai for CO adsorbed on Pt and Pd thin layers.[171] In another study by Bjerke and Griffiths, distortions of surface enhanced IR bands have been observed where they attribute the distortion to changes in the refractive index resulting from the close interaction of the analyte molecules with the metal surface.[37]

Alternatively, the anomalies of the absorption lineshapes in SEIRA have been described as a result of Fano resonances: a consequence of the interaction between plasmonic resonances, vibrational modes, and light in nanoscale plasmonic systems.[33] Specifically, the lineshapes here are a result of the interaction between spectrally broad plasmonic excitations and spectrally sharp vibrational modes, where the close coexistence of destructive and constructive interferences result in the observation of characteristic Fano type line profiles.[33,172] In a recent study, Brown et.al. have observed strong infrared spectroscopic enhancements from individual gold nanoantennas, while the dimensions of the individual antenna structures were tuned to enhance the IR modes of specific chemical moieties.[31] Interestingly, they observed that if a metallic antenna structure has a plasmon resonance at the same frequency as a molecular vibration, the metal and molecule system can couple, resulting in spectral features with Fano lineshapes.[31] Hence, such Fano type line profiles are believed to be involved in the unprecedented signal enhancement occurring when vibrational excitations of a molecule are coupled with a plasmon resonance,[31,173] thus being characteristic of SEIRA.

## 3.7 Modelling the Spectroscopic Origin of Anomalous Lineshapes

Here, we attempt to model the spectroscopic origin of anomalous lineshapes in SEIRA using the fundamentals of molecular spectroscopy as follows. In a typical molecular spectroscopic experiment, specific vibrational modes of an analyte are excited by the interaction with an incoming incident laser pulse. The convolution of the molecular response created here ($R$) by the envelope of the incident laser pulse ($E_{inc}$) produces a macroscopic polarization ($P$) with a 90° phase shift with respect to $E_{inc}$ such that:

$$P \propto iRE_{inc} \tag{3.1}$$

This gives rise to an emitted signal field ($E_{sig}$) with a 180° phase shift with respect to $E_{inc}$. i.e.

$$E_{sig} \propto iP \propto i^2 R E_{inc} \tag{3.2}$$

In a typical setup, a spectrometer is used to measure the emitted electric field.[2] Typical IR detectors used in spectrophotometers are square-law detectors that can only measure intensities ($I_{meas}$), and not electric fields such that:

$$I_{meas} = \left| E_{sig} + E_{inc} \right|^2 \tag{3.3}$$

This can now be simplified to the form,

$$I_{meas} = \left| E_{inc} \right|^2 + \left| E_{sig} \right|^2 + 2\Re\left( E_{sig} E_{inc}^{*} \right) \tag{3.4}$$

where the first and second term give the incident ($I_{inc}$) and signal ($I_{sig}$) electric field intensities, respectively. The signal electric field intensity is comparatively small and thus is negligible. The third term in the above expression relates to the interference between $E_{sig}$ and $E_{inc}$.

To isolate this interference term, which contains the information of interest, one usually calculates the absorbance to subtract off the spectrum of the laser pulse (to first order) such that:

$$A = -\log\left( \frac{I_{meas}}{I_{inc}} \right) = -\log\left( \frac{I_{inc} + 2\Re\left( E_{sig} E_{inc}^{*} \right)}{I_{inc}} \right) \tag{3.5}$$

For small values of absorbance, the above expression can be approximated as;

$$A \approx 2\Re\left( E_{sig} E_{inc}^{*} \right) \tag{3.6}$$

Hence as derived above, what is actually detected in a typical molecular spectroscopic experiment is the interference between the incident and signal electric fields.

Furthermore, it can be shown that the detected electric field ($E_{\text{detect}}$) due to the interaction of $E_{inc}$ and $E_{sig}$, has the form of a free induction decay and can be modelled using a time ($t$) dependent function of the form:

$$E_{\text{detect}}(t) \propto \left[\cos(\omega_0 t)\right] e^{-gt} \tag{3.7}$$

where $\omega_0$ is the frequency resulting from the electric field interaction and $g$ is the lineshape factor. This can be transformed into the frequency domain via Fourier transformation to obtain a complex valued Lorentzian function of the form;

$$E_{\text{detect}}(\omega) \propto \frac{1}{i(\omega-\omega_0)-g} \tag{3.8}$$

This complex function can be rewritten as,

$$E_{\text{detect}}(\omega) \propto -\frac{g}{(\omega-\omega_0)^2+g^2} - i\frac{(\omega-\omega_0)}{(\omega-\omega_0)^2+g^2} \tag{3.9}$$

The first term in the above expression is real and the second term is imaginary. Recall that $E_{sig}$ has a 180° phase shift with respect to $E_{inc}$ as given by equation 3.3. Therefore, the interference of the electric fields $E_{sig}$ and $E_{inc}$ introduces two additional $i$ terms into the above expression ($i^2 = -1$), hence preserving the real and imaginary contributions to $E_{\text{detect}}$. Further, IR detectors can only measure real and not imaginary quantities. Thus, in heterodyned detection we only observe the real part of an emitted electric field. Hence, only the first term in the complex valued $E_{\text{detect}}$ expression will be detected. This term has an absorptive lineshape as shown in Figure 3.10 (A). Therefore, in heterodyne detected IR spectra, we generally observe absorptive lineshapes.[2] This behavior is typical of analyte molecules equilibrated in solution.

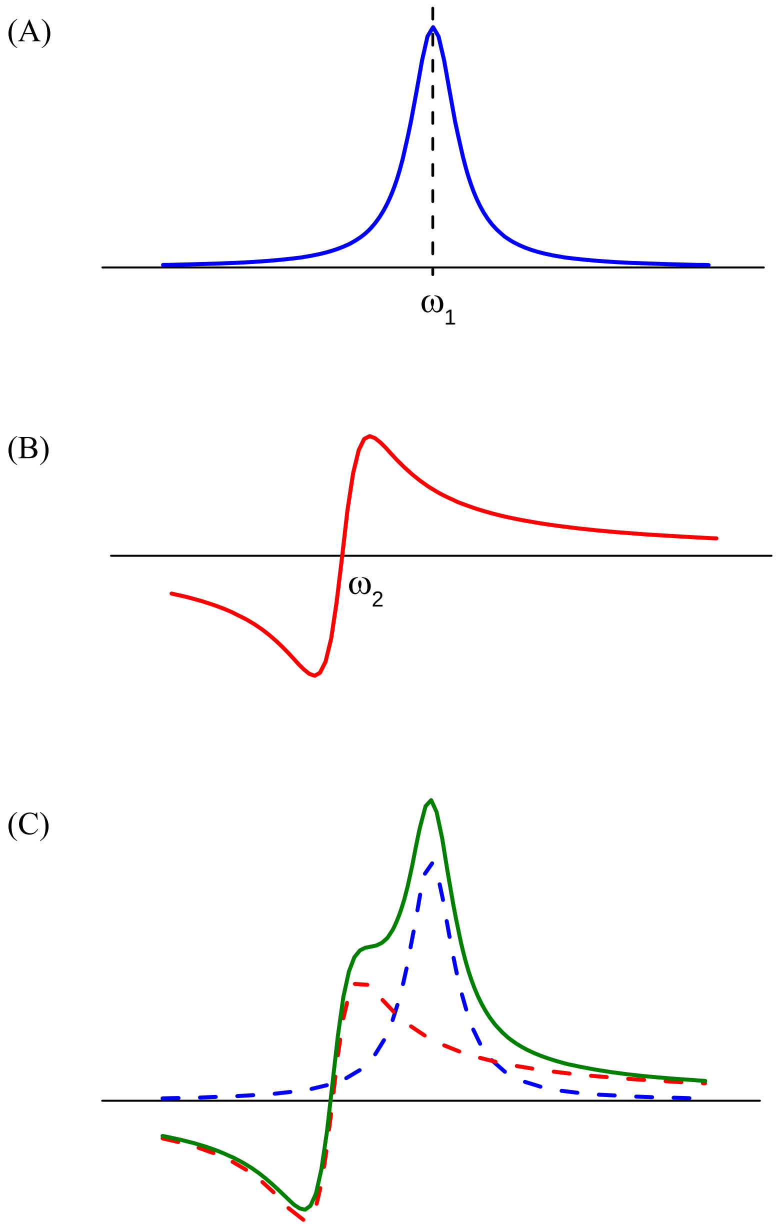

Figure 3.10 Examples of (A) a Lorentzian lineshape centered at $\omega_1$, (B) a dispersive lineshape centered at $\omega_2$ ($\omega_1 \neq \omega_2$), and (C) the lineshape obtained by the combination of overlapping Lorentzian and dispersive contributions.

In the case of surface-bound molecules, however, the above description has to be modified to account for the possibility of additional electric fields to exist giving rise to enhancement effects. Once again, we start by saying the macroscopic polarization induced in the molecule ($P_{mol}$) in the presence of the incident electric field is such that:

$$P_{mol} \propto iRE_{inc} \tag{3.10}$$

This gives rise to an electric field 180° out of phase with respect to $E_{inc}$ as below.

$$E_{mol} \propto iP_{mol} \propto i^2 RE_{inc} \tag{3.11}$$

According to previous studies, for systems in which nanoparticle bound chromophores are present, the polarization response due to the surface bound chromophores can create image charges in the nanomaterial.[174] This antenna effect creates a macroscopic polarization due to the nanoparticles ($P_{ant}$) such that:

$$P_{ant} \propto iP_{mol} \propto i^2 RE_{inc} \tag{3.12}$$

which will be 180° out of phase with respect to $E_{inc}$. These image charges behave as effective antennas which produce their own electric field, typically with a 90° phase shift from the above polarization response ($P_{ant}$) such that:

$$E_{ant} \propto iP_{ant} \propto i^3 RE_{inc} \tag{3.13}$$

Hence, overall the electric field due to this antenna effect will be 270° out of phase with respect to $E_{inc}$ as shown in equation 3.14.

Importantly, nanoparticles produce an intrinsic macroscopic polarization ($P_{NP}$) and hence an electric field ($E_{NP}$) resulting from their plasmonic properties in the presence of an external electric field. It can be shown that $P_{NP}$ is 90° out of phase with respect to $E_{inc}$ such that,

$$P_{NP} \propto iRE_{inc} \qquad (3.14)$$

Further, $E_{NP}$ can be related to $P_{NP}$ as follows (note the 180° phase shift with respect to $E_{inc}$):

$$E_{NP} \propto iP_{NP} \propto i^2 RE_{inc} \qquad (3.15)$$

Now, the intensity detected in the presence of nanoparticles will carry contributions from $E_{inc}$, $E_{mol}$, $E_{ant}$, as well as $E_{NP}$ such that;

$$I_{meas} = \left|E_{inc} + E_{mol} + E_{ant} + E_{NP}\right|^2 \qquad (3.16)$$

Recall, that in a typical experiment what is actually reported is absorbance. Absorbance in the presence of nanoparticle can be shown to have the form;

$$A \approx 2\Re\left[\left(E_{mol}E_{inc}^*\right) + \left(E_{NP}E_{inc}^*\right) + \left(E_{mol}E_{NP}^*\right) + \left(E_{ant}E_{inc}^*\right) + \left(E_{mol}E_{ant}^*\right) + \left(E_{NP}E_{ant}^*\right)\right] \qquad (3.17)$$

analogous to the derivation of equation 3.7. Further, as proven above, both $E_{mol}$, and $E_{NP}$ are 180° out of phase with respect to $E_{inc}$. Hence the first two interactions above will allow the real (absorptive) part in equation 3.10 to be detected. The third term measures the interference between two in-phase fields, once again allowing the real part of the complex Lorentzian lineshape to be detected.

However, $E_{ant}$ is 270° out of phase with respect to $E_{inc}$ giving rise to a factor of $i^3$, and hence the measured signal due to the interaction between $E_{ant}$ and $E_{inc}$ will be the imaginary part of the complex Lorentzian lineshape in equation 3.10, which has a dispersive lineshape as indicated in Figure 3.10 (B). Similarly, both $E_{NP}$ and $E_{mol}$ are 90° out of phase with respect to $E_{ant}$ and once again the dispersive contribution to $E_{\text{detect}}$ will be measures due to the last two interactions in the above expression. So in essence, it is clear that in the presence of nanoparticles, the detected signal will carry both absorptive and dispersive lineshape contributions. Further, a given experimental system would often contain both surface bound and unbound molecules in a dynamic equilibrium. Notably, the absorption due to the free or surface-unbound analyte often occurs at a shifted frequency due to the changes in the electronic structures of the bound and unbound analyte as discussed previously for $SCN^-$ (*vide supra*). Hence, the overlap of these frequency-shifted absorptive and dispersive contributions will lead to the observation of anomalous lineshapes as shown in Figure 3.10 (C).

It is interesting to note that the third interaction term above represents the interaction between a broad plasmonic feature ($E_{NP}$) and a narrow molecular signal ($E_{mol}$) in-phase with each other. This is characteristic of a Fano type resonance, where the interaction between spectrally broad plasmonic excitations and spectrally sharp vibrational modes give rise to distinct lineshapes.[33] Therefore, the model developed above is capable of explaining the origin of anomalous lineshapes in SEIRA, although the relative contributions of dispersive or Fano-type lineshapes giving rise to the overall observed lineshape cannot be directly determined.

The absorption observed here for nanoparticle bound $SCN^-$ indicate characteristics features of a distorted lineshape, where absorptive and dispersive (or Fano type) contributions are clearly visible as shown in Figure 3.9. Further, the absorptive feature here is centered at ~2065 $cm^{-1}$, whereas the dispersive feature is centered at ~2121 $cm^{-1}$. This difference in the bound versus unbound chromophore absorptions, both in direction as well as magnitude of shift, is comparable to those observed with the SERS data. It should, however, be noted that an exact value for the center of the dispersive lineshape cannot be determined here owing to multiple reasons. Notably, (1) the dispersive signal may have different amplitudes in the positive and negative direction, (2) the dispersive feature is clearly overlapping with the absorptive lineshape due to the SCN$^-$ in solution, and (3) the signal is sitting on a large plasmonic background, all of which make the estimation of the peak center challenging.

Nevertheless, it is clear that the observed distortions of the infrared signal is characteristic of the electromagnetic coupling between the nanoparticle substrate and the surface-bound chromophore, thus being clear evidence of a SEIRA. Thus, the results observed here indicate promising potential for SCN$^-$ to be used as an efficient SEIRA probe in future experiments. Unfortunately, however, nanoparticle stability could not be retained under the experimental conditions, suggesting that an alternate plasmonic material which could withstand the experimental conditions used here, while at the same time indicating plasmonic features in the MIR is warranted in moving forward.

## 3.8 Summary, Conclusions and Future Direction

The objective of this study was to observe a solution-phase SEIRA signal via a suitable chromophore bound on spherical gold nanoparticles. A series of experiments were conducted to observe a SEIRA signal using *p*-azidothiphenol and SCN$^-$ bound to 1st generation spherical gold nanoparticles. No change in signal was observed in the *p*-azidothiphenol based SEIRA experiments, because of (1) low nanoparticle concentration, (2) instability of the nanoparticles in the presence of DMF, and (3) small enhancement factors associated with SEIRA.

SCN$^-$ was then selected as an alternative chromophore, where experiments were conducted by replacing the citrate molecules on the nanoparticles with SCN$^-$ anions. IR spectra were collected at various nanoparticle concentrations as to observe evidence of

SEIRA. Interestingly, IR spectra collected in the presence of nanoparticles indicated clear band distortion, and signs of a plasmonic background, specifically at the higher nanoparticle concentrations. Such IR band distortion has been commonly observed in relation to previous solid state SEIRA investigations.[7] Interestingly, the combination of the shifted frequency and the dispersive lineshape observed in these experiments, therefore, provide direct evidence of SIERA.

Generally, spherical nanoparticles are easy to synthesize, stable in solution and widely studied compared to other morphological forms of nanoparticles, and was thus used in these preliminary solution-phase SEIRA investigations. The plasmonic properties of spherical nanoparticles are, however, much less interesting compared to the more complicated morphologies. Nevertheless, various other morphological forms of gold as well as other noble metals are well known to exhibit plasmonic behavior which is extended into the NIR, or even the MIR wavelengths under unique conditions. With the better understanding of SEIRA obtained in these preliminary investigations, there is great potential for alternative nanostructures with IR plasmonic behavior to be used in the observation of a solution-phase SEIRA signal. Hence, the potential future direction of this study would be in elucidating better plasmonic materials that allows easy and efficient infrared enhancements to be realized in solution, via a suitably bound chromophore.

# CHAPTER 4

# SYNTHESIS AND CHARACTERIZATION OF PLASMONIC MATERIALS WITH INFRARED ABSORPTION PROPERTIES

## 4.1 Motivation: Nanoparticle Morphology and the Ensuing Optical Properties

Many metallic nanoparticles exhibit dipole resonance spectral features in the ultraviolet (UV) and visible (VIS) regions of the electromagnetic spectrum.[175] For instance, spherical gold nanoparticles, show strong dipole resonances in the visible region between 520 - 550 nm originating from the collective oscillations of the free electrons (6s electrons of the conduction band in the case of gold), with the plasmon wavelength varying based on the size, shape, and the aggregation state of the nanoparticles as well as their local dielectric environment.[176] The plasmonic properties of metallic nanostructures are strongly dependent on their structure and composition.[175] Thus, the localized surface plasmon resonance (LSPR) of the materials can be shifted into the near infrared (NIR) or even the mid infrared (MIR) regions of the electromagnetic spectrum via anisotropic morphologies such as nanotriangles,[177] nanoantennas,[31] nanostars,[176,178] and tetrapods.[179] Alternatively, these lower energy spectral features can be generated by varying the distance between nanostructures,[180] thus giving rise to intensified electric fields. Both strategies can yield nanoparticles with plasmonic properties that can be exploited for surface enhanced Raman and infrared spectroscopies (SERS and SEIRA).

Unlike in the case of spherical nanoparticles suspended in a uniform medium, the plasmon resonance of non-spherical architectures reveal multiple, yet characteristic plasmonic features. For instance, LSPR spectra of ellipsoids or nanorods reveal a longitudinal mode and a higher energy transverse mode.[176,181] Similar multi-polar plasmon resonance spectra contain long wavelength spectral features, which have the potential to be utilized in SEIRA, SERS, as well as other LSPR sensing applications.[182] Because radiation dampening and other dielectric constant properties increase with increasing particle size in general,[183] these NIR and MIR properties are more difficult to observe and exploit for surface enhanced spectroscopies such as SEIRA.

## 4.2 Plasmonic Properties of Gold Nanostars

One nanoparticle architecture that gives rise to NIR plasmon resonances are branched nanostructures. Branched gold nanostructures are complex architectures with plasmon resonances that can be tuned by controlling the diameter of the core particle as well as the length and density of the protruding branches.[184,185] These nanostructures are generally composed of a core that serves as an efficient nanoscale antenna, which couples to the protruding branches (also known as tips, spikes, or arms) thereby giving rise to unique and tunable optical properties.[185] For example, gold nanostars, can be modelled as truncated spheres with protruding prolate spheroidal tips. The optical properties of these materials can be explained using a hybridization model between the plasmon energies of the core and the tips of the nanostructures.[182] As such, the anisotropic optical properties of gold nanostars exhibit plasmon resonances that were strongly dependent on the size (length and width) of the protruding tips.[182]

Furthermore, these nanostar architectures exhibit multiple plasmon resonance features.[186] Specifically, the high energy plasmon resonance feature of nanostars arise from branch tips and the particle core. Mixing of the plasmon modes dramatically increases the extinction cross-section of the high energy mode(s).[182] This mixing, in turn, results in very large electric field enhancements compared to those originating from individual tips,[182,185] making gold nanostars a preferred substrate for many applications where intense electric fields are desired. The conduction electrons that resonate at high energies compared to those associated with the tips couple adiabatically. The low energy oscillations increases the effective dipole moment of the high energy resonance, giving rise to both increased extinction cross-sections as well as electric field enhancements of the low energy nanostars plasmonic modes.[182]

Of note, the antenna effect associated with the gold nanostar cores generates "extraordinary" electromagnetic near-fields at the sharp tips, which decay exponentially tens of nanometers from the tip surface[185] thus enabling a range of applications including highly sensitive LSPR sensing,[187] SERS,[188] biomedicine,[189] and thermosplasmonics.[190] For instance, Hrelescu et. al. recently demonstrated that gold nanostars give rise to SERS enhancements up to $10^7$ from individual nanostars. Impressively, these signal enhancements were observed without aggregation or resonance Raman mechanisms.[191] Instead, this phenomenon was attributed to molecules at the nanostar tips where the electric field strengths are largest,[191] making gold nanostars a promising architecture in all surface enhanced spectroscopies.

One limitation in using branched gold nanostructures in applications arises from the reagents used to grow these materials. For instance, the growth of gold nanostars requires a selective capping of the face-centered cubic lattice planes for growth of other planes.[186] Although seed-mediated growth in aqueous media with various capping agents such as cetyltrimethylammonium bromide (CTAB), polyvinylpyrrolidone, sodium citrate, etc. results in anisotropic nanostructures, produced materials suffer from heterogeneity, plasmon damping, linewidth broadening etc.[185] Alternatively, gold nanostars can be synthesized directly using a seedless one-step redox reaction, using a Good's buffer such as HEPES (4-(2-hydroxyethyl)-1-piperazineethanesulfonic acid) as the capping agent.[178,179] These synthetic routes result in nanostars with modulating geometries that depend on buffer concentration, $Au^{3+}$ concentration, and the pH of the buffer.[185] As such, the optical properties of these materials can be tuned throughout the visible region of the electromagnetic spectrum.

Here, gold nanostars are synthesized using 2-[4-(2-hydroxyethyl)-1-piperazenyl] propanesulfonic acid (EPPS) ($pK_a$ = 8.4[192]) as both the buffer and reducing agent. This straightforward, seedless, and one-pot synthesis is used to vary the geometry of the synthesized nanostars by simple modification of the buffer concentration. Several features are noted. First, the gold nanostars exhibit up to three distinct plasmon features in the visible and infrared wavelengths. Second, these features are sensitive to the buffer concentration used during synthesis and are consistent with those previously reported for gold nanostars synthesized via alternative methods.[176,178] Finally, the nanostars remain stably suspended in aqueous media for weeks without any visible signs of aggregation. Accordingly, these nanostructures are promising for solution phase surface enhanced spectroscopy in the NIR and MIR.

## 4.3 Synthesis of Gold Nanostars via Solution-phase Redox Chemistry

The crystallographic planes of a metal influences the rate of growth to form branched nanocrystals following homogeneous nucleation.[178] Xie et. al., for instance, reported three-dimensional branched gold nanocrystals containing one to eight tips at high yield (ca. 92%) could be synthesized via the simple reaction of an aqueous solution of chloroauric acid with the Good's buffer, 2-[4-(2-hydroxyethyl)-1-piperazenyl] ethanesulfonic acid (HEPES) (Figure 4.1 (A)) at room temperature.[178] While the mechanism of formation of gold nanostars is not fully understood, several strategies were previously hypothesized. First, a detailed analysis conducted by Liu et. al. revealed that high concentrations of HEPES (i.e., roughly 3000-fold excess of HEPES to gold salt) facilitated the long-range ordering of HEPES thus forming soft templates for the direct formation of anisotropic gold nanoparticle growth.[179] Furthermore, density functional theory (DFT) calculations predicted that the sulfonate groups of HEPES molecules bind to the gold surfaces while the free hydroxyl groups facilitate the self-assembly and bilayer formation of the soft template via hydrogen bonding.[179] Thus, the dual roles of the HEPES in reducing the gold salt while at the same time directing anisotropic growth allows the achievement of morphological control. In contrast, mechanisms at smaller ratios of HEPES to gold salt resulted in the formation of gold nanostars through piperazine ring directed capping and reduction.[176,178,185] Whether high or low HEPES to gold ratios are used, gold nanostars form and their optical properties can be characterized.

Given the importance of the Good's buffer reagent, varying the composition of the molecule is expected to impact gold nanostar morphology. 2-[4-(2-hydroxyethyl)-1-

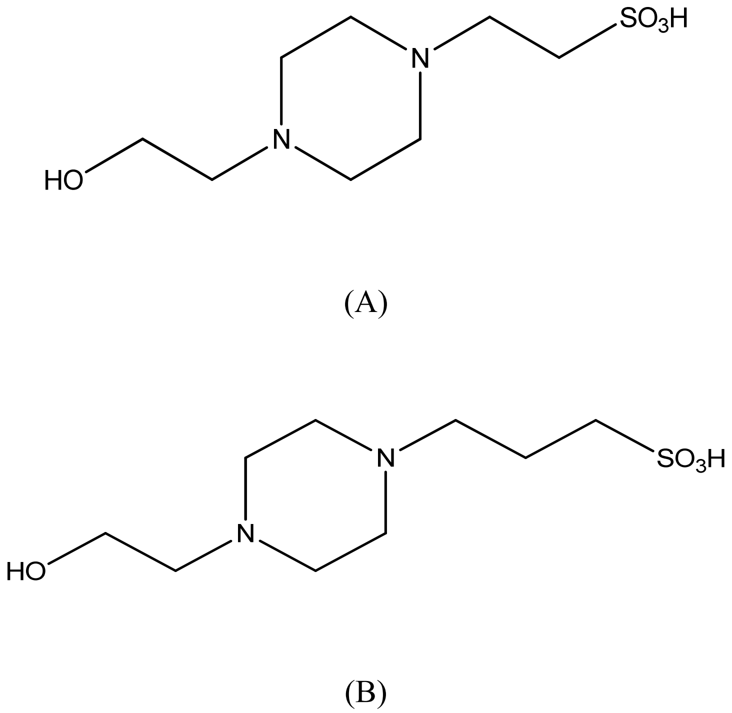

Figure 4.1 Chemical structures of (A) 2-[4-(2-hydroxyethyl)-1-piperazenyl] ethanesulfonic acid (HEPES) and (B) 2-[4-(2-hydroxyethyl)-1-piperazenyl]propanesulfonic acid (EPPS). As can be seen, the two molecules are similar in functionality, and differ only by the additional $-CH_2-$ group between the piperazine ring and the sulfonic acid group. (Note that the sulfonic acid moiety of EPPS is deprotonated at the pH of 7.4 used during synthesis)

piperazenyl]propanesulfonic acid, more commonly known as EPPS buffer (Figure 4.1 (B)), is functionally similar to HEPES but contains an additional -$CH_2$- group between the piperazine ring and the sulfonic acid group. According to previous studies, EPPS can be successfully used in synthesizing gold nanostars, under identical experimental conditions used with HEPES.[179] Furthermore, the presence of a longer alkane chain provides a template for the formation of longer branches versus those synthesized with HEPES thus giving rise to plasmonic features that are shifted into the infrared.

To evaluate implications of buffer on star properties, gold nanostars were synthesized using chloroauric acid and the Good's buffer EPPS via a one-step, solution-phase redox chemistry reaction, where EPPS acts as the buffer as well as the reducing agent (*vide infra*). All glassware were cleaned with Aqua Regia (HCl:$HNO_3$ in a 3:1 ratio by volume) and rinsed with Nanopure water. A 1 M stock solution of EPPS was prepared in Nanopure water (initial pH ~5.9), and the pH was adjusted to 7.4 ± 0.1 at 25 °C with 1 M NaOH. The stock concentration of EPPS was adjusted to reflect the volume of NaOH added during the pH adjustment (After pH adjustment the stock concentration of EPPS was ~850 mM). Solutions (5.00 mL) of different EPPS concentrations (20, 40, 50, 60, 80, 100, 200, 300, and 400 mM) were prepared by diluting the EPPS stock with Nanopure water. Finally, 50 µL of 20 mM $HAuCl_4$ solution was added to each solution followed by gentle swirling of the reaction vessel (20 mL glass vials). The solution was then allowed to react overnight. The color of the incubated solutions changed from colorless to red, blue, or green depending on the EPPS concentration. The resulting nanoparticle solutions were analyzed (*vide infra*). In addition, gold nanostars at 40 mM EPPS or HEPES were prepared under identical experimental conditions to compare how buffer composition influenced the optical properties of the materials.

## 4.4 Mechanism of Gold Nanostar Formation

In a study by Habib et. al., the mechanism of nanostar formation by various Good's buffers was extensively investigated using electron spin resonance (ESR) and cyclic voltammetry (CV).[176] Here, the CV data indicated the mild reducing ability of the Good's buffers and the ESR data indicated the generation of nitrogen-centered cationic free radicals from the Good's buffers in the presence of Au(III). Corresponding to their findings with various other Good's buffers, the mechanism of forming gold nanostars using EPPS can be summarized as below.

$$\text{Au(III)} + \text{EPPS} \rightarrow \text{Au(II)} + \text{Cationic free radicals of EPPS}$$

$$2\text{Au(II)} \rightarrow \text{Au(III)} + \text{Au(I)}$$

$$\text{Au(I)} + \text{EPPS} \rightarrow \text{Au(0)} + \text{Cationic free radicals of EPPS}$$

$$n\text{Au(0)} \rightarrow (\text{Au(0)})_n\text{, gold nanostars}$$

$$\text{Cationic free radicals of EPPS} + O_2 \rightarrow \text{Degraded products}$$

## 4.5 Effect of Reducing Agent: HEPES versus EPPS

The optical properties of the synthesized nanostars were characterized using UV-visible spectroscopy. All extinction measurements were collected using a UV-visible spectrophotometer (BWTEK *i*-trometer) configured in transmission geometry and polymethyl methacrylate cuvettes with a 5 mm pathlength.

The synthesis of gold nanostars with HEPES is well-studied[176,178,179] and replacing this well-known reducing agent with a different reagent is expected to impact the optical and/or structural properties of the synthesized product. For instance, LSPR spectra of gold nanoparticles prepared with 40 mM HEPES or EPPS are shown in Figure 4.2. Clear impacts of the reducing agent/buffer composition are observed. Two resonance features are observed. The first is a shoulder feature centered at ~530 nm and is consistent with the plasmonic properties of the gold core. The more intense spectral feature is observed at longer wavelengths and is consistent with branch properties. This plasmon feature is located at ~630 nm and ~652 nm for HEPES and EPPS products respectively. The observed red-shift likely results from changes in nanostructure geometry and the extent of plasmonic hybridization of the core and the individual tips of the synthesized nanostructures. Importantly, the longer hydrocarbon chain in the reducing agent EPPS facilitates directional growth as with HEPES. In summary, therefore, EPPS can be used as a reducing agent in the synthesis of gold nanostars where the visible extinction properties are qualitatively similar to those synthesized via well-established protocols using HEPES as the reducing agent.

## 4.6 Effect of Buffer Concentration: Optical and Structural Variations

The concentration of buffer reagent should impact gold nanostructure morphology (i.e., branch length and/or core diameter). To evaluate these trends, EPPS concentration was varied from 20 and 400 nM during the synthesis of gold nanostars. Photographs of the resulting suspensions are shown in Figure 4.3. The solution color varies from red, purple, blue, green, and grey with increasing EPPS concentration. To better understand the source

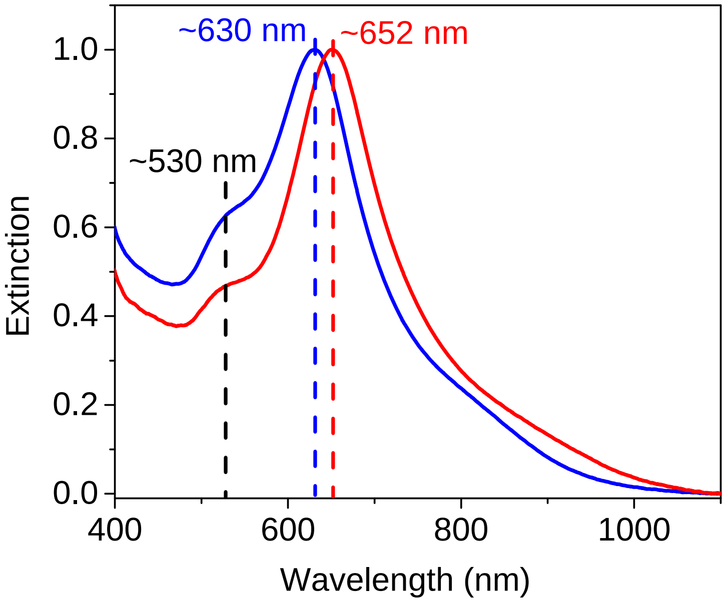

Figure 4.2 Comparison of the LSPR spectra of gold nanostars synthesized at 40 mM buffer concentration where (A) HEPES and (B) EPPS is used as the buffer. As can be seen there is a red shift in the extinction maximum wavelength ($\lambda_{max}$) when EPPS is used versus HEPES.

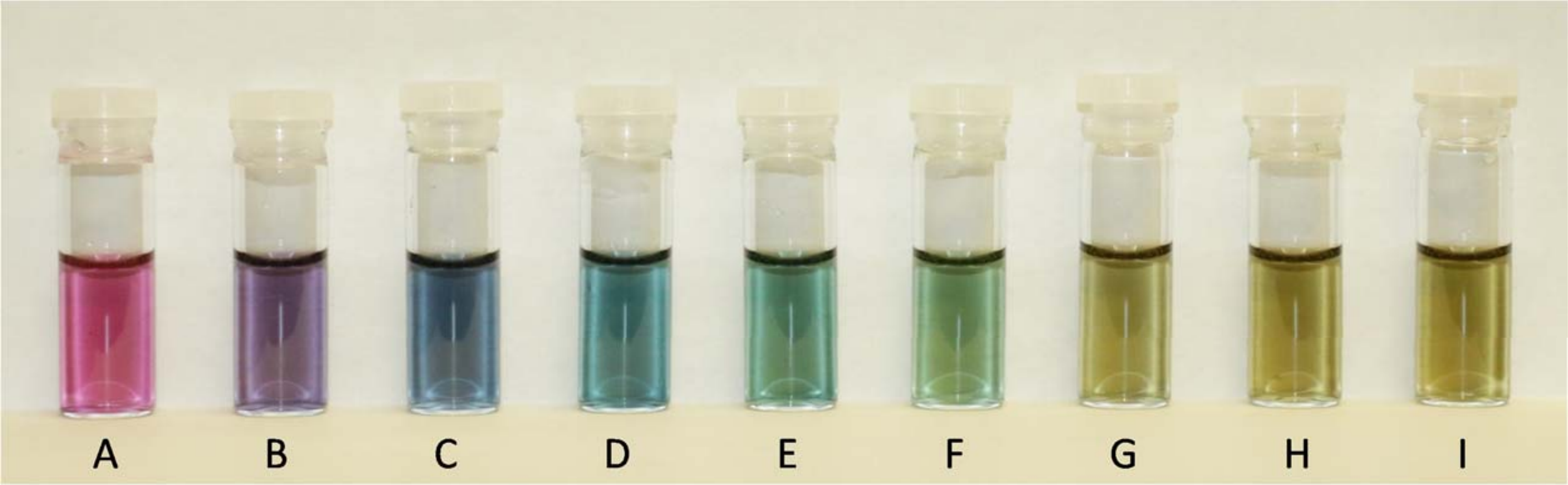

Figure 4.3 Photographs of gold nanostar solutions synthesized at 20, 40, 50, 60, 80, 100, 200, 300, and 400 mM EPPS concentrations going from A to I respectively. As can be seen, the color of the solutions change from red, purple, blue, green, to grey.

of these colors, LSPR spectra are collected and shown in Figure 4.4. Several features are noted. First, a small resonance centered at 565 ± 17 nm is observed for all samples (Table 4.1). Second, a low energy secondary feature shifts to longer wavelengths, then saturates as EPPS concentration increase (Table 4.1). This suggest that branch length is increasing with increasing EPPS concentration.[185] Finally, resonances, that extend beyond the visible wavelengths (*vide supra*) are observed and become increasingly prominent at the highest buffer concentration.

In addition, the magnitude of the longest visible resonance extinction at the $\lambda_{max}$ increases with increasing buffer concentration until a ~100 mM EPPS concentration is used. Given the growth mechanism of the nanostars, not all gold salt should be consumed. This is confirmed via analysis of residual choloroauric (at ~387 nm, see Figure 4.5). Thus, the variation in the extinction at the lowest energy visible $\lambda_{max}$ likely stems from the synthesis of nanoparticles with higher extinction coefficients as the buffer concentration increases. Previously, the large extinction cross-sections of gold nanostars were shown to stem from the coupling of electric fields due to the core and the protruding tips,[182] which in turn are sensitive to structural variations caused by varying buffer concentrations.

In order to better understand morphological variations caused by changing the buffer concentration, samples of synthesized gold nanostars were imaged using transmission electron microscopy (TEM). Aliquots (500 µL) of the nanoparticle solutions at EPPS concentrations of 100 and 400 mM were selected for imaging as these exhibited the most encouraging results for IR applications. As the high salt concentrations in the as-synthesized often interferes with imaging, the samples were centrifuged in 2 mL centrifuge tubes at 2000 g (4615 RPM) for 30 minutes using a microcentrifuge (Eppendorf Centrifuge

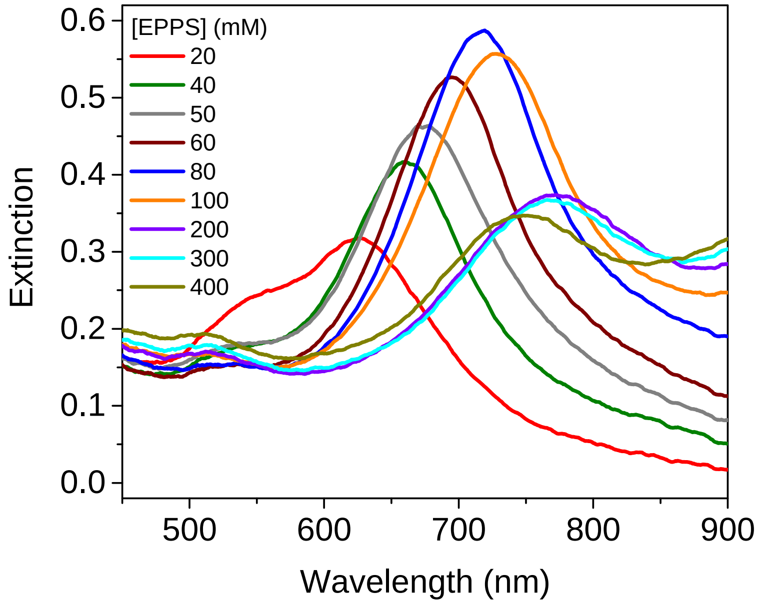

Figure 4.4 LSPR spectra of gold nanostars synthesized using 20 - 400 mM EPPS. Note the wavelengths of maximum extinction as well as the magnitude of the extinction at this wavelength systematically changes with EPPS concentration. Notably, there is evidence of a plasmonic features extending beyond the visible, especially at the higher EPPS concentrations.

Table 4.1 Absorption maximum wavelengths ($\lambda_{max}$) of the primary, secondary, and tertiary plasmon resonance features of gold nanostars synthesized at various EPPS concentrations determined from the zero point crossing value of the first derivative of each spectrum using MathCAD.

| **EPPS concentration (mM)** | **Values of $\lambda_{max}$ (nm) of the plasmon resonance features** | | |
|---|---|---|---|
| | **Primary** | **Secondary** | **Tertiary** |
| 20 | ~550* | 626.0 | - |
| 40 | ~550* | 660.4 | - |
| 50 | ~550* | 674.5 | - |
| 60 | 535.1 | 695.0 | - |
| 80 | 557.0 | 717.7 | ~1000* |
| 100 | 565.0 | 727.9 | 1040.4 |
| 200 | 578.3 | 770.7 | 1133.5 |
| 300 | 577.4 | 767.9 | 1134.9 |
| 400 | 577.5 | 749.8 | 1116.0 |

* Exact values could not be obtained for $\lambda_{max}$ because these peaks appeared as weak shoulders under the strong secondary plasmon resonance absorption features.

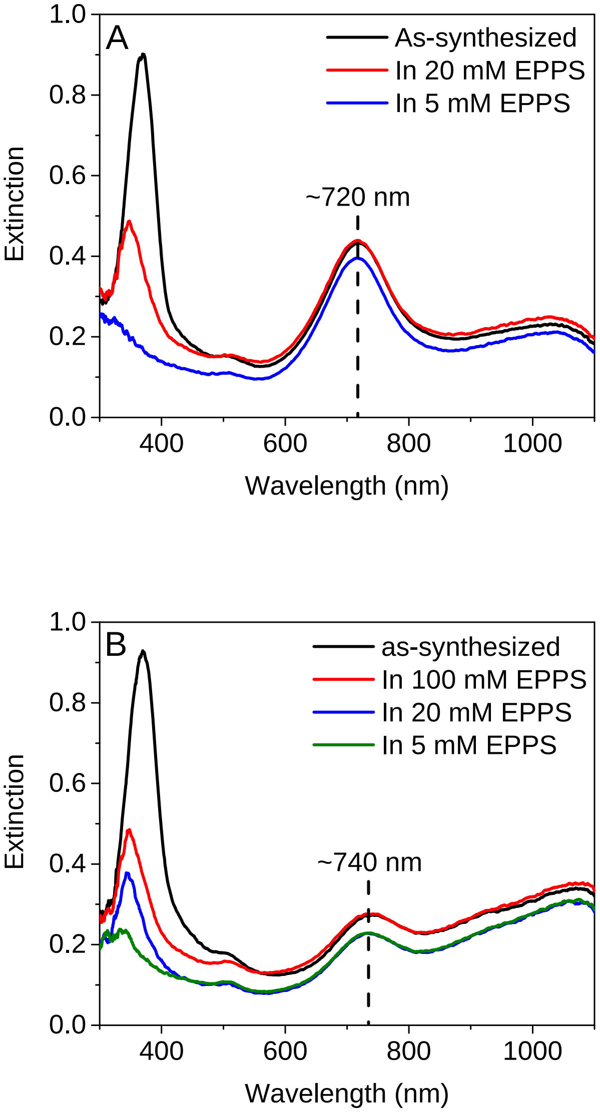

Figure 4.5 LSPR spectra collected before and after each round of centrifugation during the process of decreasing the EPPS concentration in the as-synthesized medium for gold nanostars synthesized at (A) 100 and (B) 400 mM EPPS concentrations with $\lambda_{max}$ centered at ~720 and ~740 nm respectively. Note that the legends on each plot indicate the EPPS concentration used for resuspension after each successive round of centrifugation.

5424). The supernatant was replaced by a lower concentrated EPPS solution as to gradually lower the EPPS concentration in the medium to a final 5 mM concentration. Thus, the bulk EPPS concentrations were reduced consecutively from 100, 20, and 5 mM or 400, 100, 20, and 5 mM for the samples synthesized at initial EPPS concentrations of 100 and 400 mM, respectively.

The LSPR of the samples were monitored after each round of centrifugation to ensure the stability of the samples. The extinction spectra, as indicated in Figure 4.5 suggest that the samples remain stably dispersed after each round of centrifugation with no evidence of structural deformations (as evidenced by the optical properties associated with the stars remaining unchanged). These data also suggest the removal of excess gold salt as evidenced by the reduction of absorbance centered at ~387 nm. In all cases, 10 μL of a diluted nanoparticle solution (20 % mixture in ethanol) was applied to a carbon-formvar coated copper grid (400 mesh, Ted Pella or Electron Microscopy Sciences) and allowed to air dry prior to imaging. The samples were imaged using JEOL JEM-1230 Electron Microscope as shown by the representative TEM images in Figure 4.6. The resulting images were analyzed using Image J Analyzer, and 100 nanoparticles were evaluated per sample.

Similarities and differences between the two samples are noted in the TEM images. First, the number of tips (spikes) on the individual nanostars varied between 3 and 5, while the samples predominantly contained tetrapod nanostructures (i.e., nanostars with 4 spikes per particle). This is consistent with the literature where Good's buffers such as HEPES resulted in predominantly branched tetrapod nanostructures.[179] Second, the nanostars synthesized using 100 mM EPPS exhibited an average largest tip-to-tip distance of 295 ±

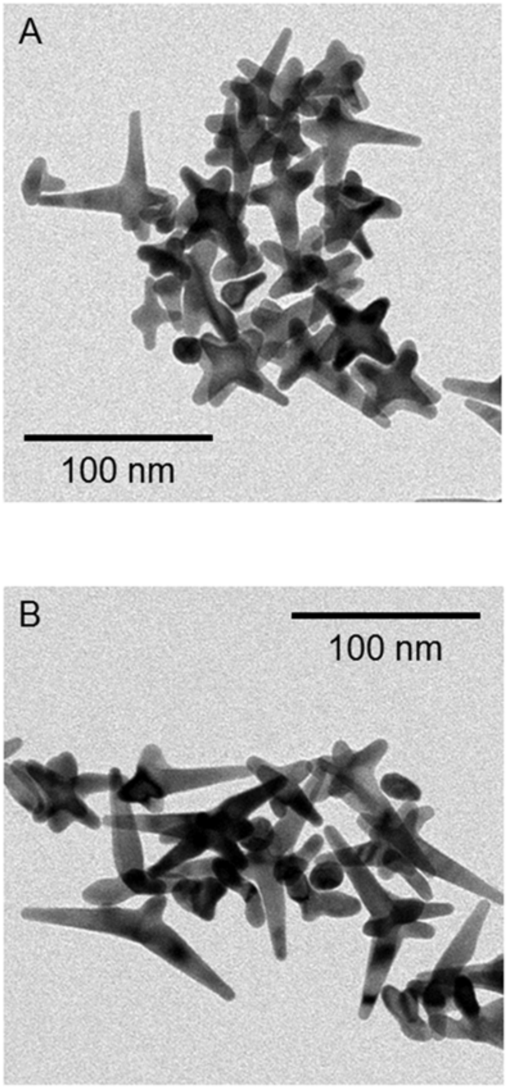

Figure 4.6 TEM images of gold nanostars synthesized at (A) 100 and (B) 400 mM EPPS concentrations. In both samples, the number of tips per nanostars ranged from 3 - 5 while most particles had 4 tips. The largest tip-to-tip distance of the nanostars were 295 ± 112 and 388 ± 200 nm for the nanostars synthesized at 100 and 400 mM EPPS concentrations, respectively. The average tip length in the nanostars were 109 ± 50 and 139 ± 88 nm for the nanostars synthesized at 100 and 400 mM EPPS concentrations respectively (100 nanoparticles were analyzed in each sample).

112 nm, whereas those synthesized at a 400 mM EPPS concentration were significantly larger (388 ± 200 nm). These large standard deviations are attributed to particle heterogeneity as seen in Figure 4.6. As previously noted, the lowest energy visible plasmon features of gold nanostars is associated with the branches with hybridization contributions from the core of the nanostars.[182] Hence, the nanostar branch morphology (length, width, etc.) is important in determining the position of these low energy visible bands in the extinction spectra. Upon analysis of the TEM images, the average branch length of the nanostars synthesized at 100 mM EPPS was 109 ± 50 nm while those synthesized using 400 mM EPPS were 139 ± 88 nm. Thus, these branch length differences can be used to understand the low energy visible plasmon resonance observed for the two nanostar samples. Once again, large standard deviations are observed here as the nanostars are heterogeneous in branch length, where on most particles at least one branch was significantly longer than the others. This is consistent with anisotropic or directional growth of branches during the synthesis of nanostars. Although both TEM analysis and visible extinction spectra indicated material differences, further spectroscopic investigations at the infrared frequencies is warranted in order to obtain a better understanding of the buffer concentration effects on the lowest energy plasmon resonance.

## 4.7 Infrared Optical Properties of Gold Nanostars

Although the visible plasmonic properties of gold nanostars are well-studied, fewer investigations of their infrared plasmon properties have been performed. According to a recent study conducted by Lee and Kwak, discrete dipole approximations of gold nanostars exhibit a primary plasmon resonance at high energies due to the inner core, while secondary and tertiary resonances may also exist as a result of the protruding branches.[193] The secondary resonance is typically a result of the hybridization of the core and the individual branches, while the tertiary resonance results from the coupling between the protruding branch(es).[193] The plasmonic properties of nanostars can be understood in terms of morphology, which consists of spherical as well as elongated (nanorod-like) architectures thus giving rise to multiple plasmon resonance features.

To evaluate these spectral variations, LSPR spectra are collected for the nanostar samples so that optical data ranging from 450 - 1400 nm can be observed. From these spectra, variations in plasmonics of the spherical core and branches can be observed. To investigate the plasmonic variations that extend beyond the visible frequencies, near infrared (NIR) spectra are also collected using a FTIR spectrophotometer (Bruker Tensor 27) configured in transmission geometry and equipped with a NIR light source and a deuterated triglycine sulfate (DGTS) detector. Note that the FTIR sample compartment was modified to hold the polymethyl methacrylate cuvettes used in the extinction measurements to preserve consistency between measurements. All spectra collected using a 5 mm pathlength, and a Nanopure water blank are shown in Figure 4.7. Each pair of visible and NIR spectra were overlapped at 1000 nm. Thus, the NIR spectra were multiplied by a constant to correct for slight pathlength variations and to match the absorbance with the visible spectrum.

Three plasmon features are highlighted from these spectra; (1) a weak primary plasmon feature at wavelengths $< 600$ nm, (2) an intense secondary plasmon feature between 600 - 900 nm, and (3) a broad tertiary plasmon feature at wavelengths $> 900$ nm. The $\lambda_{max}$ values of each of these features for gold nanostars synthesized with various EPPS

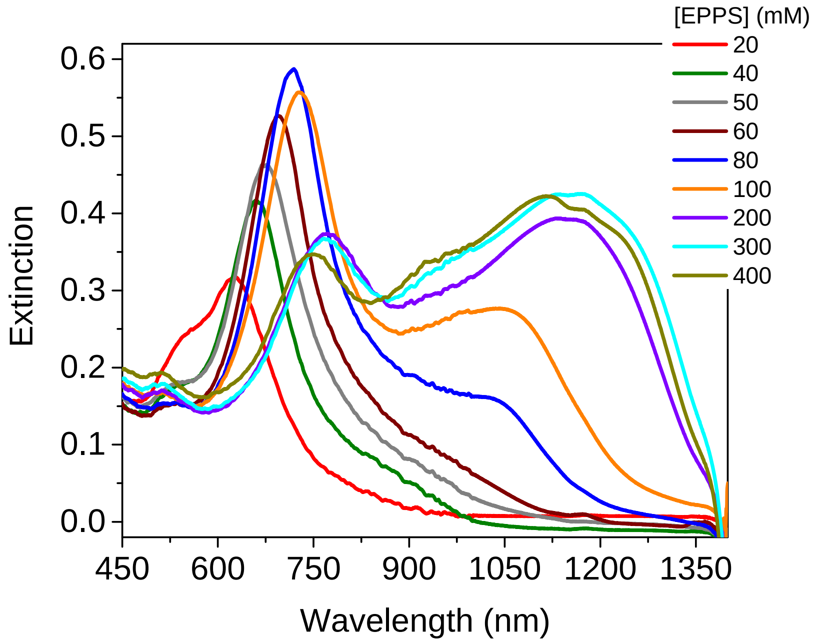

Figure 4.7 Combined visible and NIR spectra of the synthesized gold nanostars. The visible and NIR spectra were collected separately using a 5 mm pathlength and were aligned at 1000 nm. The data beyond 1450 nm is not shown here due to the interference from the strong absorption of infrared radiation by water around this wavelength.

concentrations is summarized in Table 4.1. According to previous analysis conducted by Webb et. al. with gold nanostars synthesized with HEPES, the plasmon features of nanostar structures are explained via a hybridization model where the plasmon properties of the core and the branches are hybridized to produce bonding and anti-bonding plasmonic features.[185] The primary plasmon features are attributed to the anti-bonding plasmon feature, which is primarily contributed by the core plasmons, whereas the secondary plasmon features are predominantly attributed to the bonding plasmon feature, where the predominant contributions are those of branches with a finite contribution from the core.[185] The shoulder or tertiary plasmon feature observed at lower energy arise from the hybridization of the plasmons of multiple branches of a nanostar and imply that this inter-branch hybridization (1) increases the extinction cross-section of the bonding nanostar plasmons due to the admixture of the core plasmons in the bonding plasmon mode, and (2) enhances the dipole moment of the branch plasmons.[185]

Further, the nanostar core behaves as an antenna effectively increasing the near-field enhancements of the bonding plasmons and therefore, as the nanostar branch dimensions (length, width, and density) increase, stronger hybridization occurs between the core and branch plasmons, increasing the energy-level splitting between the bonding and anti-bonding plasmon modes.[185] This enhanced hybridization, thus, gives rise to a red shift in the $\lambda_{max}$ of the secondary (or bonding) plasmon feature as the nanostar branches become larger in dimensions. Here, variations in the branch dimensions are observed by varying the EPPS concentration. The EPPS concentration dependent spectra in Figure 4.7 as well as the corresponding values of $\lambda_{max}$ for the secondary plasmon feature reported in Table 4.1 are therefore consistent with the explanation above.

Interestingly, the NIR spectral features observed for the nanostars was clearly sensitivity to the buffer concentration used during synthesis. Initially, at lower EPPS concentrations, this feature is present as a weak, shoulder on the secondary plasmon. But at high enough EPPS concentrations, the plasmon is shifted into the NIR portion of the spectrum while at the same time increasing its intensity. Note that as a relatively large (5 mm) pathlength was used in collecting the IR spectra, the overtone water band present near 1400 nm (i.e. ~7150 cm$^{-1}$) interfered in observing any residual plasmonic behavior beyond this wavelength.

Structural anisotropy or the breach in structural symmetry of nanostars is known to result in higher order plasmon features as well as to enhance the intensity of the dark modes.[194] The tertiary plasmon feature described above, therefore, can be attributed to non-symmetric gold nanostars synthesized here (*vide supra*). Further, the non-symmetry of the synthesized nanostars were more apparent at the higher 400 mm EPPS concentration compared to the lower 100 mM concentration. Increase in intensity of the tertiary plasmon feature observed here as the buffer concentration increased is hence consistent with the concentration dependent structural anisotropy of the synthesized gold nanostars.

Many nanoscale architectures of gold are known to exhibit plasmonic features in the visible wavelengths while being well-dispersed in solution. However, architectures that exhibit plasmonic behavior that extends into the infrared wavelengths while being well dispersed in solution is scarce to date. Interestingly, the outlined synthesis provides a straightforward and simple procedure to synthesize gold nanostructures with NIR plasmonic character that can be stably dispersed in solution. Further, these plasmons can be easily tuned by the simple variation of the buffer concentration used in synthesis.

Notably, the plasmonic features extended into the NIR, while indicating broad resonances especially for the larger (> 100 mM) EPPS concentrations.

## 4.8 Summary, Conclusions and Future Direction

Herein, a seedless, one-step synthesis of gold nanostars was demonstrated with tunable plasmon resonances via the simple variation of buffer concentration used during synthesis. The EPPS buffer plays multiple roles during the synthesis, by simultaneously serving as the reducing agent for gold as well as a template for directing anisotropic growth of the nanoparticles. Hence, the optical properties and morphology variations of the nanostars were conducted to understand variations caused by the buffer used during synthesis. Good correlation between the nanostar morphology and optical properties are observed, both of which change consistently with varying EPPS concentration.

Plasmonic tunability is an important consideration for nanomaterial synthesis in the many applications where the optical properties of the nanomaterials are imperative. For instance, plasmonic materials with resonances at or near the excitation wavelength is believed to be desirable for SERS applications. Importantly, plasmonic material with absorption properties extending into the infrared have the potential applicability in SEIRA. Thus, the outlined procedure for the synthesis of gold nanostars with plasmons extending into the NIR will be important in the rational design, synthesis, and applications of gold nanostars in novel surface enhanced spectroscopies.

The outlined synthesis was simple, and straightforward, especially in contrast to typical nanomaterial synthetic procedures where many parameters including temperature, reaction time, and the addition rates are extensively controlled during synthesis. However, a drawback to the lack of controls is the reproducibility of the resulting material. Hence, detailed investigations of the many variables that may alter the properties of the nanomaterials synthesized here, for example temperature, pH of the medium, ionic strength etc. should be extensively studied if more precise control of nanoparticle properties are desired.

Another potential future direction is to investigate the applicability of these nanomaterials in various nanotechnology applications. For instance, the gold nanostars synthesized here at EPPS concentrations exceeding 200 mM indicate a broad plasmon centered at ~760 nm. These particles, therefore, indicate promising potential as SERS substrates where a typical excitation wavelength of 785 nm can be successfully used in observing a SERS signal. Further, with the synthesized nanomaterials clearly exhibiting broad NIR plasmonic behavior, they are likely to be ideal candidates in observing a SEIRA signal via a suitably bound infrared chromophore. Importantly, in addition to the above plasmon tunability, the significant solution-phase stability and the tolerance to high ionic strength as observed with these gold nanostars are likely to produce an ideal system for future SEIRA investigations.

# CHAPTER 5

# CONCLUSIONS AND FUTURE DIRECTION

The scope of the material discussed herein can be broadly categorized as being focused on achieving three distinct objectives: (1) refining the accuracy and predictability of functionalized nanoparticle stability via proposing apt improvements in parametrization to the well-known xDLVO theory, (2) investigations of the ability of gold nanospheres in producing surface-enhanced infrared absorption via a suitably bound chromophore, and (3) the development of a straightforward and simple procedure to synthesize gold nanostructures with plasmonic character extending into the infrared wavelengths. The individual objectives were dealt with in detail in the preceding chapters, however, the overall objective of this work is the development of a model system for the observation of a surface-enhancement using solution-phase nanoparticles with applications in SEIRA and SE-2D IR spectroscopies.

It is important to note that all objectives stated above represent initial steps in attaining this ultimate objective. First, an increased comprehension of nanostructure stability and the ensuing physical and chemical properties was achieved via xDLVO modelling. Then, a better understanding of the nanoparticle morphology as well as the nanoparticle-solution interface in spectroscopic applications of nanomaterials of various morphology was achieved in the eventual investigations, with emphasis on the many factors that are essential considerations for solution-phase SEIRA spectroscopy. Hence, the overall comprehension achieved here is imperative in allowing an ideal system to be designed, developed, and applied in observing a competent infrared surface enhancement.

The xDLVO improvements were developed for functionalized, spherical gold nanoparticles. Nevertheless, we have come to the understanding that nanomaterials of spherical morphology are not robust SEIRA substrates, thereby requiring more complicated morphological forms to be utilized. Hence, a possible future direction is to investigate ways of adopting the DLVO framework with complicated, non-spherical morphologies. This has previously been done in terms of widely used nanoparticle morphologies such as nanotubes.[77,195] However, close attention to the intricate details of calculating the individual interaction potentials is required if this model is to be adopted for complicated morphologies such as nanostars, nanorods, tetrapods, etc.

Second, a significant parametrization modification was conducted by the incorporation of a size-dependent Hamaker constant in calculating the van der Waals interactions. Many assumptions, however, were incorporated due to the limited availability of simple models explaining the size-dependent dielectric properties of a metal. Hence, further modifications are required in order to increase the accuracy of the calculated size-dependent Hamaker constant values of gold nanoparticles. This, in turn, would be of widespread interest to many nanotechnology applications as van der Waals interactions often dominate nanoparticle interactions, thereby allowing nanoparticle stability to be easily predicted or even controlled, via the accurate knowledge of these interactions, resulting from better estimations of the Hamaker constant.

Third, in the detailed investigations of the ability of gold nanospheres in producing a surface enhancement, direct evidence of SEIRA was revealed in the IR spectra of $SCN^-$ with 1st generation gold nanospheres. This was via the combination of the shifted frequency and the anomalous lineshape observed in these experiments. However, the spectra obtained here do not allow us to separately quantify the absorptive and dispersive lineshape contributions to the total signal. In turn, knowledge on these relative contributions would allow us to obtain a better understanding of the enhancement mechanism, while at the same time allowing quantification of the enhancement. Hence, further experiments that investigate this anomalous lineshape are important. For example, the spectra reported were collected for samples where both free and surface-bound $SCN^-$ was present, and gave rise to the observed lineshape. If spectra could be collected after the removal of the free analyte in the system thereby eliminating the absorptive contributions from the free analyte, the enhanced (surface-bound) signal could be easily isolated, allowing more in-depth analysis.

Forth, it is clear that non-spherical geometries of nanostructures are more efficient for IR plasmonic applications as they are well-known to exhibit plasmonic features in the IR wavelengths, however, a problem that needs to be addressed is the solution-phase stability of such plasmonic nanostructures. A straightforward and simple procedure was developed to synthesize gold nanostructures with plasmonic character clearly extending into the infrared wavelengths was presented. Regardless of their dimensions, these nanoparticles were stably suspended in solution for at least few weeks and could withstand high ionic strengths, both of which are in favor of solution-phase SEIRA applications. Importantly, the plasmon resonances of the synthesized nanostars could be easily tuned by simple variation of the buffer concentration used during the synthesis and could be exploited in applications.

With the successful synthesis of IR plasmonic nanomaterials, the next step would be to utilize these structures in various forms of surface enhanced spectroscopies. According to previous reports, gold nanostars have produced SERS enhancements as high as $10^7$ from individual nanostars, without the need to form hotspots in the junctions between aggregated particles or resonance Raman effects.[191] The gold nanostars synthesized here could be used in SERS experiments thus allowing a better understanding of these structures as potential surface enhanced spectroscopy substrates. These experiments could be also extended to SEIRA experiments where the IR plasmon resonance features of the gold nanostars might contribute to surface enhancements.

Finally, the systems developed for observing a SEIRA signal can be used in SE-2D IR experiments, whereby the enhancements can be quantified more accurately, allowing for a better understanding of surface enhancement mechanisms to be learned. More importantly, the successful application of a model SEIRA system in SE-2D IR could be followed by the incorporation of these nanostructures into the many scientifically relevant systems, where measuring a 2D IR signal is difficult owing to low signal intensity. Fortunately, the SEIRA enhancements are more significant for SE-2D IR, and hence even a modest enhancement in SEIRA could be followed by a substantial enhancement being observed in SE-2D IR spectroscopy, thereby allowing widespread applicability of the infrared surface enhancement phenomena.

# APPENDIX A

# CALCULATION OF SUPPLEMENTARY VARIABLES FOR XDLVO MODELLING OF NANOPARTICLE STABILITY

**Inverse Debye Length.** The inverse Debye length ($\kappa$) of a system is calculated as follows:

$$\kappa = \left( \frac{e^2}{\varepsilon_0 \varepsilon_r k_B T} \sum_{i=1}^{N} z_i^2 n_i \right)^{\frac{1}{2}} \tag{A1}$$

where $e$ is the elementary electric charge, $\varepsilon_0$ is the permittivity of vacuum, $\varepsilon_r$ is relative permittivity of the solution, and $z_i$ and $n_i$ are the charge and number concentration of each ionic species in solution, respectively. (oshima Effective Surface Potential and Double-Layer Interaction of Colloidal Particles 1995)

**Volume Fraction of a Ligand.** The volume fraction of a ligand ($\phi_p$) is determined by the following relationship;

$$\phi_p = \frac{3\Gamma_{\max} a^2}{\rho_d \left( (t+a)^3 - a^3 \right)} \tag{A2}$$

where $\rho_d$ is the density of the (pure) SAM ligand, and $\Gamma_{\max}$ is the surface density in units of ligand mass per nanoparticle surface area estimated from X-ray photoelectron spectroscopy.[1]

# APPENDIX B

# THEORETICAL FRAMEWORK FOR DETERMINING THE SIZE-DEPENDENT HAMAKER CONSTANTS OF SPHERICAL GOLD NANOPARTICLES

**Size-Dependent Imaginary Dielectric Permittivity Calculations and the Hamaker Constant.** According to Lifshitz theory, the Hamaker constant is calculated as follows

$$A_{NP-Medium-NP} = \frac{3}{4\pi}\hbar\omega_{NP-Medium-NP} \tag{B1}$$

where $\omega_{NP\text{-}Medium\text{-}NP}$ is the Lifshitz constant defined as

$$\omega_{NP-Medium-NP} = \int_0^\infty \left(1 - \frac{2\varepsilon_M(i\omega)}{\varepsilon_{NP}(i\omega) + \varepsilon_M(i\omega)}\right)^2 d\omega \tag{B2}$$

Here, $\varepsilon_{NP}(i\omega)$ and $\varepsilon_M(i\omega)$ are the dielectric permittivity of the metal (nanoparticle) and of the medium as a function of the imaginary frequency iω, respectively. The values of $\varepsilon_{NP}(i\omega)$ and $\varepsilon_M(i\omega)$ can be calculated using the imaginary component of the dielectric constant of the material (Im $\varepsilon_{NP}(x)$) as follows

$$\varepsilon_n(i\omega) = 1 + \frac{2}{\pi}\int_0^\infty \frac{x\,\mathrm{Im}\,\varepsilon_n(x)}{x^2+\omega^2}dx \tag{B3}$$

The imaginary part of the bulk dielectric permittivity can be measured experimentally, but it must be corrected to account for size dependence. As the nanosphere diameter decreases, the fraction of surface atoms with dangling bonds increases and electron confinement leads to discrete electronic densities of states. Collectively, these effects cause the dielectric properties of nanoparticles to deviate significantly from those of the bulk.[112] To account for the size dependence of the imaginary dielectric permittivity for a metal nanoparticle, a correction term as a function of frequency (ω) and nanoparticle radius (a) can be calculated using the expression

$$\Delta\left(\mathrm{Im}\,\varepsilon\left(\omega,a\right)\right)=\frac{\omega_P^2}{\omega^3}\left\{\gamma\left(a\right)-\gamma\right\} \tag{B4}$$

where $\omega_P$ is the plasma frequency ($5.8 \times 10^{15}$ s$^{-1}$), γ is the electron scattering rate (0.01 $\omega_P$), and γ(R) is the size-dependent electron scattering rate, which can be calculated as follows

$$\gamma\left(a\right)=\gamma+C\frac{v_F}{a} \tag{B5}$$

Here, $V_F$ is the Fermi velocity ($1.39 \times 10^6$ ms$^{-1}$) and and C is a dimensionless constant that accounts for the chemical composition and the size-dependent mean free path that leads to size-dependent electron scattering of the material, respectively.[196,197] The constant C in these calculations is taken to be 1 for gold, assuming the angular dependence of the scattering of each electron to be isotropic. Now, the size corrected dielectric permittivity of the metal can be calculated by adding the size-dependent correction to the imaginary dielectric permittivity (Δ(Imε(ω,a))) to the experimentally measured bulk value of the imaginary dielectric permittivity at each wavelength. These size-corrected values can then be used to determine the Hamaker constant using equations B1-B3 where we approximate the integrals as discrete summations that run over the full range of the experimental data.

# APPENDIX C

## SUPPLEMENTARY CHARACTERIZATION OF THE SYNTHESIS PRODUCT *P*-AZIDOTHIOPHENOL

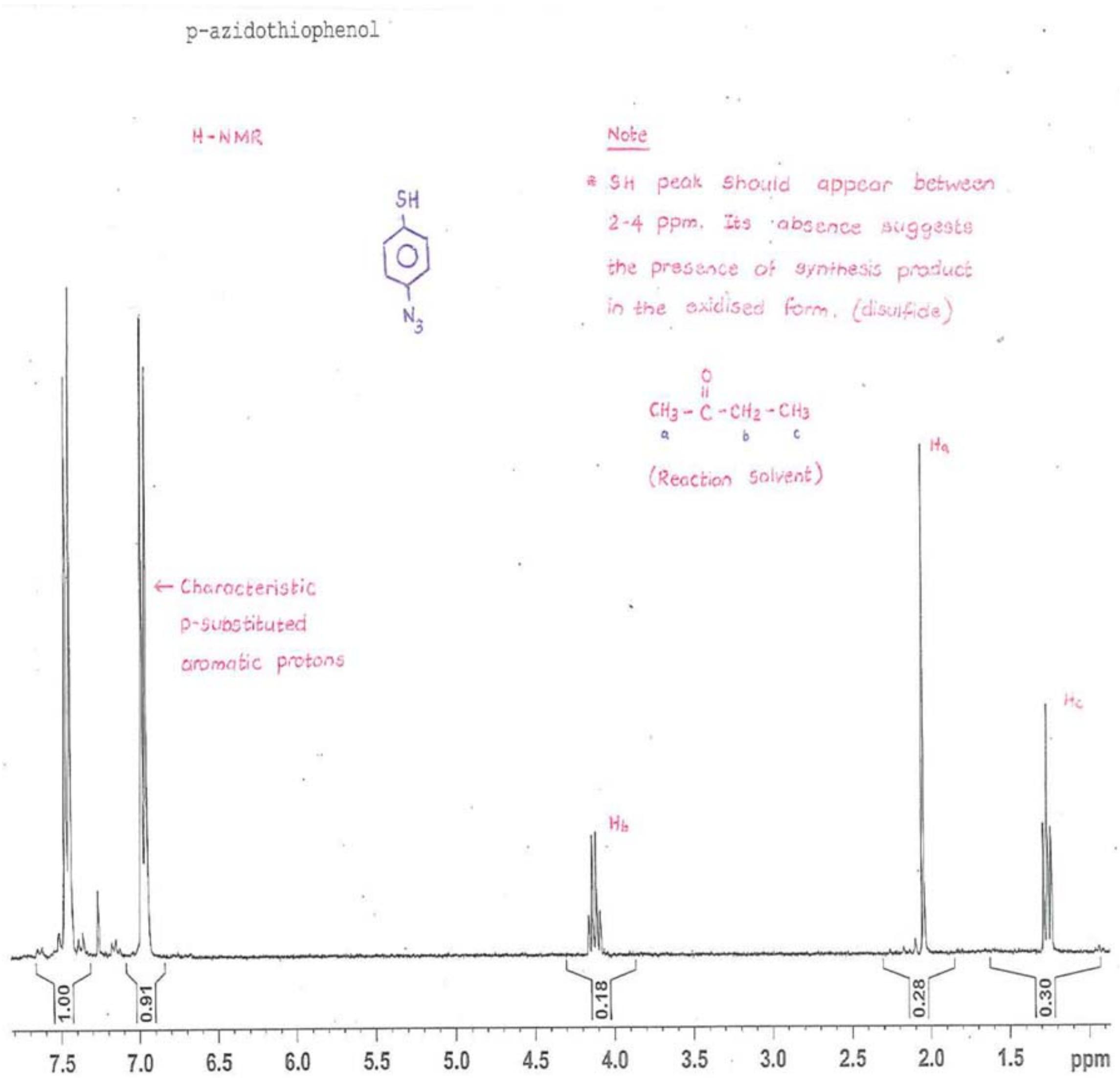

Note

* SH peak should appear between 2-4 ppm. Its absence suggests the presence of synthesis product in the oxidised form. (disulfide)

(Reaction solvent)

← Characteristic p-substituted aromatic protons

Figure C.1 $^1$H-NMR spectrum of the synthesis product, *p*-Azidothiophenol

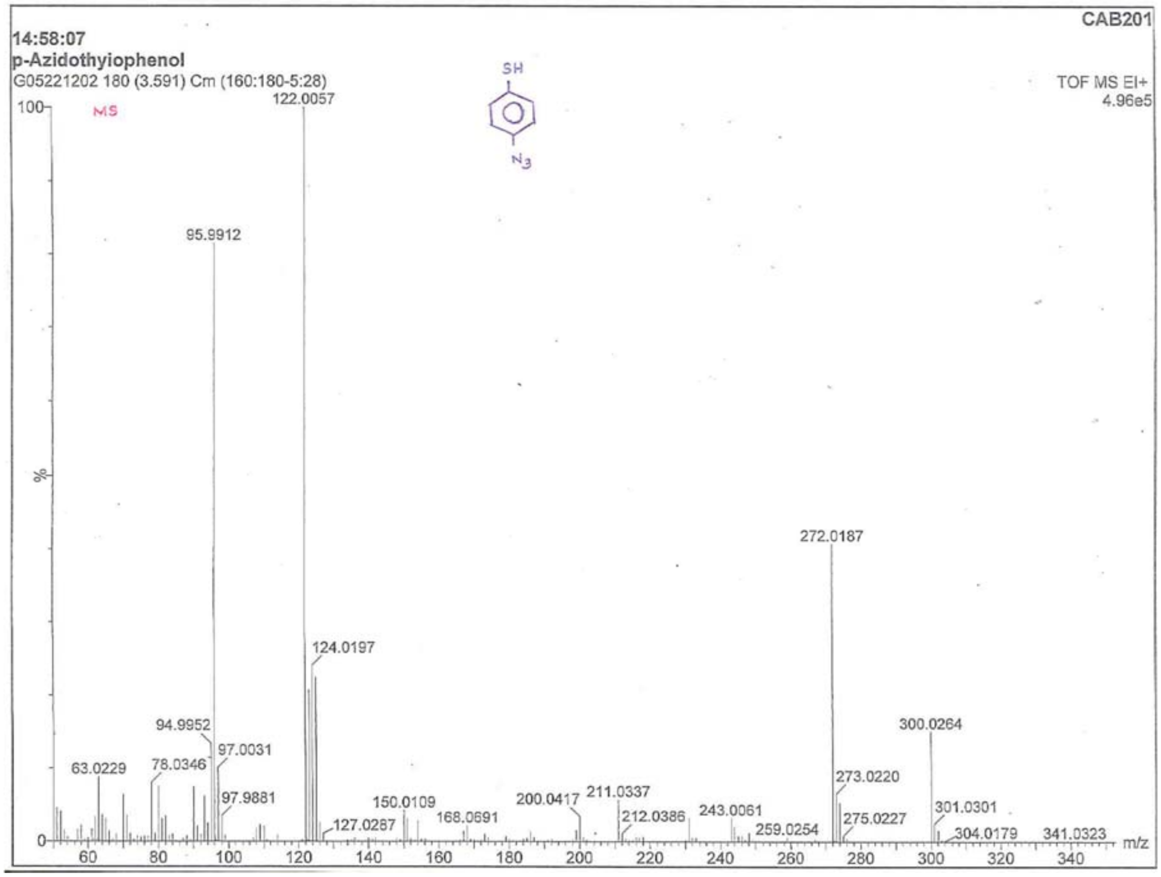

Figure C.2 Mass spectrum of the synthesis product, *p*-Azidothiophenol

# APPENDIX D

# MATLAB FUNCTION FOR THE DETERMINATION OF INTERACTION PAIR POTENTIALS OF NANOPARTICLES VIA THE XDLVO THEORY

```
function XDLVO

%     This function calculates and plots the interaction potential
      between 2 NPs of specified radius a (nm) as a function for
      separation distance (nm), using the extended-DLVO theory. The other
      parameters of the system can be changed from within the code.
      Compiled by Lahiru Wijenayaka on 28.04.14 (Last modified on
      11.25.14)

% Constants
E0=8.854E-12;           % F/m
kB=1.381E-23;           % J/K
e=1.602E-19;            % C
Na=6.022E23;            % /mol

% System parameters
T=298.15;               % K
Er=78.4;                % unitless
a=6.5;                  % Nanoparticle radius (nm
A=3.7E-19;              % Hamaker constant
I=63;                   % mM (same as mol/m3)
ZP=-20.9;               % mV
```

```
% SAM parameters
MW=148.22;                % Molecular weight of ligand (g/mol)
d=1.087;                  % Density of ligand (g/cm3) in pure form
l=1.13;                   % Molecule length (nm)
Pd=4.58E14;               % SAM packing density (molecules/cm2)
Theta=39;                 % Tilt angle (degrees)

% Solvent parameters
MWs=18.01528;             % Molecular weight of solvent (g/mol)
ds=1000000;               % Density of solvent molecules (g/m3)
X=0.45;                   % Flory Huggins solvency parameter

% Calculation of parameters
      s=[0.001:0.01:10];
      % Separation distances in nm
      K=(((2*Na*e*e*I)/(E0*Er*kB*T))^0.5)*(1E-9);
      % Inverse Debye length in nm-1
      t=l*cos(Theta*(pi/180));
      % SAM thickness (nm)
      Psi0=(ZP*0.001)*(1+(1/(K*a)))*exp(1);
      % Surface potential in V
      Y=(8*tanh((e*Psi0)/(4*kB*T)))/(1+((1-
      (((2*K*a)+1)/(((K*a)+1)^2)*((tanh((e*Psi0)/(4*kB*T)))^2)))^0.5));
      % Factor required to calculate Vele
      C=(1000*10000*Pd*MW)/Na;
      % Surface concentration of SAM (mg/m2)
      VF=(3*C*a*a)/(d*(((t+a)^3)-(a^3)));
      % Volume fraction of SAM (unitless)
```

```
        MVs=MWs/ds;
        % Molar volume of solvent (m3/mol)

  % Calculation of potentials
       % Van der Waals
             Vvdw=-
             (A/(6*kB*T))*(((2*a*a)./(((4*a)+s).*s))+((2*a*a)./(((2*a)+s
             ).^2))+log((((4*a)+s).*s)./(((2*a)+s).^2)));
             % Van der Waals potential (/kT)

      % Electrostaic
          if (K*a)<5
             Vele=((4*pi*E0*Er*a*a*(1E-18)*Y*Y*kB*T)/(e*e)).*((exp(-
             K.*s))./((s+(2*a))*(1E-9)));
             % Electrostatic potential at Ka<5 (/kT)
          else
             Vele=((2*pi*E0*Er)/(kB*T))*(Psi0^2)*(a*(1E-9))*log(1+exp(-
             K.*s));
             % Electrostatic potential at Ka>5 (/kT)
          end

      % Osmotic
           for i=1:length(s);
          if s(i)<t;
             Vosm(i)=(((4*pi*Na*a*(1E-9)*VF*VF*t*t*(1E-18))/(MVs))*(0.5-
             X)).*((s(i)./(2*t))-(1/4)-log(s(i)./t));
             % Osmotic potential at s<t (/kT)
          elseif s(i)<(2*t);
```

```
        Vosm(i)=(((4*pi*Na*a*(1E-9)*VF*VF)/(MVs))*(0.5-X)).*((t-
        (s(i)./2))^2).*(1E-18);
        % Osmotic potential at t=<s<2t (/kT)
    else
        Vosm(i)=0;
        % Osmotic potential at s>=2t (/kT)
    end
end

% Elastic
for i=1:length(s);
    if s(i)<t;
        Vela(i)=((2*pi*Na*a*(1E-9)*VF*t*t*(1E-
        18)*d*(1E6))/(MW)).*(((s(i)./t).*log((s(i)./t).*(((3-
        (s(i)./t))./2).^2)))-(6.*log((3-(s(i)./t))./2))+(3.*(1-
        (s(i)./t))));
        % Elastic potential at s<t (/kT)
    else
        Vela(i)=0;
        % Elastic potential at s>=t (/kT)
    end
end

% Total interaction potential (/kT)
        Vt=Vvdw+Vele+Vosm+Vela;
```

```
% Plotting the output

      p=plot (s,Vvdw,'b--',s,Vele,'k--',s,Vosm,'g--',s,Vela,'m--
      ',s,Vt,'r',s,0,'k');

      set(p(5),'linewidth',1.5)

      xlim([0 10])

      ylim([-20 30])

      xlabel('Separation distance (nm)')

      ylabel('Potential/kT (unitless)')

      legend('Van der
      Walls','Electrostatic','Osmotic','Elastic','Total');


% Saving the output in txt format

      A=[s; Vvdw; Vele; Vosm; Vela; Vt];

      fileID = fopen('Au@MHA.txt','w');

      fprintf(fileID,'%7s %12s %13s %11s %14s
      %10s\n','s(nm)','Vvdw(/kT)','Vele(/kT)','Vosm(/kT)','Vela(/kT)','
      Vt(/kT)');

      fprintf(fileID,'%6f %12f %12f %12f %12f %12f\n',A);

      fclose(fileID);

end
```

# APPENDIX E

## MATLAB BASED GUI FOR THE DETERMINATION OF INTERACTION PAIR POTENTIALS OF NANOPARTICLES VIA THE XDLVO THEORY

```
function varargout = XDLVO_GUI(varargin)

%     XDLVO_GUI MATLAB code for XDLVO_GUI.fig
%     This GUI calculates and plots the interaction potential between 2
      NPs of specified radius a (nm) as a function of separation distance
      nm), using the extended-DLVO theory
%     Last Modified by GUIDE v2.5 25-Nov-2014 10:33:50
%     Compiled by Lahiru Wijenayaka on 11.24.14 (Last modified on
      12.05.14)

% Begin initialization code
gui_Singleton = 1;
gui_State = struct('gui_Name',       mfilename, ...
                   'gui_Singleton',  gui_Singleton, ...
                   'gui_OpeningFcn', @XDLVO_GUI_OpeningFcn, ...
                   'gui_OutputFcn',  @XDLVO_GUI_OutputFcn, ...
                   'gui_LayoutFcn',  [] , ...
                   'gui_Callback',   []);
if nargin && ischar(varargin{1})
    gui_State.gui_Callback = str2func(varargin{1});
end
if nargout
    [varargout{1:nargout}] = gui_mainfcn(gui_State, varargin{:});
```

```
else
    gui_mainfcn(gui_State, varargin{:});
end
% End initialization code

function XDLVO_GUI_OpeningFcn(hObject, eventdata, handles, varargin)
handles.output = hObject;
% Update handles structure
guidata(hObject, handles);
function varargout = XDLVO_GUI_OutputFcn(hObject, eventdata, handles)
varargout{1} = handles.output;

function IS_Callback(hObject, eventdata, handles)
IS = str2double(get(hObject, 'String'));
if isnan(IS)
    set(hObject, 'String', 0);
    errordlg('Input must be a number','Error');
end
handles.metricdata.IS = IS;
guidata(hObject,handles)
function IS_CreateFcn(hObject, eventdata, handles)
if ispc && isequal(get(hObject,'BackgroundColor'),
get(0,'defaultUicontrolBackgroundColor'))
    set(hObject,'BackgroundColor','white');
end

function Zeta_Callback(hObject, eventdata, handles)
Zeta = str2double(get(hObject, 'String'));
```

```
if isnan(Zeta)

    set(hObject, 'String', 0);

    errordlg('Input must be a number','Error');

end

handles.metricdata.Zeta = Zeta;

guidata(hObject,handles)

function Zeta_CreateFcn(hObject, eventdata, handles)

if ispc && isequal(get(hObject,'BackgroundColor'),

get(0,'defaultUicontrolBackgroundColor'))

    set(hObject,'BackgroundColor','white');

end

function Hamaker_Callback(hObject, eventdata, handles)

Hamaker = str2double(get(hObject, 'String'));

if isnan(Hamaker)

    set(hObject, 'String', 0);

    errordlg('Input must be a number','Error');

end

handles.metricdata.Hamaker = Hamaker;

guidata(hObject,handles)

function Hamaker_CreateFcn(hObject, eventdata, handles)

if ispc && isequal(get(hObject,'BackgroundColor'),

get(0,'defaultUicontrolBackgroundColor'))

    set(hObject,'BackgroundColor','white');

end


function Radius_Callback(hObject, eventdata, handles)

Radius = str2double(get(hObject, 'String'));

if isnan(Radius)
```

```
    set(hObject, 'String', 0);
    errordlg('Input must be a number','Error');
end
handles.metricdata.Radius = Radius;
guidata(hObject,handles)
function Radius_CreateFcn(hObject, eventdata, handles)
if ispc && isequal(get(hObject,'BackgroundColor'),
get(0,'defaultUicontrolBackgroundColor'))
    set(hObject,'BackgroundColor','white');
end

function LMW_Callback(hObject, eventdata, handles)
LMW = str2double(get(hObject, 'String'));
if isnan(LMW)
    set(hObject, 'String', 0);
    errordlg('Input must be a number','Error');
end
handles.metricdata.LMW = LMW;
guidata(hObject,handles)
function LMW_CreateFcn(hObject, eventdata, handles)
if ispc && isequal(get(hObject,'BackgroundColor'),
get(0,'defaultUicontrolBackgroundColor'))
    set(hObject,'BackgroundColor','white');
end

function LD_Callback(hObject, eventdata, handles)
LD = str2double(get(hObject, 'String'));
if isnan(LD)
```

```
    set(hObject, 'String', 0);
    errordlg('Input must be a number','Error');
end
handles.metricdata.LD = LD;
guidata(hObject,handles)
function LD_CreateFcn(hObject, eventdata, handles)
if ispc && isequal(get(hObject,'BackgroundColor'),
get(0,'defaultUicontrolBackgroundColor'))
    set(hObject,'BackgroundColor','white');
end

function LL_Callback(hObject, eventdata, handles)
LL = str2double(get(hObject, 'String'));
if isnan(LL)
    set(hObject, 'String', 0);
    errordlg('Input must be a number','Error');
end
handles.metricdata.LL = LL;
guidata(hObject,handles)
function LL_CreateFcn(hObject, eventdata, handles)
if ispc && isequal(get(hObject,'BackgroundColor'),
get(0,'defaultUicontrolBackgroundColor'))
    set(hObject,'BackgroundColor','white');
end
function SAMD_Callback(hObject, eventdata, handles)
SAMD = str2double(get(hObject, 'String'));
if isnan(SAMD)
    set(hObject, 'String', 0);
```

```
    errordlg('Input must be a number','Error');
end
handles.metricdata.SAMD = SAMD;
guidata(hObject,handles)
function SAMD_CreateFcn(hObject, eventdata, handles)
if ispc && isequal(get(hObject,'BackgroundColor'),
get(0,'defaultUicontrolBackgroundColor'))
    set(hObject,'BackgroundColor','white');
end

function Tilt_Callback(hObject, eventdata, handles)
Tilt = str2double(get(hObject, 'String'));
if isnan(Tilt)
    set(hObject, 'String', 0);
    errordlg('Input must be a number','Error');
end
handles.metricdata.Tilt = Tilt;
guidata(hObject,handles)
function Tilt_CreateFcn(hObject, eventdata, handles)
if ispc && isequal(get(hObject,'BackgroundColor'),
get(0,'defaultUicontrolBackgroundColor'))
    set(hObject,'BackgroundColor','white');
end

function Temp_Callback(hObject, eventdata, handles)
Temp = str2double(get(hObject, 'String'));
if isnan(Temp)
    set(hObject, 'String', 0);
```

```
    errordlg('Input must be a number','Error');
end
handles.metricdata.Temp = Temp;
guidata(hObject,handles)
function Temp_CreateFcn(hObject, eventdata, handles)
if ispc && isequal(get(hObject,'BackgroundColor'),
get(0,'defaultUicontrolBackgroundColor'))
    set(hObject,'BackgroundColor','white');
end
function Perm_Callback(hObject, eventdata, handles)
Perm = str2double(get(hObject, 'String'));
if isnan(Perm)
    set(hObject, 'String', 0);
    errordlg('Input must be a number','Error');
end
handles.metricdata.Perm = Perm;
guidata(hObject,handles)
function Perm_CreateFcn(hObject, eventdata, handles)
if ispc && isequal(get(hObject,'BackgroundColor'),
get(0,'defaultUicontrolBackgroundColor'))
    set(hObject,'BackgroundColor','white');
end

function SMW_Callback(hObject, eventdata, handles)
SMW = str2double(get(hObject, 'String'));
if isnan(SMW)
    set(hObject, 'String', 0);
    errordlg('Input must be a number','Error');
```

```
end
handles.metricdata.SMW = SMW;
guidata(hObject,handles)
function SMW_CreateFcn(hObject, eventdata, handles)
if ispc && isequal(get(hObject,'BackgroundColor'),
get(0,'defaultUicontrolBackgroundColor'))
    set(hObject,'BackgroundColor','white');
end

function SD_Callback(hObject, eventdata, handles)
SD = str2double(get(hObject, 'String'));
if isnan(SD)
    set(hObject, 'String', 0);
    errordlg('Input must be a number','Error');
end
handles.metricdata.SD = SD;
guidata(hObject,handles)
function SD_CreateFcn(hObject, eventdata, handles)
if ispc && isequal(get(hObject,'BackgroundColor'),
get(0,'defaultUicontrolBackgroundColor'))
    set(hObject,'BackgroundColor','white');
end

function FH_Callback(hObject, eventdata, handles)
FH = str2double(get(hObject, 'String'));
if isnan(FH)
    set(hObject, 'String', 0);
    errordlg('Input must be a number','Error');
```

```
end
handles.metricdata.FH = FH;
guidata(hObject,handles)
function FH_CreateFcn(hObject, eventdata, handles)

if ispc && isequal(get(hObject,'BackgroundColor'),
get(0,'defaultUicontrolBackgroundColor'))
    set(hObject,'BackgroundColor','white');
end

% --- Executes on button press in Calculate.
function Calculate_Callback(hObject, eventdata, handles)

% Constants
      E0=8.854E-12;           % F/m
      kB=1.381E-23;           % J/K
      e=1.602E-19;            % C
      Na=6.022E23;            % /mol

% Nanoparticle parameters
      a=handles.metricdata.Radius;    % Nanoparticle radius (nm
      A=handles.metricdata.Hamaker;   % J
      ZP=handles.metricdata.Zeta;     % mV
      I=handles.metricdata.IS;        % mM (same as mol/m3)

% System parameters
      T=handles.metricdata.Temp;      % K
      Er=handles.metricdata.Perm;     % unitless
```

```
      MWs=handles.metricdata.SMW;

      % Molecular weight of solvent (g/mol)

      ds=(handles.metricdata.SD)*(1e6);

      % Density of solvent molecules (g/cm3)

      X=handles.metricdata.FH;

      % Flory Huggins solvency parameter (unitless)


% Ligand parameters

      MW=handles.metricdata.LMW;

      % Molecular weight of ligand (g/mol)

      d=handles.metricdata.LD;

      % Density of ligand (g/cm3) in pure form

      l=handles.metricdata.LL;

      % Molecule length (nm)

      Pd=handles.metricdata.SAMD;

      % SAM packing density (molecules/cm2)

      Theta=handles.metricdata.Tilt;

      % Tilt angle (degrees)


% Calculation of parameters

      s=[0.001:0.01:10];

      % Separation distances in nm


      K=(((2*Na*e*e*I)/(E0*Er*kB*T))^0.5)*(1E-9);

      % Inverse Debye length in nm-1

      t=l*cos(Theta*(pi/180));

      % SAM thickness (nm)
```

```
      Psi0=(ZP*0.001)*(1+(1/(K*a)))*exp(1);
      % Surface potential in V
      Y=(8*tanh((e*Psi0)/(4*kB*T)))/(1+((1-
      (((2*K*a)+1)/(((K*a)+1)^2)*((tanh((e*Psi0)/(4*kB*T)))^2)))^0.5));
      % Factor required to calculate Vele
      C=(1000*10000*Pd*MW)/Na;
      % Surface concentration of SAM (mg/m2)
      VF=(3*C*a*a)/(d*(((t+a)^3)-(a^3)));
      % Volume fraction of SAM (unitless)
      MVs=MWs/ds;
      % Molar volume of solvent (m3/mol)

% Calculation of potentials
     % Van der Waals
      Vvdw=-
      (A/(6*kB*T))*(((2*a*a)./(((4*a)+s).*s))+((2*a*a)./(((2*a)+s).^2))
      +log((((4*a)+s).*s)./(((2*a)+s).^2)));
      % Van der Waals potential (/kT)
    % Electrostaic
        if (K*a)<5
            Vele=((4*pi*E0*Er*a*a*(1E-18)*Y*Y*kB*T)/(e*e)).*((exp(-
            K.*s))./((s+(2*a))*(1E-9)));
            % Electrostatic potential at Ka<5 (/kT)
        else
            Vele=((2*pi*E0*Er)/(kB*T))*(Psi0^2)*(a*(1E-9))*log(1+exp(-
            K.*s));
            % Electrostatic potential at Ka>5 (/kT)
        end
```

```
% Osmotic
 for i=1:length(s);
    if s(i)<t;
        Vosm(i)=(((4*pi*Na*a*(1E-9)*VF*VF*t*t*(1E-18))/(MVs))*(0.5-
        X)).*((s(i)./(2*t))-(1/4)-log(s(i)./t));
        % Osmotic potential at s<t (/kT)
    elseif s(i)<(2*t);
        Vosm(i)=(((4*pi*Na*a*(1E-9)*VF*VF)/(MVs))*(0.5-X)).*((t-
        (s(i)./2))^2).*(1E-18);
        % Osmotic potential at t=<s<2t (/kT)
    else
        Vosm(i)=0;
        % Osmotic potential at s>=2t (/kT)
    end
end

% Elastic
  for i=1:length(s);
    if s(i)<t;
        Vela(i)=((2*pi*Na*a*(1E-9)*VF*t*t*(1E-
        18)*d*(1E6))/(MW)).*(((s(i)./t).*log((s(i)./t).*(((3-
        (s(i)./t))./2).^2)))-(6.*log((3-(s(i)./t))./2))+(3.*(1-
        (s(i)./t))));
        % Elastic potential at s<t (/kT)
    else
        Vela(i)=0;
        % Elastic potential at s>=t (/kT)
    end
```

```
    end

    % Total interaction potential (/kT)
            Vt=Vvdw+Vele+Vosm+Vela;


% Plotting the output
      p=plot (s,Vvdw,'b--',s,Vele,'k--',s,Vosm,'g--',s,Vela,'m--
      ',s,Vt,'r',s,0,'k');
      set(p(5),'linewidth',1.5);
      xlim([0 10])
      ylim([-20 30])
      xlabel('Separation distance (nm)')
      ylabel('Interaction pair potential/kBT (unitless)')
      legend({'Van der
      Walls','Electrostatic','Osmotic','Elastic','Total'},'FontSize',8)
      ;

% Displaying the numerical output
      set(handles.Debye, 'String', K);
      set(handles.VF, 'String', VF);

function Reset_Callback(hObject, eventdata, handles)
cla(handles.axes1,'reset')
      set(findobj(0,'style','edit'),'string',0)
      set(handles.Debye,'String',0);
      set(handles.VF,'String',0);
      set(handles.DefaultData,'String','')
```

```
set(handles.DefaultData2,'String','');

function Default_Callback(hObject, eventdata, handles)
% Setting the default parameter values for Au@MHA nanoparticles
      set(handles.Radius,'String',6.5);
      set(handles.Hamaker,'String',4e-19);
      set(handles.Zeta,'String',-20.9);
      set(handles.IS,'String',63);
      set(handles.Temp,'String',298.15);
      set(handles.Perm,'String',78.4);
      set(handles.SMW,'String',18.01528);
      set(handles.SD,'String',1);
      set(handles.FH,'String',0.45);
      set(handles.LMW,'String',148.22);
      set(handles.LD,'String',1.087);
      set(handles.LL,'String',1.2);
      set(handles.SAMD,'String',4.58e14);
      set(handles.Tilt,'String',39);
      set(handles.DefaultData,'String','These values correspond to
      mercaptoundecanoic acid (MHA) functionalized gold nanoparticles
      suspended in water');
      set(handles.DefaultData2,'String','Please reset the values before
      any further calculations');
% Nanoparticle parameters
      a=6.5;              % Nanoparticle radius (nm)
      A=4e-19;            % J
      ZP=-20.9;           % mV
      I=63;               % mM (same as mol/m3)
```

```
% System parameters

      T=298.15;            % K

      Er=78.4;             % unitless

      MWs=18.01528;        % Molecular weight of solvent (g/mol)

      ds=1000000;          % Density of solvent molecules (g/m3)

      X=0.45;              % Flory Huggins solvency parameter


% Ligand parameters

      MW=148.22;           % Molecular weight of ligand (g/mol)

      d=1.087;             % Density of pure ligand (g/cm3)

      l=1.2;               % Molecule length (nm)

      Pd=4.58e14;          % SAM packing density (molecules/cm2)

      Theta=39;            % Tilt angle (degrees)


% Constants

      E0=8.854E-12;        % F/m

      kB=1.381E-23;        % J/K

      e=1.602E-19;         % C

      Na=6.022E23;         % /mol


% Calculation of parameters

      s=[0.001:0.01:10];

      % Separation distances in nm

      K=(((2*Na*e*e*I)/(E0*Er*kB*T))^0.5)*(1E-9);

      % Inverse Debye length in nm-1

      t=l*cos(Theta*(pi/180));

      % SAM thickness (nm)
```

```
     Psi0=(ZP*0.001)*(1+(1/(K*a)))*exp(1);
     % Surface potential in V
     Y=(8*tanh((e*Psi0)/(4*kB*T)))/(1+((1-
     (((2*K*a)+1)/(((K*a)+1)^2)*((tanh((e*Psi0)/(4*kB*T)))^2)))^0.5));
     % Factor required to calculate Vele
     C=(1000*10000*Pd*MW)/Na;
     % Surface concentration of SAM (mg/m2)
     VF=(3*C*a*a)/(d*(((t+a)^3)-(a^3)));
     % Volume fraction of SAM (unitless)
     MVs=MWs/ds;
     % Molar volume of solvent (m3/mol)

% Calculation of potentials
   % Van der Waals
           Vvdw=-
           (A/(6*kB*T))*(((2*a*a)./(((4*a)+s).*s))+((2*a*a)./(((2*a)+s
           ).^2))+log((((4*a)+s).*s)./(((2*a)+s).^2)));
           % Van der Waals potential (/kT)
   % Electrostaic
       if (K*a)<5
           Vele=((4*pi*E0*Er*a*a*(1E-18)*Y*Y*kB*T)/(e*e)).*((exp(-
           K.*s))./((s+(2*a))*(1E-9)));
           % Electrostatic potential at Ka<5 (/kT)
       else
           Vele=((2*pi*E0*Er)/(kB*T))*(Psi0^2)*(a*(1E-9))*log(1+exp(-
           K.*s));
           % Electrostatic potential at Ka>5 (/kT)
       end
```

```
% Osmotic

for i=1:length(s);

    if s(i)<t;

        Vosm(i)=(((4*pi*Na*a*(1E-9)*VF*VF*t*t*(1E-18))/(MVs))*(0.5-

        X)).*((s(i)./(2*t))-(1/4)-log(s(i)./t));

        % Osmotic potential at s<t (/kT)

 elseif s(i)<(2*t);

        Vosm(i)=(((4*pi*Na*a*(1E-9)*VF*VF)/(MVs))*(0.5-X)).*((t-

        (s(i)./2))^2).*(1E-18);

        % Osmotic potential at t=<s<2t (/kT)

    else

        Vosm(i)=0;

        % Osmotic potential at s>=2t (/kT)

    end

end

% Elastic

for i=1:length(s);

    if s(i)<t;

        Vela(i)=((2*pi*Na*a*(1E-9)*VF*t*t*(1E-

        18)*d*(1E6))/(MW)).*(((s(i)./t).*log((s(i)./t).*(((3-

        (s(i)./t))./2).^2)))-(6.*log((3-(s(i)./t))./2))+(3.*(1-

        (s(i)./t))));

        % Elastic potential at s<t (/kT)

    else

        Vela(i)=0;

        % Elastic potential at s>=t (/kT)

    end

end
```

```
% Total interaction potential (/kT)
      Vt=Vvdw+Vele+Vosm+Vela;

% Plotting the output
      p=plot (s,Vvdw,'b--',s,Vele,'k--',s,Vosm,'g--',s,Vela,'m--
      ',s,Vt,'r',s,0,'k');
      set(p(5),'linewidth',1.5);
      xlim([0 10])
      ylim([-20 30])
      xlabel('Separation distance (nm)')
      ylabel('Interaction pair potential/kBT (unitless)')
      legend({'Van der
      Walls','Electrostatic','Osmotic','Elastic','Total'},'FontSize',8)
      ;

% Displaying the numerical output
      set(handles.Debye, 'String', K);
      set(handles.VF, 'String', VF);
```

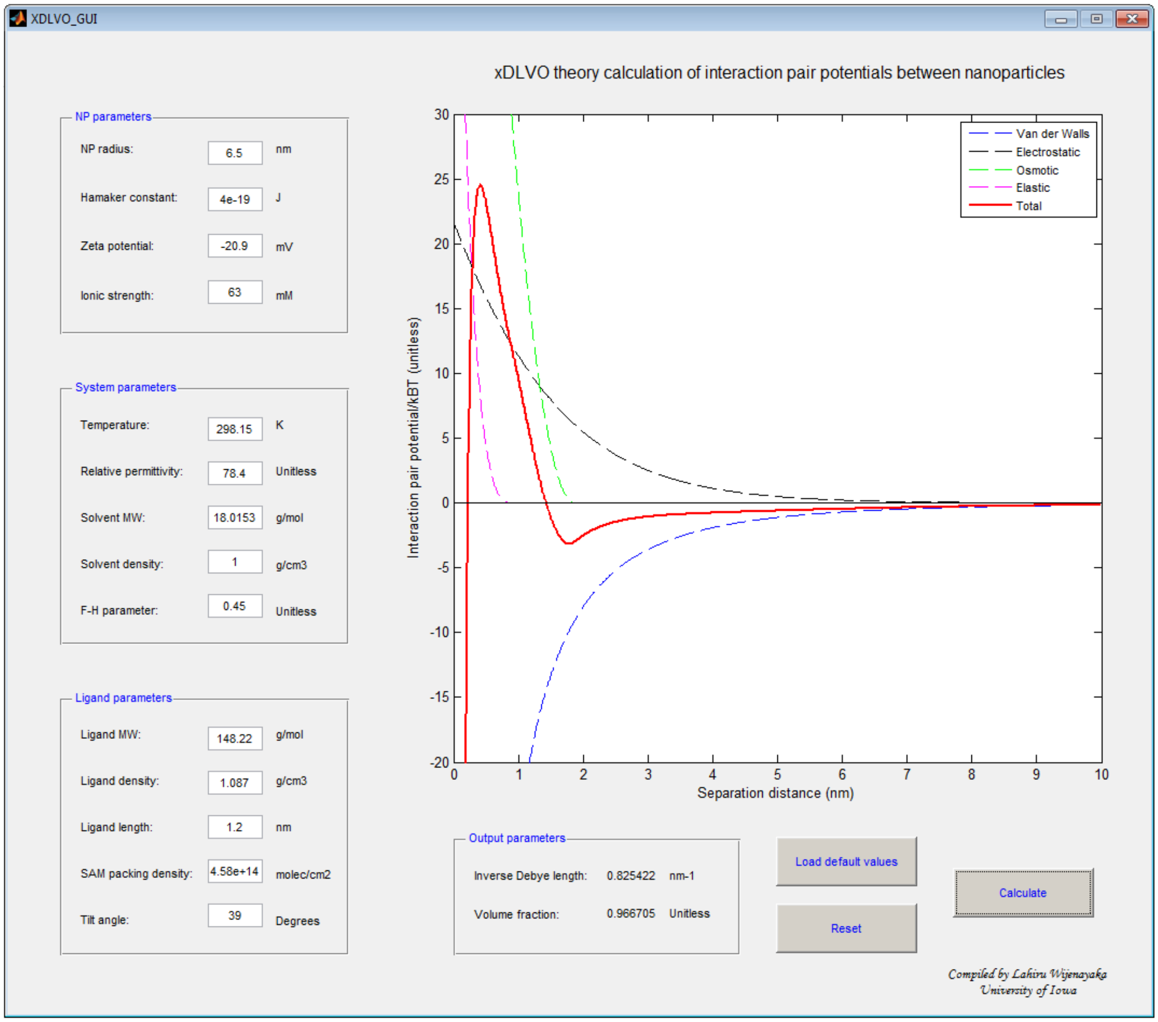

NP parameters

NP radius: 6.5 nm

Hamaker constant: 4e-19 J

Zeta potential: -20.9 mV

Ionic strength: 63 mM

System parameters

Temperature: 298.15 K

Relative permittivity: 78.4 Unitless

Solvent MW: 18.0153 g/mol

Solvent density: 1 g/cm3

F-H parameter: 0.45 Unitless

Ligand parameters

Ligand MW: 148.22 g/mol

Ligand density: 1.087 g/cm3

Ligand length: 1.2 nm

SAM packing density: 4.58e+14 molec/cm2

Tilt angle: 39 Degrees

Output parameters

Inverse Debye length: 0.825422 nm-1

Volume fraction: 0.966705 Unitless

*Compiled by Lahiru Wijenayaka*
*University of Iowa*

Figure E.1 MATLAB based graphical user interface developed for the calculation and display of individual and total interaction potentials between a pair of spherical nanoparticles suspended in solution at a known temperature.

# REFERENCES

(1) Ivanov, M. R.; Haes, A. J. *Anal. Chem.* **2011**, *84*, 1320.

(2) Hamm, P.; Zanni, M. *Concepts and Methods of 2D Infrared Spectroscopy*; Cambridge University Press: Cambridge, UK, 2011.

(3) Rock, W.; Li, Y.-L.; Pagano, P.; Cheatum, C. M. *The Journal of Physical Chemistry A* **2013**, *117*, 6073.

(4) Justin, L. A.; Jeremy, D. D.; Ralph, A. T.; Yiping, Z. In *Functional Nanoparticles for Bioanalysis, Nanomedicine, and Bioelectronic Devices Volume 2*; American Chemical Society: 2012; Vol. 1113, p 235.

(5) Titus, E. J.; Weber, M. L.; Stranahan, S. M.; Willets, K. A. *Nano Letters* **2012**, *12*, 5103.

(6) Stranahan, S. M.; Titus, E. J.; Willets, K. A. *The Journal of Physical Chemistry Letters* **2011**, *2*, 2711.

(7) Osawa, M. In *Handbook of Vibrational Spectroscopy*; John Wiley & Sons, Ltd: 2006.

(8) Donaldson, P. M.; Hamm, P. *Angewandte Chemie International Edition* **2013**, *52*, 634.

(9) Heni, W.; Vonna, L.; Haidara, H. *Nano Letters* **2015**, *15*, 442.

(10) Kim, J.-K.; Howard, M. D.; Dziubla, T. D.; Rinehart, J. J.; Jay, M.; Lu, X. *ACS Nano* **2011**, *5*, 209.

(11) Manikas, A. C.; Causa, F.; Della Moglie, R.; Netti, P. A. *ACS Applied Materials & Interfaces* **2013**, *5*, 7915.

(12) Ding, X.; Kong, L.; Wang, J.; Fang, F.; Li, D.; Liu, J. *ACS Appl. Mater. Interfaces* **2013**, *5*, 7072.

(13) Mieszawska, A. J.; Mulder, W. J. M.; Fayad, Z. A.; Cormode, D. P. *Mol. Pharmaceut.* **2013**, *10*, 831.

(14) Fazal, S.; Jayasree, A.; Sasidharan, S.; Koyakutty, M.; Nair, S. V.; Menon, D. *ACS Appl. Mater. Interfaces* **2014**, *6*, 8080.

(15) Baeissa, A.; Dave, N.; Smith, B. D.; Liu, J. *ACS Appl. Mater. Interfaces* **2010**, *2*, 3594.

(16) Maurer, J. H. M.; González-García, L.; Reiser, B.; Kanelidis, I.; Kraus, T. *ACS Appl. Mater. Interfaces* **2015**, *7*, 7838.

(17) Weeraman, C.; Yatawara, A. K.; Bordenyuk, A. N.; Benderskii, A. V. *J. Am. Chem. Soc.* **2006**, *128*, 14244.

(18) Ling, X. Y.; Reinhoudt, D. N.; Huskens, J. *Langmuir* **2006**, *22*, 8777.

(19) Beaurepaire, E.; Buissette, V.; Sauviat, M.-P.; Giaume, D.; Lahlil, K.; Mercuri, A.; Casanova, D.; Huignard, A.; Martin, J.-L.; Gacoin, T.; Boilot, J.-P.; Alexandrou, A. *Nano Lett.* **2004**, *4*, 2079.

(20) Chakraborty, S.; Padhy, S. *Acs Nano* **2008**, *2*, 2029.

(21) Chandni, U.; Kundu, P.; Singh, A. K.; Ravishankar, N.; Ghosh, A. *ACS Nano* **2011**, *5*, 8398.

(22) Chen, S. W. *Anal. Chim. Acta* **2003**, *496*, 29.

(23) Liu, J.; Legros, S.; Ma, G.; Veinot, J. G. C.; von der Kammer, F.; Hofmann, T. *Chemosphere* **2012**, *87*, 918.

(24) Saunders, S. R.; Eden, M. R.; Roberts, C. B. *J. Phys. Chem. C* **2011**, *115*, 4603.

(25) Skoglund, S.; Lowe, T. A.; Hedberg, J.; Blomberg, E.; Wallinder, I. O.; Wold, S.; Lundin, M. *Langmuir* **2013**, *29*, 8882.

(26) Hotze, E. M.; Phenrat, T.; Lowry, G. V. *J. Environ. Qual.* **2010**, *39*, 1909.

(27) Donaldson, P. M.; Hamm, P. *Angewandte Chemie* **2013**, *52*, 634.

(28) Haes, A. J.; Haynes, C. L.; McFarland, A. D.; Schatz, G. C.; Van Duyne, R. P.; Zou, S. *MRS Bulletin* **2005**, *30*, 368.

(29) Halas, N. *MRS Bulletin* **2005**, *30*, 362.

(30) Osawa, M. In *Near-Field Optics and Surface Plasmon Polaritons*; Kawata, S., Ed.; Springer Berlin Heidelberg: 2001; Vol. 81, p 163.

(31) Brown, L. V.; Zhao, K.; King, N.; Sobhani, H.; Nordlander, P.; Halas, N. J. *Journal of the American Chemical Society* **2013**, *135*, 3688.

(32) Lu, F.; Jin, M.; Belkin, M. A. *Nat Photon* **2014**, *8*, 307.

(33) Giannini, V.; Francescato, Y.; Amrania, H.; Phillips, C. C.; Maier, S. A. *Nano Lett.* **2011**, *11*, 2835.

(34) Johnson, S. A.; Pham, N. H.; Novick, V. J.; Maroni, V. A. *Appl. Spectrosc.* **1997**, *51*, 1423.

(35) Seelenbinder, J. A.; Brown, C. W.; Pivarnik, P.; Rand, A. G. *Anal. Chem.* **1999**, *71*, 1963.

(36) Brown, C. W.; Li, Y.; Seelenbinder, J. A.; Pivarnik, P.; Rand, A. G.; Letcher, S. V.; Gregory, O. J.; Platek, M. J. *Anal. Chem.* **1998**, *70*, 2991.

(37) Bjerke, A. E.; Griffiths, P. R.; Theiss, W. *Analytical Chemistry* **1999**, *71*, 1967.

(38) Lu, G.-Q.; Sun, S.-G.; Cai, L.-R.; Chen, S.-P.; Tian, Z.-W.; Shiu, K.-K. *Langmuir* **2000**, *16*, 778.

(39) Osawa, M.; Ataka, K.-i.; Yoshii, K.; Yotsuyanagi, T. *J. Electron. Spectrosc. Relat. Phenom.* **1993**, *64–65*, 371.

(40) Lal, S.; Grady, N. K.; Kundu, J.; Levin, C. S.; Lassiter, J. B.; Halas, N. J. *Chemical Society Reviews* **2008**, *37*, 898.

(41) Nikoobakht, B.; El-Sayed, M. A. *Chemistry of Materials* **2003**, *15*, 1957.

(42) Gole, A.; Murphy, C. J. *Chemistry of Materials* **2004**, *16*, 3633.

(43) Tse Sum Bui, B.; Merlier, F.; Haupt, K. *Analytical Chemistry* **2010**, *82*, 4420.

(44) Liu, P.; Liu, R.; Guan, G.; Jiang, C.; Wang, S.; Zhang, Z. *Analyst* **2011**, *136*, 4152.

(45) Intra, J.; Salem, A. K. *Journal of Controlled Release* **2008**, *130*, 129.

(46) Ivanov, M. R.; Bednar, H. R.; Haes, A. J. *ACS Nano* **2009**, *3*, 386.

(47) Culzoni, M. J.; Goicoechea, H. C.; Pagani, A. P.; Cabezon, M. A.; Olivieri, A. C. *Analyst* **2006**, *131*, 718.

(48) Olivieri, A. C. *Journal of Chemometrics* **2005**, *19*, 253.

(49) Mat Lazim, A.; Bradley, M.; Eastoe, J. *Langmuir* **2010**, *26*, 11779.

(50) German, S. R.; Luo, L.; White, H. S.; Mega, T. L. *J. Phys. Chem. C* **2012**, *117*, 703.

(51) Li, J.-L.; Liu, X.-Y.; Wang, X.-G.; Wang, R.-Y. *Langmuir* **2011**, *27*, 7820.

(52) Hwang, S. J.; Kim, S.-K.; Lee, J.-G.; Lee, S.-C.; Jang, J. H.; Kim, P.; Lim, T.-H.; Sung, Y.-E.; Yoo, S. J. *J. Am. Chem. Soc.* **2012**, *134*, 19508.

(53) Li, J.; Armstrong, B. L.; Kiggans, J.; Daniel, C.; Wood, D. L. *Langmuir* **2012**, *28*, 3783.

(54) Zhang, Z.; Chen, Z.; Wang, S.; Qu, C.; Chen, L. *ACS Appl. Mater. Interfaces* **2014**, *6*, 6300.

(55) Segets, D.; Marczak, R.; Schäfer, S.; Paula, C.; Gnichwitz, J.-F.; Hirsch, A.; Peukert, W. *ACS Nano* **2011**, *5*, 4658.

(56) Gambinossi, F.; Mylon, S. E.; Ferri, J. K. *Adv. Colloid Interface Sci.* **2015**, in press.

(57) Biggs, S.; Mulvaney, P.; Zukoski, C. F.; Grieser, F. *J. Am. Chem. Soc.* **1994**, *116*, 9150.

(58) Wu, C.; Xu, Q.-H. *Langmuir* **2009**, *25*, 9441.

(59) Cho, E. C.; Zhang, Q.; Xia, Y. *Nat. Nano.* **2011**, *6*, 385.

(60) Asakura, S.; Oosawa, F. *J. Polym. Sci.* **1958**, *33*, 183.

(61) Zhang, X.; Servos, M. R.; Liu, J. *J. Am. Chem. Soc.* **2012**, *134*, 9910.

(62) Phenrat, T.; Saleh, N.; Sirk, K.; Kim, H.-J.; Tilton, R.; Lowry, G. *J. Nanopart. Res.* **2008**, *10*, 795.

(63) Sonntag, H.; Strenge, K. *Coagulation Knetics and Structure Formation*; Plenum Press: New York, 1987.

(64) Kilpatrick, J. I.; Loh, S.-H.; Jarvis, S. P. *J. Am. Chem. Soc.* **2013**, *135*, 2628.

(65) Cornelis, G. *Environ. Sci.: Nano* **2015**.

(66) Gunawan, C.; Lim, M.; Marquis, C. P.; Amal, R. *J. Mater. Chem. B* **2014**, *2*, 2060.

(67) Salado, J.; Insausti, M.; Lezama, L.; Gil de Muro, I.; Goikolea, E.; Rojo, T. *Chem. Mater.* **2011**, *23*, 2879.

(68) Sánchez-Iglesias, A.; Grzelczak, M.; Altantzis, T.; Goris, B.; Pérez-Juste, J.; Bals, S.; Van Tendeloo, G.; Donaldson, S. H.; Chmelka, B. F.; Israelachvili, J. N.; Liz-Marzán, L. M. *ACS Nano* **2012**, *6*, 11059.

(69) Puddu, V.; Perry, C. C. *ACS Nano* **2012**, *6*, 6356.

(70) Pinchuk, A. O. *J. Phys. Chem. C* **2012**, *116*, 20099.

(71) Faure, B.; Salazar-Alvarez, G.; Bergström, L. *Langmuir* **2011**, *27*, 8659.

(72) Subbaraman, R.; Zawodzinski, T.; Mann, J. A. *Langmuir* **2008**, *24*, 8245.

(73) Overbeek, J. T. G. *J. Colloid Interface Sci.* **1977**, *58*, 408.

(74) Tohver, V.; Chan, A.; Sakurada, O.; Lewis, J. A. *Langmuir* **2001**, *17*, 8414.

(75) Bhardwaj, R.; Fang, X.; Somasundaran, P.; Attinger, D. *Langmuir* **2010**, *26*, 7833.

(76) Herman, D.; Walz, J. Y. *Langmuir* **2013**, *29*, 5982.

(77) Wu, L.; Gao, B.; Tian, Y.; Muñoz-Carpena, R.; Zigler, K. J. *Langmuir* **2013**, *29*, 3976.

(78) Park, H.-Y.; Schadt, M. J.; Wang; Lim, I. I. S.; Njoki, P. N.; Kim, S. H.; Jang, M.-Y.; Luo, J.; Zhong, C.-J. *Langmuir* **2007**, *23*, 9050.

(79) McMahon, J. M.; Emory, S. R. *Langmuir* **2006**, *23*, 1414.

(80) Jiang, H.; Moon, K.-s.; Li, Y.; Wong, C. P. *Chem. Mater.* **2006**, *18*, 2969.

(81) Han, Y.; Jiang, J.; Lee, S. S.; Ying, J. Y. *Langmuir* **2008**, *24*, 5842.

(82) Jiang, Y.; Yin, P.; Li, Y.; Sun, Z.; Liu, Q.; Yao, T.; Cheng, H.; Hu, F.; Xie, Z.; He, B.; Pan, G.; Wei, S. *J. Phys. Chem. C* **2012**, *116*, 24999.

(83) Marmisollé, W. A.; Capdevila, D. A.; de la Llave, E.; Williams, F. J.; Murgida, D. H. *Langmuir* **2013**, *29*, 5351.

(84) Techane, S. D.; Gamble, L. J.; Castner, D. G. *J. Phys. Chem. C* **2011**, *115*, 9432.

(85) Love, J. C.; Estroff, L. A.; Kriebel, J. K.; Nuzzo, R. G.; Whitesides, G. M. *Chem. Rev.* **2005**, *105*, 1103.

(86) Yamamoto, H.; Waldeck, D. H. *J. Phys. Chem. B* **2002**, *106*, 7469.

(87) Frederiksen, T.; Munuera, C.; Ocal, C.; Brandbyge, M.; Paulsson, M.; Sanchez-Portal, D.; Arnau, A. *ACS Nano* **2009**, *3*, 2073.

(88) Enustun, B. V.; Turkevich, J. *J. Am. Chem. Soc.* **1963**, *85*, 3317.

(89) Johnsson, M.; Wagenaar, A.; Engberts, J. B. F. N. *J. Am. Chem. Soc.* **2002**, *125*, 757.

(90) Li, K.; Zhao, X.; K. Hammer, B.; Du, S.; Chen, Y. *ACS Nano* **2013**, *7*, 9664.

(91) Sperling, R. A.; Parak, W. J. *Surface Modification, Functionalization and Bioconjugation of Colloidal Inorganic Nanoparticles*, 2010; Vol. 368.

(92) He, L.; Hu, Y.; Wang, M.; Yin, Y. *ACS Nano* **2012**, *6*, 4196.

(93) Wang, D.; Tejerina, B.; Lagzi, I.; Kowalczyk, B.; Grzybowski, B. A. *ACS Nano* **2010**, *5*, 530.

(94) Hu, Y.; Uzun, O.; Dubois, C.; Stellacci, F. *J. Phys. Chem. C* **2008**, *112*, 6279.

(95) Huang, R.; Carney, R. P.; Stellacci, F.; Lau, B. L. T. *Langmuir* **2013**, *29*, 11560.

(96) Moskovits, M.; Vlckova, B. *J. Phys. Chem. B* **2005**, *109*, 14755.

(97) Berg, J. C. *An Introduction to Interfaces & Colloids - The Bridge to Nanoscience*; World Scientific Publishing Co. Pte. Ltd.: Singapore, 2010.

(98) Rudolph, M.; Peuker, U. A. *J. Nanopart. Res.* **2012**, *14*.

(99) Babchin, A. J.; Schramm, L. L. *Colloids Surf., B* **2012**, *91*, 137.

(100) Lee, K. T.; Sathyagal, A. N.; McCormick, A. V. *Colloid Surf., A* **1998**, *144*, 115.

(101) Ohshima, H. *J. Colloid Interface Sci.* **1995**, *174*, 45.

(102) Lin, S. H.; Wiesner, M. R. *Langmuir* **2012**, *28*, 11032.

(103) Liu, Y.; Yan, E. C. Y.; Zhao, X.; Eisenthal, K. B. *Langmuir* **2001**, *17*, 2063.

(104) Sprycha, R.; Matijevic, E. *Langmuir* **1989**, *5*, 479.

(105) Mefford, O. T.; Vadala, M. L.; Goff, J. D.; Carroll, M. R. J.; Mejia-Ariza, R.; Caba, B. L.; St. Pierre, T. G.; Woodward, R. C.; Davis, R. M.; Riffle, J. S. *Langmuir* **2008**, *24*, 5060.

(106) Dederichs, T.; Möller, M.; Weichold, O. *Langmuir* **2009**, *25*, 10501.

(107) Mani, E.; Sanz, E.; Bolhuis, P. G.; Kegel, W. K. *J. Phys. Chem. C* **2010**, *114*, 7780.

(108) Israelachvili, J. N.; ScienceDirect *Intermolecular and surface forces [electronic resource] / Jacob N. Israelachvili*; Academic Press: Burlington, MA :, 2011; Vol. 3rd ed.

(109) Parsegian, V. A.; Weiss, G. H. *J. Colloid Interface Sci.* **1981**, *81*, 285.

(110) Ederth, T. *Langmuir* **2001**, *17*, 3329.

(111) Binks, B. P.; Clint, J. H.; Fletcher, P. D. I.; Lees, T. J. G.; Taylor, P. *Langmuir* **2006**, *22*, 4100.

(112) He, Y.; Zeng, T. *J. Phys. Chem. C* **2010**, *114*, 18023.

(113) Kim, T.; Lee, K.; Gong, M.-s.; Joo, S.-W. *Langmuir* **2005**, *21*, 9524.

(114) Lundgren, A. O.; Björefors, F.; Olofsson, L. G. M.; Elwing, H. *Nano Lett.* **2008**, *8*, 3989.

(115) Vincent, B.; Edwards, J.; Emmett, S.; Jones, A. *Colloids Surf.* **1986**, *18*, 261.

(116) Haes, A. J.; Zou, S.; Schatz, G. C.; Van Duyne, R. P. *J. Phys. Chem. B* **2004**, *108*, 6961.

(117) Ehler, T. T.; Malmberg, N.; Noe, L. J. *J. Phys. Chem. B* **1997**, *101*, 1268.

(118) Jensen, T.; Kelly, L.; Lazarides, A.; Schatz, G. C. *J. Cluster Sci.* **1999**, *10*, 295.

(119) Haes, A. J.; Van Duyne, R. P. *J. Am. Chem. Soc.* **2002**, *124*, 10596.

(120) Jung, L. S.; Campbell, C. T.; Chinowsky, T. M.; Mar, M. N.; Yee, S. S. *Langmuir* **1998**, *14*, 5636.

(121) Chen, H. J.; Kou, X. S.; Yang, Z.; Ni, W. H.; Wang, J. F. *Langmuir* **2008**, *24*, 5233.

(122) Okamoto, T.; Yamaguchi, I.; Kobayashi, T. *Opt. Lett.* **2000**, *25*, 372.

(123) Sannomiya, T.; Sahoo, P. K.; Mahcicek, D. I.; Solak, H. H.; Hafner, C.; Grieshaber, D.; Voeroes, J. *Small* **2009**, *5*, 1889.

(124) Tanaka, A.; Nakamura, B. *Optical Imaging: Technology, Methods and Applications*; Nova Science Publishers, 2012.

(125) Volkert, A. A.; Pierre, M. C. S.; Shrestha, B.; Haes, A. J. *RSC Adv.* **2015**, *5*, 3774.

(126) Qian, H.; Eckenhoff, W. T.; Zhu, Y.; Pintauer, T.; Jin, R. *J. Am. Chem. Soc.* **2010**, *132*, 8280.

(127) Bae, G.-T.; Aikens, C. M. *J. Phys. Chem. A* **2013**, *117*, 10438.

(128) Maniu, D.; Chis, V.; Baia, M.; Toderas, F.; Astilean, S. *J. Optoelectr. Adv. Materials* **2007**, *9*, 733.

(129) Rooth, M.; Shaw, A. M. *J. Phys. Chem. C* **2007**, *111*, 15363.

(130) Volkert, A. A.; Subramaniam, V.; Ivanov, M. R.; Goodman, A. M.; Haes, A. J. *ACS Nano* **2011**, *5*, 4570.

(131) Abad, J. M.; Mertens, S. F. L.; Pita, M.; Fernández, V. M.; Schiffrin, D. J. *J. Am. Chem. Soc.* **2005**, *127*, 5689.

(132) Yan, C.; Gölzhäuser, A.; Grunze, M.; Wöll, C. *Langmuir* **1999**, *15*, 2414.

(133) Hou, Z.; Abbott, N. L.; Stroeve, P. *Langmuir* **1998**, *14*, 3287.

(134) Qi, Y.; Ratera, I.; Park, J. Y.; Ashby, P. D.; Quek, S. Y.; Neaton, J. B.; Salmeron, M. *Langmuir* **2008**, *24*, 2219.

(135) Baker, C. O.; Shedd, B.; Tseng, R. J.; Martinez-Morales, A. A.; Ozkan, C. S.; Ozkan, M.; Yang, Y.; Kaner, R. B. *ACS Nano* **2011**, *5*, 3469.

(136) Yamada, K.; Miyajima, K.; Mafuné, F. *J. Phys. Chem. C* **2007**, *111*, 11246.

(137) Mafuné, F.; Kohno, J.-y.; Takeda, Y.; Kondow, T. *J. Phys. Chem. B* **2003**, *107*, 12589.

(138) Schatz, G. C.; Van Duyne, R. P. *Electromagnetic Mechanism of Surface-Enhanced Spectroscopy*; Wiley: New York, 2002; Vol. 1.

(139) Wustholz, K. L.; Henry, A. I.; McMahon, J. M.; Freeman, R. G.; Valley, N.; Piotti, M. E.; Natan, M. J.; Schatz, G. C.; Van Duyne, R. P. *Journal of the American Chemical Society* **2010**, *132*, 10903.

(140) Camden, J. P.; Dieringer, J. A.; Zhao, J.; Van Duyne, R. P. *Accounts of Chemical Research* **2008**, *41*, 1653.

(141) Halas, N. J.; Lal, S.; Chang, W.-S.; Link, S.; Nordlander, P. *Chemical Reviews (Washington, DC, United States)* **2011**, *111*, 3913.

(142) Schatz, G. C.; Young, M. A.; Van Duyne, R. P. *Topics in Applied Physics* **2006**, *103*, 19.

(143) Pierre, M. C. S.; Mackie, P. M.; Roca, M.; Haes, A. J. *Journal of Physical Chemistry C* **2011**, *115*, 18511.

(144) Fraire, J. C.; Pérez, L. A.; Coronado, E. A. *The Journal of Physical Chemistry C* **2013**, *117*, 23090.

(145) Cecchini, M. P.; Turek, V. A.; Paget, J.; Kornyshev, A. A.; Edel, J. B. *Nature Materials* **2013**, *12*, 165.

(146) Edel, J. B.; Kornyshev, A. A.; Urbakh, M. *ACS Nano* **2013**, *7*, 9526.

(147) Pierre, M. C. S.; Haes, A. J. *Analytical Chemistry* **2012**, *84*, 7906.

(148) Pierre, M. C. S.; Mackie, P. M.; Roca, M.; Haes, A. J. *The Journal of Physical Chemistry C* **2011**, *115*, 18511.

(149) Volkert, A. A.; Subramaniam, V.; Haes, A. J. *Chemical Communications* **2011**, *47*, 478.

(150) Brown, K. R.; Walter, D. G.; Natan, M. J. *Chemistry of Materials* **2000**, *12*, 306.

(151) Haiss, W.; Thanh, N. T. K.; Aveyard, J.; Fernig, D. G. *Analytical Chemistry* **2007**, *79*, 4215.

(152) Brewer, S. H.; Allen, A. M.; Lappi, S. E.; Chasse, T. L.; Briggman, K. A.; Gorman, C. B.; Franzen, S. *Langmuir* **2004**, *20*, 5512.

(153) Nagaraju, D. H.; Lakshminarayanan, V. *Langmuir* **2008**, *24*, 13855.

(154) Dutta, S.; Li, Y.-L.; Rock, W.; Houtman, J. C. D.; Kohen, A.; Cheatum, C. M. *The Journal of Physical Chemistry B* **2012**, *116*, 542.

(155) Palomaki, P. K. B.; Dinolfo, P. H. *ACS Applied Materials & Interfaces* **2011**, *3*, 4703.

(156) Kim, K.; Shin, D.; Choi, J.-Y.; Kim, K. L.; Shin, K. S. *The Journal of Physical Chemistry C* **2011**, *115*, 24960.

(157) Kwok, S. W.; Fotsing, J. R.; Fraser, R. J.; Rodionov, V. O.; Fokin, V. V. *Organic Letters* **2010**, *12*, 4217.

(158) Butini, S.; Gemma, S.; Brindisi, M.; Borrelli, G.; Lossani, A.; Ponte, A. M.; Torti, A.; Maga, G.; Marinelli, L.; La Pietra, V.; Fiorini, I.; Lamponi, S.; Campiani, G.; Zisterer, D. M.; Nathwani, S.-M.; Sartini, S.; La Motta, C.; Da Settimo, F.; Novellino, E.; Focher, F. *Journal of Medicinal Chemistry* **2011**, *54*, 1401.

(159) Alloisio, M.; Demartini, A.; Cuniberti, C.; Petrillo, G.; Thea, S.; Giorgetti, E.; Giusti, A.; Dellepiane, G. *The Journal of Physical Chemistry C* **2007**, *111*, 345.

(160) Lohmüller, T.; Triffo, S.; O'Donoghue, G. P.; Xu, Q.; Coyle, M. P.; Groves, J. T. *Nano Letters* **2011**, *11*, 4912.

(161) Gai, X. S.; Coutifaris, B. A.; Brewer, S. H.; Fenlon, E. E. *Physical Chemistry Chemical Physics* **2011**, *13*, 5926.

(162) Dyall, L.; Kemp, J. *Australian Journal of Chemistry* **1967**, *20*, 1395.

(163) Wijenayaka, L. A.; Ivanov, M. R.; Cheatum, C. M.; Haes, A. J. *The Journal of Physical Chemistry C* **2015**, *119*, 10064.

(164) Zook, J. M.; Rastogi, V.; MacCuspie, R. I.; Keene, A. M.; Fagan, J. *ACS Nano* **2011**, *5*, 8070.

(165) Wan, L.-J.; Terashima, M.; Noda, H.; Osawa, M. *The Journal of Physical Chemistry B* **2000**, *104*, 3563.

(166) Chulhai, D. V.; Jensen, L. *The Journal of Physical Chemistry C* **2013**, *117*, 19622.

(167) Wang, Y.; Yan, B.; Chen, L. *Chemical Reviews* **2013**, *113*, 1391.

(168) Ren, B.; Lin, X.-F.; Yang, Z.-L.; Liu, G.-K.; Aroca, R. F.; Mao, B.-W.; Tian, Z.-Q. *Journal of the American Chemical Society* **2003**, *125*, 9598.

(169) Ohta, K.; Maekawa, H.; Saito, S.; Tominaga, K. *The Journal of Physical Chemistry A* **2003**, *107*, 5643.

(170) Schultz, P. W.; Leroi, G. E.; Popov, A. I. *Journal of the American Chemical Society* **1996**, *118*, 10617.

(171) Lu, G.-Q.; Sun, S.-G.; Chen, S.-P.; Cai, L.-R. *Journal of Electroanalytical Chemistry* **1997**, *421*, 19.

(172) Luk'yanchuk, B.; Zheludev, N. I.; Maier, S. A.; Halas, N. J.; Nordlander, P.; Giessen, H.; Chong, C. T. *Nat Mater* **2010**, *9*, 707.

(173) Neubrech, F.; Pucci, A.; Cornelius, T. W.; Karim, S.; García-Etxarri, A.; Aizpurua, J. *Phys. Rev. Lett.* **2008**, *101*, 157403.

(174) *Near-field microscopy by elastic light scattering from a tip*, 2004; Vol. 362.

(175) Le, F.; Brandl, D. W.; Urzhumov, Y. A.; Wang, H.; Kundu, J.; Halas, N. J.; Aizpurua, J.; Nordlander, P. *ACS Nano* **2008**, *2*, 707.

(176) Habib, A.; Tabata, M.; Wu, Y. G. *Bulletin of the Chemical Society of Japan* **2005**, *78*, 262.

(177) Hoffmann, J. M.; Yin, X.; Richter, J.; Hartung, A.; Maß, T. W. W.; Taubner, T. *The Journal of Physical Chemistry C* **2013**, *117*, 11311.

(178) Xie, J.; Lee, J. Y.; Wang, D. I. C. *Chemistry of Materials* **2007**, *19*, 2823.

(179) Liu, H.; Xu, Y.; Qin, Y.; Sanderson, W.; Crowley, D.; Turner, C. H.; Bao, Y. *The Journal of Physical Chemistry C* **2013**, *117*, 17143.

(180) Huck, C.; Neubrech, F.; Vogt, J.; Toma, A.; Gerbert, D.; Katzmann, J.; Härtling, T.; Pucci, A. *ACS Nano* **2014**, *8*, 4908.

(181) Link, S.; Mohamed, M. B.; El-Sayed, M. A. *The Journal of Physical Chemistry B* **1999**, *103*, 3073.

(182) Hao, F.; Nehl, C. L.; Hafner, J. H.; Nordlander, P. *Nano Letters* **2007**, *7*, 729.

(183) Wokaun, A.; Gordon, J. P.; Liao, P. F. *Physical Review Letters* **1982**, *48*, 957.

(184) Kooij, E. S.; Ahmed, W.; Hellenthal, C.; Zandvliet, H. J. W.; Poelsema, B. *Colloids and Surfaces A: Physicochemical and Engineering Aspects* **2012**, *413*, 231.

(185) Webb, J. A.; Erwin, W. R.; Zarick, H. F.; Aufrecht, J.; Manning, H. W.; Lang, M. J.; Pint, C. L.; Bardhan, R. *The Journal of Physical Chemistry C* **2014**, *118*, 3696.

(186) Liu, X.-L.; Wang, J.-H.; Liang, S.; Yang, D.-J.; Nan, F.; Ding, S.-J.; Zhou, L.; Hao, Z.-H.; Wang, Q.-Q. *J. Phys. Chem. C* **2014**, *118*, 9659.

(187) Kumar, P. S.; Pastoriza-Santos, I.; Rodríguez-González, B.; Abajo, F. J. G. d.; Liz-Marzán, L. M. *Nanotechnology* **2008**, *19*, 015606.

(188) Khoury, C. G.; Vo-Dinh, T. *J. Phys. Chem. C* **2008**, *112*, 18849.

(189) Yuan, H.; Khoury, C. G.; Wilson, C. M.; Grant, G. A.; Bennett, A. J.; Vo-Dinh, T. *Nanomedicine: Nanotechnology, Biology and Medicine* **2012**, *8*, 1355.

(190) Rodríguez-Oliveros, R.; Sánchez-Gil, J. A. *Opt. Express* **2012**, *20*, 621.

(191) Hrelescu, C.; Sau, T. K.; Rogach, A. L.; Jäckel, F.; Feldmann, J. *Applied Physics Letters* **2009**, *94*, 153113.

(192) Day, J. P.; Barany, F.; Hammer, R. P.; Bergstrom, D. *Nucleic Acids Res.* **1999**, *27*, 1819.

(193) Lee, T. K.; Kwak, S. K. *The Journal of Physical Chemistry C* **2014**, *118*, 5881.

(194) Hao, F.; Sonnefraud, Y.; Dorpe, P. V.; Maier, S. A.; Halas, N. J.; Nordlander, P. *Nano Letters* **2008**, *8*, 3983.

(195) Forney, M. W.; Poler, J. C. *J. Phys. Chem. C* **2011**, *115*, 10531.

(196) Kubo, S.; Diaz, A.; Tang, Y.; Mayer, T. S.; Khoo, I. C.; Mallouk, T. E. *Nano Lett.* **2007**, *7*, 3418.

(197) Kreibig, U.; Vollmer, M. *Optical properties of metal clusters*; Springer-Verlag Berlin Heidelberg 2010; Vol. 25.